JUSTUS-LIEBIG-
UNIVERSITÄT
GIESSEN

Physikalisch-Chemisches Institut
Physikalische Festkörperchemie

The $LiNiO_2$ Cathode Active Material: Characterization and Optimization of the Calcination Process

Dem Fachbereich Biologie und Chemie
der Justus-Liebig-Universität Giessen

vorgelegte Dissertation
zur Erlangung des akademischen Grades

Doktor der Naturwissenschaften
- Dr.rer.nat. -

von

Philipp Kurzhals

Dekan/Dean:	Prof. Dr. Thomas Wilke
1.Gutachter / 1st Reviewer:	Prof. Dr. Jürgen Janek
2.Gutachter / 2nd Reviewer:	Prof. Dr. Peter Klar

Bearbeitungszeit: 01.03.2019 – 31.07.2022

Contents

Declaration of authorship

This thesis was prepared from the 1st of March 2019 until the 31st of July 2022 at the Institute of Physical Chemistry of the Justus Liebig University Gießen under the supervision of Prof. Dr. Jürgen Janek and the experimental work was performed at the Battery Materials Research group of BASF SE in Ludwigshafen.
I hereby declare that I wrote this thesis independently and did not use any sources and tools other than the ones stated in the references, that I marked the literally and textually adopted passages in an appropriate way and respected the constitution for the protection of good scientific practice of the Justus Liebig University Gießen. I agree to a potential check of this thesis with a plagiarism assessment software.

Gießen, the _____

Philipp Kurzhals

Danksagung

Zunächst möchte ich mich bei Prof. Dr. Janek bedanken, der diese Arbeit betreut hat und mir die Möglichkeit gab, die Promotion in seiner Arbeitsgruppe durchzuführen. Obwohl ich als externer Doktorand nicht den tagtäglichen Kontakt zur Arbeitsgruppe hatte, war ich trotzdem gut eingebunden und in regem Austausch, was in hohem Maße Prof. Janek zu verdanken ist. Ich konnte mich beim Anfertigen der wissenschaftlichen Publikationen immer auf seine Unterstützung verlassen und habe ihn in den letzten Jahren sehr zu schätzen gelernt.

Für die Übernahme des Zweitgutachtens dieser Arbeit danke ich Prof. Dr. Peter Klar. Weiterhin danke ich Prof. Dr. Kerstin Volz und PD Dr. Matthias Elm dafür, dass sie sich bereiterklärt haben, Teil der Prüfungskommission zu sein.

Besonderer Dank gilt Heino Sommer, der mich bei BASF vor Ort betreut und die Ideen dieser Arbeit maßgeblich mitgestaltet hat. Er war es, der mich nach dem Masterstudium in Karlsruhe zunächst für ein Praktikum zu BASF geholt und mir anschließend die Möglichkeit gegeben hat, eine externe Promotion in der Battery Materials Research Gruppe durchzuführen. Seine fachliche Expertise und seine wissenschaftliche Neugier haben mich inspiriert und wesentlich zu dieser Arbeit beigetragen.

In gleichem Maße zu Dank verpflichtet bin ich Felix Riewald, der mit mir gemeinsam als externer Doktorand bei BASF gearbeitet hat. Die Experimente, die wir gemeinsam geplant, durchgeführt und ausgewertet haben, die vielen Diskussionen über die Arbeit und Themen außerhalb des Batteriefelds sowie die vielen Momente, in denen wir zusammen einfach herzlich gelacht haben, werde ich alle nie vergessen. Es war mir eine Freude, mit ihm die wissenschaftlichen Publikationen zu schreiben und ich habe ihn in dieser Zeit als einen wahren Vollblut-Wissenschaftler kennengelernt und einen sehr guten Freund gefunden.

Weiterhin möchte ich mich beim BASF battery team in Ludwigshafen bedanken und hier insbesondere bei den Laboranten, die mich immer unterstützt haben und für ein freundschaftliches und offenes Arbeitsumfeld gesorgt haben. In gleichem Kontext be-

danke ich mich bei Rafael Berk, Cheuck Ching, Svenja Seiffert und Sören Dreyer für die Zusammenarbeit bezüglich wissenschaftlicher Themen, aber auch für die schönen Momente außerhalb der Arbeit.

Außerdem möchte ich mich bei meiner Familie bedanken, meiner Mutter Berlind, meinem Vater Olaf, meinem Onkel Knut sowie meinen Großeltern Herta, Erna und Walter, die mich während der gesamten Schulzeit, dem Studium und der Promotion durchgehend unterstützt haben und ohne die ich diesen langen Weg nicht geschafft hätte. Besonders bedanke ich mich bei meiner Freundin Julia, die mich während der Promotionszeit unglaublich unterstützt hat und mich gerade in den schwierigen Phasen immer wieder motivieren konnte.

Abstract

The well-known cathode active material (CAM) $LiNiO_2$ (LNO) has recently regained the attention of scientists from both industry and academia as it potentially offers an increased energy density compared to the materials used in today's Lithium-Ion Batteries. Despite long-standing research efforts, LNO still faces severe challenges regarding its inherent instability during battery operation (mechanical fracturing of LNO particles, build-up of resistive surface layers, release of gaseous species) and its synthesis, which is difficult to control and to transfer to large-scale production.
From literature search, certain requirements can be deduced for the synthesis of LNO with desired properties for its use as CAM, but the investigated synthesis parameter space is often chosen too broadly, the described processes cannot be transferred to large-scale production or the provided data is incomplete. Thus, the first goal of this thesis was to carry out a comprehensive calcination study to find correlations between synthesis conditions and the resulting physicochemical properties of LNO.
In the first publication, a detailed discussion of the sample preparation and the structural chemistry was provided. Overall, 18 LNO samples were calcined and the structural properties were investigated by powder X-ray diffraction, magnetization measurements and half-cell voltage profiles. These experiments yielded consistent results regarding the amount of excess Ni^{2+} ions in the Li layer („off-stoichiometry“) and the impact of the calcination conditions on said Ni excess could be revealed. However, it was found that the Ni excess showed no correlation to the irreversible capacity loss occurring in the first charge-discharge cycle, which is contrary to previous literature results.
These findings motivated the in-depth study on the secondary and primary particle morphology together with the morphological changes during electrochemical cycling, which was presented in the second publication. The secondary particle structure of LNO fractures during cycling and thus the primary particle size distribution is of utmost importance as it will eventually determine the interface area between CAM and electrolyte. An automated scanning electron microscopy image segmentation was implemented to quantify the primary particle size distribution of the pristine CAM powder. Moreover, an impedance-based „capacitance“ method was used to monitor *in situ* the changes of the specific surface area between CAM and electrolyte during elec-

trochemical cycling. It was shown that this quantity approached a value commensurate to the estimate of primary particle specific surface area from SEM image analysis after just a few cycles. Electrochemical tests revealed that this surface area determines not only the 1^{st} cycle capacity loss but also the capacity retention and the resistance build-up during long-term cycling. Overall, within this thesis it was demonstrated that particle morphology is a key parameter that needs to be considered in future CAM development.

Following the calcination study, the focus was set on the optimization of the calcination throughput in order to comply with the steadily increasing CAM demand from battery cell manufacturers. Therefore, the third publication dealt with a two-stage calcination process to separate the lithiation reaction in a „partial-lithiation“ step from the crystallization and particle growth during the calcination step. This partial-lithiation was tested under fixed-bed and agitated-bed conditions using different furnaces. The agitated-bed case was found to yield a faster lithiation and was thus further optimized regarding the temperature profile. Afterwards, the partially-lithiated samples were subjected to a calcination step and characterized using the analysis concepts developed in the preceding publications. Benchmark testing against an LNO sample prepared by a standard one-stage calcination revealed that comparable physicochemical properties and electrochemical performance can be obtained using the partial-lithiation concept. However, with this novel approach the CAM production throughput could potentially be increased by a factor of ~ 3 compared to the one-stage counterpart. Thus, this synthesis concept is highly recommended to be tested not only on a laboratory scale but also towards an application in large-scale production.

Zusammenfassung

Das altbekannte Kathodenaktivmaterial $LiNiO_2$ (LNO) hat kürzlich das Interesse von Wissenschaftlern aus Industrie und akademischer Welt erneut geweckt, da es potenziell eine höhere Energiedichte im Vergleich zu den Materialien in aktuellen Lithiumionenbatterien anbietet. Trotz der langjährigen Forschungsanstrengungen ist LNO weiterhin mit ernstzunehmenden Herausforderungen konfrontiert hinsichtlich der innewohnenden Instabilitätsprobleme während des Batteriebetriebs (mechanisches Brechen der LNO Partikel, Aufbau von widerstandsbehafteten Oberflächenschichten, Freisetzung von gasförmigen Spezies) und der Synthese, die schwierig zu kontrollieren und zur großskaligen Produktion zu transferieren ist.
Aus der Literatur können einige Voraussetzungen für die Synthese von LNO mit gewünschten Eigenschaften für die Verwendung als Kathodenaktivmaterial abgeleitet werden, aber der untersuchte Syntheseparameterraum ist oft zu breit gewählt, der beschriebene Prozess kann nicht zu großskaliger Produktion transferiert werden oder die zur Verfügung gestellten Daten sind unvollständig. Deshalb war es das erste Ziel dieser Arbeit, eine umfassende Kalzinationsstudie durchzuführen, um Korrelationen zwischen den Synthesebedingungen und den resultierenden physikalisch-chemischen Eigenschaften von LNO zu finden.
In der ersten Publikation wurde eine detaillierte Diskussion der Probenherstellung und der Strukturchemie zur Verfügung gestellt. Insgesamt wurden 18 LNO Proben kalziniert und die strukturellen Eigenschaften wurden mittels Pulver-Röntgendiffraktion, Magnetisierungsmessungen und Halbzellspannungsprofilen untersucht. Diese Experimente haben übereinstimmende Resultate bezüglich der Menge an überschüssigen Ni^{2+} Ionen in der Li Schicht ergeben und der Einfluss der Kalzinationsbedingungen auf diesen Ni Überschuss konnte offengelegt werden. Es wurde allerdings herausgefunden, dass der Ni Überschuss keine Korrelation zum irreversiblen Kapazitätsverlust im ersten Lade-Entlade-Zyklus zeigt, was im Widerspruch zu bisherigen Literaturergebnissen steht.
Diese Resultate haben eine ausführliche Studie der Sekundär- und Primärpartikelmorphologien sowie der morphologischen Änderungen während des elektrochemischen Zyklisierens motiviert, die in der zweiten Publikation vorgelegt wurde. Die Sekundärpartikelstruktur von LNO bricht während des Zyklisierens, weshalb die Primärpar-

tikelgrößenverteilung zunehmend an Bedeutung gewinnt, da sie schließlich die Oberfläche zwischen Kathodenaktivmaterial und Elektrolyt bestimmen wird. Eine automatisierte Segmentierung für Aufnahmen eines Rasterelektronenmikroskops wurde implementiert, um die Größenverteilung der Primärpartikel des ursprünglichen Kathodenaktivmaterialpulvers zu quantifizieren. Weiterhin wurde eine impedanzbasierte „capacitance“ Methode verwendet, um *in situ* die Änderungen der spezifischen Oberfläche zwischen Kathodenaktivmaterial und Elektrolyt während des elektrochemischen Zyklisierens zu beobachten. Es wurde gezeigt, dass sich diese Größe nach nur wenigen Zyklen einem Wert annähert, der proportional zur Abschätzung der spezifischen Primärpartikeloberfläche aus der Analyse der Rasterelektronenmikroskopieaufnahmen ist. Elektrochemische Tests haben deutlich gemacht, dass diese Oberfläche nicht nur den Kapazitätsverlust im ersten Zyklus, sondern auch den Kapazitätserhalt und den Widerstandsaufbau während des Langzeitzyklisierens bestimmt. Insgesamt wurde in dieser Arbeit nachgewiesen, dass die Partikelmorphologie ein Schlüsselparameter ist, der für die zukünftige Entwicklung von Kathodenaktivmaterialien berücksichtigt werden muss.
Nach der Kalzinationsstudie wurde der Fokus auf die Optimierung des Kalzinationsdurchsatzes gelegt, um der kontinuierlich ansteigenden Nachfrage an Kathodenaktivmaterial durch die Batteriezellhersteller nachzukommen. Hierzu hat sich die dritte Publikation mit einem zweistufigen Kalzinationsprozess beschäftigt, um die Lithiierungsreaktion in einem „Teil-Lithiierungs“ -Schritt von der Kristallisation und dem Partikelwachstum während des Kalzinationsschritts zu trennen. Die Teil-Lithiierung wurde unter starren und aufgewirbelten Bedingungen unter Einsatz unterschiedlicher Öfen getestet und es wurde herausgefunden, dass letztere zu einer schnelleren Lithiierung führt, weshalb sie weiter bezüglich des Temperaturprofils optimiert wurde. Im Anschluss an die Teil-Lithiierung wurden die Proben einem Kalzinationsschritt unterzogen und charakterisiert, wobei die Analysekonzepte verwendet wurden, die in den vorangegangenen Publikationen entwickelt worden waren. Der Vergleichstest mit einer LNO Probe, die mit einer standardmäßigen einstufigen Kalzination hergestellt wurde, hat offenbart, dass vergleichbare physikalisch-chemische Eigenschaften und elektrochemische Leistungsfähigkeit mit dem Teil-Lithiierungs-Konzept erzielt werden können. Allerdings könnte dieser neuartige Ansatz den Produktionsdurchsatz für Kathodenaktivmaterial potenziell um einen Faktor 3 im Vergleich zu seinem einstufigen Gegenstück erhöhen. Deshalb wird es mit Nachdruck empfohlen, dieses alternative Synthesekonzept nicht nur im Labormaßstab sondern auch bezüglich einer Anwendung in großskaliger Produktion zu testen.

List of Abbreviations

CAM	Cathode Active Material
LNO	$LiNiO_2$
LIB	Lithium-Ion Battery
SEM	Scanning Electron Microscopy
NCM	$Li(Ni_{1-x-y}Co_xMn_y)O_2$
NCA	$Li(Ni_{1-x-y}Co_xAl_y)O_2$
BEV	Battery Electric Vehicle
LCO	$LiCoO_2$
XRD	X-ray Diffraction
EC	Ethylene Carbonate
DEC	Diethyl Carbonate
DMC	Dimethyl Carbonate
PVDF	Polyvinylidene fluoride
RHK	Roller Hearth Kiln
ASSB	All-Solid-State Battery

Chapter 1

Introduction

The focus of this PhD thesis is on the cathode active material (CAM) $LiNiO_2$ (LNO). Since the first documentation of its synthesis in 1954[1] and the first reported use as CAM in an electrochemical cell in 1985,[2] a tremendous number of researchers has spent time and effort on the optimization of this material. So one could definitively ask the question: what is yet to come from this apparently „old material“?
For a long period of time, LNO has been described as *model material* for the layered transition metal oxides $Li(Ni_{1-x-y}Co_xMn_y)O_2$ (NCM) and $Li(Ni_{1-x-y}Co_xAl_y)O_2$ (NCA) with a high Ni content, which are currently used to power battery electric vehicles (BEVs), indicating that it is rather interesting for academia but not considered to be a promising commercial product. This is linked to its intrinsic structural, mechanical and thermal instability issues. However, as the demand for energy storage solutions has been increasing over the recent years, CAM manufacturers start to change opinions: it is considered to be more efficient to follow a top-down approach starting from LNO, which promises increased energy density at reduced overall costs of the battery compared to systems applying the currently available NCM and NCA compositions. The pure LNO is then diluted with foreign atoms („dopants“) to stabilize the bulk layered structure and the vulnerable surface of the CAM particles is protected by a coating layer. Following this strategy, customer targets could be reached faster compared to the alternative bottom-up approach, where the Ni content in NCM and NCA materials is only gradually increased in smaller steps. Thus, significant research and development effort in CAM industry is focused on the synthesis of LNO and on possible strategies to mitigate the instability problems.
The novelty of this thesis compared to older work on LNO is that it was prepared within a collaboration between academia (Justus Liebig University Gießen) and industry (BASF SE) and that the entire experimental work was done in the laboratories of BASF. As a consequence, state-of-the-art synthesis and characterization techniques were used and the process parameters were chosen in such a way, that a commercialization would in principle be possible.

In the first part of this work, the synthesis of LNO and its basic physicochemical properties were revisited. Many research groups have dealt with this topic and a large number of publications is already available (a selection will be discussed in the respective section). Various studies on this topic were published in the 1990s and early 2000s and during review it soon became clear that an industrially feasible process was out of the scope of these publications. The authors often used a very broad range of calcination conditions, which makes it difficult to say if the optimal material was produced or if the optimum hid somewhere in between the prepared samples. Furthermore, the appropriate choice of starting materials (nickel-containing precursor and Li source) is important for a potential scale-up to mass production, but is seldom considered by academia. Moreover, the electrochemical testing conditions were far away from what is assumed to be today's standard to assess the goodness of the material for its use as CAM. Finally, the provided data were often incomplete as the focus of the authors was only on a specific set of properties, e.g., defects in the crystal structure or magnetic behavior, without the aim to get a full picture.
Therefore, in this thesis special attention was paid on the careful choice of educts and calcination conditions and a large number of characterization techniques was applied to reveal formerly unknown correlations between the CAM preparation and the resulting physicochemical properties. The results opened up a new perspective on the question which property determines the electrochemical performance of LNO. While in the past the crystal structure (more precisely: the exact Li stoichiometry) was often considered to be the most important factor that influences LNO's performance as CAM, this systematic study showed that primary particle morphology plays a key role. By the use of newly developed methods (automated SEM image segmentation, *in situ* measurement of CAM-to-electrolyte interface area during battery operation), it was possible to quantify primary particle size distributions and to follow the development of the specific surface area in contact with the electrolyte during electrochemical cycling. The results revealed that this specific surface area determines 1st cycle capacity loss, capacity retention and resistance growth.
The reported findings will also have an impact on the stabilization strategies for LNO (bulk doping and surface coating) and for Ni-rich NCM and NCA materials, as the established concepts are expected to be transferable to these systems, too.
The second part of this work took a deep dive into the question how the calcination procedure can be further optimized to end up with an economically feasible process. After in the first part the correlations between synthesis parameters and physicochemical properties were discussed, the investigation of a possible process concept to increase the production throughput and concomitantly reduce production costs was the goal of the subsequent study. This reflects the overall intention of this thesis to study a well-known material while putting special emphasis on practicable synthesis conditions. On the way, important aspects of the LNO calcination process were revisited and complemented. The novel methods developed in the first part of this thesis were applied in

this work as well to assess the quality of the produced materials. Taking into account all findings, a new direction for resource-efficient CAM manufacturing was suggested. All in all, this comprehensive work contributes to the in-depth understanding of LNO, which is not only a *model material* for academia anymore but also a *target material* for industry.

Chapter 2

Background: The Journey of $LiNiO_2$

2.1 Motivation

In this paragraph, the history of LNO will be recapitulated to recall the established concepts in the literature and to point out the open questions, which were addressed in the course of this work. However, as this thesis is intended to examine LNO from both academic and industrial perspective, at first it should be pointed out why this compound is currently in the focus of CAM manufacturers.
In fact, $LiCoO_2$ (LCO) was the first layered transition metal oxide to be used as CAM by the group of Goodenough in 1980,[3] meaning that it features alternating layers of Co^{3+} and Li^+ in an oxygen framework and that Li ions can be extracted from this layered structure. However, it was only five years later when the same group published a report on an LNO cathode used in an electrochemical cell.[2] The two compounds share many properties as they are „crystallographic twins“ and both crystallize in a rhombohedral unit cell, isostructural with α-$NaFeO_2$ with the space group $R\text{-}3m$. Moreover, they have a nearly identical theoretical capacity Q_{theo} of $\sim$ 274 $\text{mAh}\,\text{g}^{-1}$, which is due to their similar molecular weight (97.63 $\text{g}\,\text{mol}^{-1}$ for LNO and 97.87 $\text{g}\,\text{mol}^{-1}$ for LCO), that enters the expression in equation 2.1.

$$Q_{\text{theo}} = \frac{z \cdot F}{M_{\text{mol}}} \tag{2.1}$$

Here, z denotes the number of transferred electrons ($z = 1$ for both LNO and LCO) and $F \approx 96485\,\text{C}\,\text{mol}^{-1}$ is the Faraday constant.
However, it soon became clear that LCO is easier to prepare compared to LNO, especially on an industrial scale,[4,5] which is also reflected in the fact that the first commercialized Lithium-Ion Battery (LIB) featured an LCO cathode.[6] Subsequently, it was found that LCO exhibits rapid capacity fading when delithiated to a certain critical Li content,[7] and this in practice limits the achievable capacity to roughly 60% of the theoretical value ($\sim$ 164 $\text{mAh}\,\text{g}^{-1}$).[8,9] Although LCO cathodes still maintain a significant

market share for LIBs used in consumer electronics, due to the insufficient practical energy density they are not used to power BEVs.
Thus, the solid solutions NCM and NCA became popular, which combine the strengths of LNO (high energy density) and LCO (easy manufacturing and relative structural stability) with the additional improvements regarding structural and thermal stability provided by the electrochemically inactive Al^{3+} and Mn^{4+}, respectively. The energy density of these CAMs can be increased by increasing the Ni content, while considering the trade-off between higher capacity and reduced capacity retention.[10–12]
The limited global Co production capacity ($\sim$ 140 000 t Co compared to 2.4 Mio t Ni in 2021), the comparably higher raw material costs (US$ 70 000/t Co compared to US$ 24 000/t Ni at the end of 2021) and on-going concerns regarding the circumstances of Co mining ask for a further reduction of the Co content in the CAM.[13–15] While the first generations of BEVs utilized LIBs with moderate Ni and significant Co content („NCM 523“ with 50% Ni, 20% Co and 30% Mn and „NCM 622“ with 60% Ni, 20% Co and 20% Mn), current models employ cathodes with $\sim$ 80% Ni and $10 - 15$% Co.[16]
It is important to consider that Ni raw material costs are also not immune to severe fluctuations. In March 2022, the Ni price hit a record high at US$ 100 000/t due to price speculation of only one market player.[17] With cell manufacturers announcing ambitious plans to increase their production capacity in the near future, the increasing demand will intensify the fight for reliable raw material supply chains. CAM producers realized that this poses severe challenges for their businesses and securing long-term supply contracts, especially for Ni, became part of their priority lists to encounter price volatility. Despite the recent resurgence of $LiFePO_4$ as alternative cathode material for safe and low-cost LIBs for BEVs with a moderate driving range, NCM and NCA solid solutions are expected to remain predominant in the premium segment, probably reaching a Ni content ≥ 95% and a Co content ≤ 5% by 2025.[18] This continuous trend towards lower Co contents in LIBs brought up the question to academia „Is cobalt needed in Ni-rich positive electrode materials for lithium ion batteries?“ and the entire replacement of Co by other elements (e.g., Al and/or Mn) is under discussion.[19–22] This turns the spotlight again on LNO, as a fundamental understanding of its synthesis and properties should be gained prior to the investigation of its derivatives.

2.2 Synthesis and structural characterization

After clarifying why further research on LNO is needed, the following section will summarize the most important results on the synthesis and characterization given in the literature.
The first report on the preparation of LNO dates from 1954, when Dyer et al. successfully prepared the material by the chemical reaction between anhydrous LiOH and a

nickel tube at 800 °C in a pure oxygen atmosphere.[1] X-ray diffraction (XRD) analysis revealed that the oxygen ions form a cubic close packed structure with Li^+ and Ni^{3+} located in alternating layers in the octahedral interstices of the oxygen array.
In the following, it was found that LNO can be prepared by the reaction of NiO and Li_2O as depicted in equation 2.2.

$$\frac{1}{2}Li_2O + NiO + \frac{1}{4}O_2 \leftrightarrow LiNiO_2 \tag{2.2}$$

Note that an oxygen-containing atmosphere is needed to oxidize Ni^{2+} in NiO to Ni^{3+} in LNO. Goodenough et al. synthesized materials with lithium deficiency (some amount of the provided Li source was not incorporated in the LNO bulk structure) by the reaction of NiO and Li_2CO_3, whereby the latter starts to melt at $\sim 715\,°C$ concomitant with the decomposition to Li_2O and CO_2.[23,24] They showed that a material with less lithium deficiency could be prepared by the use of LiOH instead of Li_2CO_3 and pure O_2 instead of air. These findings were consistently reproduced in the literature and were an important starting point for this project, too.
The first use of LNO as CAM was reported by Thomas et al., who pressed LNO powder on a stainless steel grid, performed charging tests in an electrochemical cell and showed that Li^+ can be extracted to form $Li_{1-x}NiO_2$ (an Al anode and an electrolyte consisting of 1M solution of $LiBF_4$ in propylene carbonate were used).[2] Already at this early point in time it was noticed that it is impossible to prepare fully stoichiometric LNO, related to the difficulty to stabilize Ni^{3+} at the high preparation temperatures in the range of 700 °C and the similar ionic radii of Li ions ($r(Li^+) = 76\,pm$) and divalent Ni ions ($r(Ni^{2+}) = 69\,pm$).[25,26] This leads to the common representation $Li_{1-z}Ni_{1+z}O_2$, meaning that $2z$ Ni^{2+} ions are present in the material with half of them located in the „Ni slab“ and half of them in the „Li interslab“. This concept to describe LNO and related materials is called „off-stoichiometry“ or „cationic disorder“.
Moreover, LNO tends to thermal decomposition which emerges close to the required high calcination temperatures and leads to Li_2O formation according to the backward reaction in equation 2.2. Due to the volatility of Li_2O at these temperatures in an oxidizing atmosphere, this can lead to significant Li loss.[27] Thus, taking the off-stoichiometry and the thermal decomposition of LNO into account, its equilibrium state is better described by equation 2.3.

$$\frac{1}{1+z}Li_{1-z}Ni_{1+z}O_2 + \frac{z}{1+z}Li_2O + \frac{z}{2(1+z)}O_2 \leftrightarrow LiNiO_2 \tag{2.3}$$

Dahn et al. reported that the amount of excess Ni^{2+} in the Li layer has profound implications for the crystal structure, as the unit cell volume increases with increasing z.[28] In this study they also followed *in situ* the changes of the lattice parameters during electrochemical cycling by XRD using a Li metal anode. This was the starting point

for further measurements with an improved *in situ* setup by the same group, which yielded the phase diagram of LNO on electrochemical delithiation.[29] Three single-phase regions and three two-phase regions were identified, with phase transitions from an original hexagonal phase (H1) to a monoclinic phase (M) to a second hexagonal phase (H2) for increasing x in $Li_{1-x}NiO_2$. For the maximum degree of delithiation, a two-phase region consisting of the H2 phase and a third hexagonal phase (H3) was observed. Moreover, the illustration of the phase transitions using dQ/dV plots was applied, where the differential capacity dQ/dV is shown as a function of the cell voltage, resulting in minima for single-phase regions and sharp peaks corresponding to phase transitions. All three hereinafter discussed publications use this concept as a diagnostic tool to understand correlations between the materials' crystal structure and electrochemical behavior. Interestingly, 25 years after the original publication from 1993, a refreshed version was published, exploiting improved synthesis and characterization techniques.[30] The structural and electrochemical data from this work embody an important reference for the herein presented studies.

During the 1990s, the sensitivity of the LNO synthesis to the used reagents, the temperature profile and the atmosphere were further investigated. In 1993 Ohzuku et al. used a variety of Ni precursors (Ni metal, $Ni(OH)_2$, $Ni(NO_3)_2$, $NiCO_3$ and NiOOH), Li sources (LiOH, $LiNO_3$ and Li_2CO_3), calcination temperatures (750 °C, 800 °C, 850 °C and 900 °C) and distinguished between synthesis under air and under pure O_2.[31] However, the preparation conditions were changed in large steps and the electrochemical testing revealed that the samples were far away from being optimized.

One year later, Kanno et al. synthesized LNO samples starting from NiO and Li_2O_2, pure O_2 atmosphere, a dwell time at calcination temperature of 48 h and a broad range of temperatures (450 °C - 850 °C in 50 °C steps).[32] Selected samples were investigated by means of neutron diffraction and the authors reported that the sample calcined at 700 °C showed almost perfect stoichiometry with only 0.4% Ni excess in the Li layer. Although it should be questioned, whether such a low off-stoichiometry can indeed be realized (no detailed description of the experimental procedure and the reliability factors of the refinement were provided), throughout the literature 700 °C maximum calcination temperature has proven to be the „comfort zone“ of LNO.

Afterwards, Arai et al. suggested that LNO close to perfect stoichiometry could be prepared by the use of excess Li in the calcination (three molar equivalents of Li with respect to Ni were used as excess in this report) and a subsequent washing in H_2O combined with an annealing step to remove unreacted lithium-containing residuals.[33] They showed that with this approach a sample with only 0.5% Ni excess can be made. Moreover, they proposed a correlation between the amount of Ni^{2+} ions in the Li layer of the CAM and the achievable charge and discharge capacities in a half-cell with a Li metal anode. However, the authors draw this conclusion by comparing the material with small Ni excess to samples with a much larger off-stoichiometry (5.6 - 13.5% Ni excess) made by calcination at 800 °C and a dwell time of up to 60 h. Furthermore,

an industrially feasible process would aim at avoiding a washing step and certainly also the loss of 75% of precious Li source in the waste water, which requires expensive reprocessing.
Two years later, the same authors published a report, in which they prepared LNO with $\sim 1\%$ Ni^{2+} ions in the Li layer with the same excess Li method and discussed the discrepancy between the measured 1st charge capacity of $260\,mAh\,g^{-1}$ and the 1st discharge capacity of $220\,mAh\,g^{-1}$.[34] Although almost all Li can be deintercalated upon the 1st charge, as the theoretical capacity of LNO amounts to $274\,mAh\,g^{-1}$, not all of the Li can be reintercalated during discharge, which leads to an irreversible capacity loss in the very first cycle. The authors attributed this phenomenon to the formation of „inactive domains“, which they hypothesized to form only in the first cycle as the following cycles showed rather good Li reversibility. Moreover, they assumed that the formation of these inactive domains is likely affected by the properties of the pristine LNO powder such as surface morphology, particle size and interface area between LNO particles and the conductive carbon in the cathode framework.
Rougier et al. prepared a variety of LNO samples by the use of different Li sources (Li_2O, Li_2O_2 and Li_2CO_3), a broad range of maximum calcination temperatures (600°C, 700 °C, 800 °C, 850 °C and 950 °C) and also intentionally synthesized Li deficient samples.[35] They found out that for the preparation of „quasi 2D LNO“ with small z in $Li_{1-z}Ni_{1+z}O_2$ it is favorable to use a Li source with a high reactivity (oxide and peroxide preferred compared to the carbonate) and rather low calcination temperatures (600 °C and 700 °C). Using powder XRD and Rietveld refinement, the authors showed that the off-stoichiometry model yielded a good agreement with the experimental data, although a cation mixing between Li and Ni (Ni^{2+} in the Li layer and Li^+ in the Ni layer) was considered to be possible for very pronounced Li deficiency. However, it was also discussed that XRD analysis alone is not suitable to conclusively confirm either the off-stoichiometry or the cation mixing model due to the low scattering power of Li towards X-rays. Moreover, the authors characterized the materials by means of their magnetic susceptibility and confirmed that the magnetic behavior of LNO is related to the Ni excess and that the magnetic ordering temperature increases with z. Note that the mechanism behind the magnetic ordering is under debate up to today.[36] It can be said for sure that the ordering is caused by the interaction between the paramagnetic Ni^{3+} ions in the Ni slab and the extra Ni^{2+} ions in the Li layer. For a perfectly stoichiometric LNO, no long range ordering but pure paramagnetic behavior would be expected.
The authors used four samples of their study with $z = 0.02, 0.06, 0.12, 0.24$ to discuss the electrochemical behavior in a half-cell with a Li metal anode and the measurements revealed that reversible cycling was not possible when z was too large ($z = 0.24$ in this case). They assumed that the presence of excess Ni ions decreases the Li interslab thickness ($r(Ni^{2+}) < r(Li^+)$) and, in combination with a strong electrostatic repulsion between Ni^{2+} and Li^+, leads to hindered Li ion diffusion.

In a follow-up publication, the authors reinforced their observations and laid the focus on the 1st charge-discharge cycle.[37] They proposed that the oxidation of the excess Ni^{2+} in the Li layer to Ni^{3+} during charging leads to a shrinkage of the Li interslab space ($r(Ni^{3+}_{LS}) = 56\,pm < r(Ni^{2+}) = 69\,pm$; LS = low spin),[25] and thus the amount of Ni excess is responsible for the 1st cycle capacity loss. Furthermore, they charged the cells to voltages below 4 V vs. Li^+/Li, which means that overall less Li was extracted, and found very good reversibility. The authors assumed that in this case only Ni ions in the Ni slab were oxidized and the shrinkage of the Li layer was thus prevented. Finally, they observed that a deep discharge to 2 V vs. Li^+/Li and a long relaxation time of one month could be used to completely recover the initial Li content in the LNO cathode, although this was accompanied by a large increase in cell polarization. The local shrinkage of the Li interslab space might thus be reversed by the reduction of the excess Ni ions from the trivalent state back to the divalent one, but the required cycling conditions (low voltage, long relaxation time) suggest that this process is very slow.

Further important results on the structural chemistry of LNO were published by Pouillerie et al. who investigated samples with a broad range of off-stoichiometry values ($z = 0.02, 0.07$ and 0.25) by means of neutron diffraction.[38] As mentioned previously, besides the off-stoichiometry model with excess divalent Ni ions in the Li layer, a true „cation mixing“ between Li and Ni with a fraction of Li^+ in the Ni slab could be possible. Due to the large difference between the coherent scattering lengths of Li and Ni towards neutrons, the authors were able to probe both models and ascertained that there was no cation mixing for samples with moderate Li deficiency ($z = 0.02, 0.07$) and only a weak mixing with 2% Li^+ in the Ni layer for the sample with very pronounced Li deficiency ($z = 0.25$). These results embody an important basis for the present thesis as LNO samples with a small Li deficiency are sought for the use as industrially relevant CAM. With this neutron diffraction study in mind, powder XRD analysis performed in the course of this thesis was based on the off-stoichiometry model.

In the early 2000s, further efforts were made to understand correlations between the synthesis conditions and physicochemical properties of LNO. Bianchi et al. published a study on the calcination of LNO using the Li excess method, but with rather moderate excess ≤ 10 mol% in order to avoid a subsequent washing step.[39] The authors stated that they prepared a material with only 0.5% Ni excess in the Li layer by using a Li excess of 7 mol%, a maximum calcination temperature of 700 °C, $12 - 24$ h dwell time and a continuous oxygen flow (one furnace volume exchange every minute). By changing the amount of Li excess and the time of thermal treatment, samples with various amounts of Ni^{2+} ions in the Li layer were prepared and the change of the unit cell parameters and magnetic behavior for increasing Ni excess were investigated. For moderate values of $z = 0.01 - 0.05$, which is a range where commercially relevant materials are located, they found a linear increase of the unit cell volume with increasing amount of Ni^{2+} ions in the Li layer. Furthermore, they plotted the inverse magnetic

susceptibility as a function of temperature and fitted this curve to the Curie-Weiss law depicted in equation 2.4 for temperatures above 300 K

$$\chi = \frac{C}{T - \theta} \tag{2.4}$$

where χ is the magnetic susceptibility, C is the Curie constant, T is the temperature during the measurement and θ is the Weiss constant. From this relation, they extracted the Weiss constant θ, which describes the transition temperature between paramagnetic behavior at high temperatures towards a regime of magnetic ordering, and found a linear correlation between θ and the off-stoichiometry z, as had already been indicated in a preceding study.[35] The depiction of θ deduced from magnetization measurements and the unit cell volume gained from powder XRD analysis as a function of z were adopted for the later on presented synthesis study.

Bianchi et al. discussed the electrochemical data related to these samples in a subsequent publication and looked for possible correlations between the performance of LNO in a half-cell with Li metal anode and the amount of Ni^{2+} ions in the Li layer.[40] They displayed the voltage profiles (cell voltage vs. Li content in the cathode) for three LNO samples with $z = 0.008, 0.025$ and 0.062 and suggested that higher discharge capacities can be achieved for smaller off-stoichiometries. Moreover, it was argued that higher current rates led to an increased polarization for the sample with a rather moderate Ni excess of 2.5% in contrast to the material with $z = 0.008$, which was barely affected by a faster charge and discharge rate.

One key finding of this publication, which will be challenged in the course of this thesis, was a linear increase of the 1st cycle capacity loss for $Li_{1-z}Ni_{1+z}O_2$ samples with increasing values of z, taking into account the results from other research groups as well. However, the authors also pointed out that an extrapolation to $z = 0$ would not lead to an infinitesimal capacity loss, but to an irreversible loss of $\sim 27.5\ mAh\,g^{-1}$, which amounts to 10% of the theoretical capacity. Moreover, the cycling stability was suggested to be dependent on the amount of Ni excess as well as the sample with almost perfect stoichiometry ($z = 0.008$) showed the highest capacity retention.

Unfortunately, the conclusions from this work were drawn by the comparison of two self-made LNO samples ($z = 0.008$, 0.062) with a material provided from a commercial supplier ($z = 0.025$), meaning that the synthesis conditions for the latter are unknown. Moreover, the description of sample morphology was limited to one top view scanning electron microscopy (SEM) image per sample in a large magnification and the particle size was estimated to be within $0.2 - 2.0$ µm with a wide size distribution.[39] In general, information on the morphology of the LNO samples (particle size, size distribution, porosity, etc.) in all publications discussed so far was very scarce. The impact of the preparation conditions on the structural chemistry were widely discussed and correlations between the deviation from the ideal stoichiometry and the electrochemical performance were proposed, but the influence of other parameters could have been

overlooked. In this thesis, a lot of attention was paid on the morphology of LNO samples and for this reason the following section summarizes the main findings regarding this topic found in the literature.

2.3 Morphology

Broussely et al. prepared LNO samples by a solid state reaction using LiOH monohydrate and NiO (the properties of the reagents, e.g., particle shape and purity, were not further specified) at a maximum calcination temperature of 700 °C in air and performed long-term cycling tests in full-cells with a graphite anode.[5] They measured SEM images of the pristine cathode powder as well as recovered powder from the cell after 1200 cycles and showed that it was characterized by large agglomerates (diameter $\sim$ 10 µm) that consisted of smaller particles. However, the size of the smaller particles is vaguely identifiable due to the poor image resolution. The authors stated that no „electrochemical grinding“ occurred during cycling, which means that the particles were apparently intact after the charge-discharge test for 1200 cycles, but this cannot be judged from the SEM pictures in the publication.
Li et al. investigated the impact of particle morphology of LNO samples on the electrochemical performance and the thermal stability, which they measured as the weight loss due to partial thermal decomposition at high temperatures.[41] Without providing any details on the synthesis process, the authors compared three samples: one with an agglomerate size of $\sim$ 20 µm and a particle size below $\sim$ 1 µm, one with an agglomerate size of $\sim$ 8 µm and a particle size of $\sim$ 4 µm and one sample, where each agglomerate only consisted of one particle with a size of $\sim$ 12 µm (the provided SEM images cannot be evaluated due to their poor quality). They found out that samples with a larger particle size showed a better thermal stability, but slightly inferior capacities. One of the samples with a large particle size was specified with a 1st charge capacity of 195 mAh g^{-1} and a 1st discharge capacity of 150 mAh g^{-1}, meaning that 45 mAh g^{-1} capacity was lost in the very first cycle. The beforehand discussed publications in section 2.2 described the impact of the preparation conditions on the structural chemistry of the samples and dependencies between the off-stoichiometry and the electrochemical behavior were sought without considering the influence of particle morphology. In contrast, Li et al. set the focus on the particle morphology and its implications for the electrochemical performance without providing any information on the preparation conditions and the resulting off-stoichiometry, which makes it difficult to get the full picture.
Similar problems occur when analyzing another report on two commercial LNO samples, which were described as agglomerates of two different size distributions (5 µm - 10 µm and 10 µm - 20 µm, respectively) with each agglomerate consisting of fine parti-

cles with a size of $\sim 0.1\,\mu m$ (no SEM images shown in the publication).[42] The authors stated that the material with smaller agglomerates displayed slightly better electrochemical properties, but this could also stem from poorer crystallinity of the sample with larger agglomerates indicated by the depicted powder XRD patterns.

In 2000 a very important observation regarding morphological changes of LNO particles during cycling was made using a setup with separated LNO agglomerates ($20 - 50\,\mu m$ diameter) attached to a Pt microelectrode, which were cycled with Li metal foil as anode.[43] The LNO agglomerates were charged to increasing cut-off voltages and the changes of morphology were monitored with a combination of a microscope and a CCD camera. The authors revealed that the particles fractured into several smaller parts with a certain probability when charge voltages higher than 4.2 V vs. Li^+/Li were reached, indicated by the loss of electrical contact between agglomerate and microelectrode. They attributed this phenomenon to the significant reduction of the c lattice parameter of $Li_{1-x}NiO_2$, when it is delithiated to $x > 0.75$ and undergoes the structural phase transition from the H2 to the H3 phase, as observed by earlier *in situ* XRD investigations.[29,31] For agglomerated samples consisting of particles randomly attached to each other, they argued that the mechanical stress, induced by the large changes of the crystal structure during electrochemical operation, is likely to be concentrated at the grain boundaries. Up to the present day, the concept of particle fracturing due to volume contraction and expansion during charge-discharge cycling is considered to be one major failure mechanism of LNO and its derivatives NCM and NCA with a high Ni content.[10,44–47]

A first attempt to separately investigate the influence of structural chemistry and particle morphology on the electrochemical behavior of LNO was made by Chang et al., who used a sol-gel synthesis to prepare LNO samples with a similar off-stoichiometry but with different particle sizes.[48] They used 5 mol% Li excess and calcined the samples at a maximum calcination temperature of 750 °C in oxygen for 5 h, 15 h and 30 h, leading to samples with $\sim 1\%$ Ni excess and particle sizes ranging from 300 nm for 5 h dwell time to 800 nm for 30 h dwell time. The particle sizes were determined by inspecting the agglomerates with SEM and taking the average of ~ 200 particles per sample. The authors pointed out that the sample with the largest particle size has a $\sim 10\%$ lower discharge capacity compared to the one with the smallest particle size and attributed this result to increased diffusion paths for the Li^+ ions in case of larger particle sizes. Moreover, they prepared a sample with a maximum calcination temperature of 800 °C in air and a dwell time of 5 h, which was characterized by 7% Ni excess, the occurrence of Li_2CO_3 impurities in the powder XRD pattern and a similar particle size of ~ 800 nm compared to the LNO sample made at 750 °C and a dwell time of 30 h in oxygen. Despite the similar particle size, the sample prepared at 800 °C in air showed significantly worse electrochemical performance and this brought the authors

to the conclusion that impurity phases and the off-stoichiometry primarily impact the electrochemical properties of LNO and that the particle size is only of minor importance.
Similarly, one report dealt with the synthesis of LNO samples using a spherical $Ni(OH)_2$ precursor made by co-precipitation, a 4 mol% Li excess and three different maximum calcination temperatures (650 °C, 670 °C and 690 °C).[49] It was found that 670 °C calcination temperature led to the lowest amount of Ni^{2+} ions in the Li layer (the cation mixing model allowing Li^+ in the Ni layer was assumed, contrary to the neutron diffraction results discussed in section 2.2) and that this sample also revealed the highest 1st discharge capacity. The crystallite sizes were assessed using the powder XRD patterns and Rietveld refinement of the respective structural model and it was found that increasing the maximum calcination temperature in 20 °C steps resulted in a size increase from 200 nm to 380 nm and finally to 410 nm. Interestingly, the highest capacity retention was observed for the LNO sample prepared at the lowest investigated maximum calcination temperature of 650 °C.
It is important to note that the co-precipitation method used in the aforementioned study to prepare the $Ni(OH)_2$ precursor is the industrially applied process, as it allows for proper control of the agglomerate and crystallite sizes and the preparation of spherical agglomerates, which are beneficial for a homogeneous (de-)lithiation and electrode processing. Moreover, this process can be used to homogeneously distribute transition metals other than Ni in the precursor (e.g., Co, Mn and Al in the precursors made for the preparation of NCM and NCA cathode materials). In the studies published in the course of this thesis, $Ni(OH)_2$ precursors made by co-precipitation were applied for the synthesis of LNO. For the final CAM, the following terms were used: „secondary particles“ for the larger agglomerates ($4-12\,\mu m$ diameter) and „primary particles“ for the smaller particles (sizes of a few hundred nm), that the agglomerates consist of.

Additional work was published on the influence of calcination conditions on the properties of materials deviating from pure LNO, where Ni was replaced by one or more other metals. One study discussed the influence of maximum calcination temperature and amount of Li excess on physical and electrochemical properties of a CAM containing 90% Ni and 10% Co.[50] First, the authors fixed the Li excess at 3 mol% and varied the maximum calcination temperature between 710 °C and 750 °C in 10 °C steps using 15 h dwell time and an oxygen atmosphere. Afterwards, they took the beforehand optimized temperature and altered the Li:(Ni+Co) ratio (1.02, 1.03, 1.05 and 1.07). They found the best electrochemical performance for the material synthesized at 730 °C with 3 mol% Li excess, which also showed the lowest amount of Ni^{2+} ions in the Li layer ($\sim$ 0.3% Ni excess deduced from powder XRD analysis). This brought them to the conclusion that the cycling behavior is determined by the Ni excess, but did not look for a possible impact of particle morphology, although the average crystallite size from XRD analysis and qualitative information on the primary particle size from top view

SEM images were available.
Another publication examined the synthesis of an NCA CAM containing 15% Co and 5% Al, which consisted of secondary particle agglomerates with a diameter of $5 - 8\,\mu m$ and a primary particle size ranging from 200 nm to 300 nm to 500 nm with increasing maximum calcination temperature from 750 °C to 800 °C to 850 °C.[51] Here, the primary particle sizes were roughly estimated by the use of SEM imaging. From the analysis of powder XRD patterns, it was concluded that higher calcination temperatures led to an increasing Ni excess and this was used to explain the good electrochemical performance of the 750 °C sample, especially at higher current densities.
Moreover, the impact of calcination temperature was investigated for NCM samples, e.g., containing 20% Co and 30% Mn.[52] In this study, three different commercial precursors with varying shape and crystallite size were used for the synthesis. One of these precursors was used to optimize the maximum calcination temperature between 850 °C and 910 °C in 10 °C steps and it was found by examination of the powder XRD patterns that 880 °C yielded the sample with the smallest deviation from a perfectly layered crystal structure. Moreover, a linear increase of the primary particle size and a concomitant broadening of the size distribution with increasing calcination temperature were shown by SEM image analysis. For the size evaluation, the authors took the average over more than 200 primary particles per sample.
Afterwards, samples were prepared from all three precursors with a calcination temperature of 880 °C and it was found that the primary particle sizes differed significantly despite using exactly the same temperature profile, indicating a severe impact of the precursor morphology on primary particle growth. Electrochemical testing revealed that the initial capacity was higher for samples with a well-ordered crystal structure, whereas a sample with smaller primary particle size was shown to have a better capacity retention when compared to a material with larger primary particles.
Another study investigated the impact of the calcination temperature on the primary particle size, the amount of Ni excess and the electrochemical performance for NCM samples with 76% Ni, 14% Co and 10% Mn.[53] The authors used a transition metal hydroxide precursor made by co-precipitation, 3% Li excess and varied the maximum calcination temperature (725 °C, 750 °C, 775 °C, 800 °C, 850 °C, 900 °C) with a dwell time of 20 h in ambient air. Powder XRD analysis revealed that with increasing calcination temperature the crystallite size increased from 28 nm to 47 nm, but these values were calculated using only the 003 Bragg reflection and no information on the instrumental resolution function was provided. Rietveld refinement resulted in Ni excess values between 3.7% and 5.2%, with the lowest amount of Ni^{2+} ions in the Li layer observed for the material prepared at 775 °C. While top view SEM images showed „no clear difference in the size of primary particles“ for the samples calcined at 725 °C, 750 °C and 775 °C, a significant growth was observed at 800 °C and above with primary particle sizes of $\sim$ 1 µm for the sample prepared at 900 °C. The material calcined at 725 °C displayed both low 1st charge and 1st discharge capacity, which the authors

explained by means of a defective crystal structure, whereas the low 1st discharge capacity of the 900 °C sample was attributed to the larger Li^+ diffusion paths due to the larger primary particle sizes. In general, it was found that the capacity retention worsened with increasing maximum calcination temperature. The authors assumed that this observation was related to less crack formation for the CAMs with smaller primary particle sizes in cross section SEM images after 200 cycles, although only one secondary particle per sample was shown in the publication and no information was given on how the cathode powder was recovered or on the lithiation degree of the CAM at the end of the cycling test.

A calcination study comparing LNO and a CAM with a lower Ni content of 60% and equal amounts of Co and Mn was performed by Ronduda et al., who tried to correlate calcination temperature, structural properties and electrochemical performance.[54] For the LNO synthesis, they impregnated NiO with an aqueous solution of LiOH monohydrate and varied the maximum calcination temperature between 650 °C and 850 °C in 50 °C steps using a dwell time of 15 h and ambient air. They performed powder XRD measurements and found out that the 700 °C sample displayed the lowest amount of Ni excess, although no quantitative information was provided. The average crystallite size was shown to increase from 30 nm to 120 nm, when the maximum calcination temperature was increased and the same trend was observed for the primary particle size estimated by the examination of top view SEM images. The samples prepared by the lowest calcination temperatures (650 °C and 700 °C) showed the highest initial discharge capacities and significantly improved rate capability compared to their counterparts made at higher temperatures.
Interestingly, all NCM samples displayed smaller primary particles in the SEM images and average crystallite sizes from Rietveld refinement when compared to LNO CAMs prepared at the same maximum calcination temperature (NCM samples were synthesized with maximum calcination temperatures between 750 °C and 950 °C). The NCM sample synthesized at 900 °C showed the lowest amount of Ni excess and also the best electrochemical performance, indicating that for this CAM composition a „temperature tipping point“ exists, below and above which electrochemical properties are negatively affected. The authors mainly attributed the improved performance of the 700 °C LNO and the 900 °C NCM sample to the respective minimum values of Ni excess for a given chemical composition. The results again underlined that LNO should be calcined at rather moderate temperatures around 700 °C, whereas materials with a lower Ni content require significantly higher temperatures.
The study by Ronduda et al. yielded some important insights, but still the results should be taken with a grain of salt. The samples were prepared by impregnating the precursors with the Li source and a subsequent drying step was done at low temperature before the calcination, which is a process that most likely will not be used in industrial production. Moreover, the synthesis of LNO was performed in ambient air,

although it had been widely recognized in the literature that calcination in pure oxygen always yielded the better results. Lastly, the lack of quantitative evaluation of the primary particle size from the SEM images and the obvious discrepancy between particle size estimated from SEM and crystallite size determined from powder XRD analysis cast doubt on the published findings. This is a good example to illustrate why it was thought at the beginning of this thesis that a thorough investigation of correlations between synthesis parameters, structural chemistry, morphology and electrochemical performance of $LiNiO_2$ is still an open point that needs to be addressed.

2.4 Implications for the design of a calcination study

After reviewing the extensive literature on the synthesis of $LiNiO_2$ and the related NCM and NCA phases, several key problems became apparent. The most important issue was the incompleteness of the provided data. Many calcination studies only focussed on one synthesis parameter, e.g., the amount of Li excess, and searched for correlations with one specific physicochemical property, e.g., the amount of Ni^{2+} ions in the Li layer, without considering the other synthesis parameters (precursor, dwell time, atmosphere, maximum calcination temperature, handling of the moisture-sensitive CAM powder). Due to the sole focus on one key property, e.g., the structural chemistry, other important material properties (primary particle size, agglomeration, surface texture, surface contamination with lithium-containing residual salts) might have been overlooked and wrong conclusions might have been drawn.
This problem was further enhanced by the use of low-quality equipment for sample characterization, which is for example commonly observed for the determination of the average crystallite size from powder XRD analysis. The measurements were performed with laboratory devices with instrumental resolution functions that were not suitable to evaluate LNO samples with crystallite sizes of a few hundred nm as comparably large coherently scattering domains lead to sharp Bragg reflections. This might result in large discrepancies, e.g., average crystallite sizes between 30 nm and 120 nm given by Rietveld refinement and primary particle sizes between several hundred nm and more than 1 µm determined with SEM imaging.[54] Moreover, important material properties were often only qualitatively assessed. The primary particle size was estimated using a single top view SEM image, but the image might not have been representative for the whole sample and no information on the particle size distribution could be gained.[49,50] Besides, the amount of Ni excess was often qualitatively determined by comparing intensity ratios of certain Bragg reflections, but quantitative results can only be achieved by taking the whole powder XRD pattern into account.[51,52]

These considerations led to several requirements for the synthesis parameters and experimental techniques that were applied in this thesis. First of all, a narrow parameter

space in the vicinity of an assumed optimum was used regarding the calcination conditions. Several literature studies revealed that the maximum calcination temperature for the synthesis of well-ordered LNO should ideally be near 700 °C and a rather moderate variation of ± 20 °C around this value was tested. LiOH monohydrate was used as Li source because Li_2CO_3 as alternative choice has a melting point close to the evaluated calcination temperatures, which would lead to a delayed lithiation reaction. Moreover, the use of Li_2CO_3 would lead to a higher amount of carbonate-containing residual salts on the surface of the CAM particles, which is known to be detrimental for LIB operation.[55–58] The number of Li equivalents per mol of Ni was varied independently from the calcination temperature and close to 1.0 to avoid a cost-intensive washing step and to keep the process as simple as possible. In the same sense, $Ni(OH)_2$ precursors prepared by the co-precipitation method were used, which is an industrially scalable process. Precursors with different secondary particle size (d_{50} = 12 µm and 4 µm) were used in order to investigate the influence of this parameter on the physicochemical properties and the electrochemical performance of the calcined materials. All calcinations were performed in pure oxygen atmosphere instead of air, as under these conditions Ni ions can more easily be maintained in the +3 oxidation state. Furthermore, a continuous gas flow (ten furnace volume exchanges per hour) was provided in order to remove the evolving water vapor from the drying of LiOH monohydrate and precursor as well as the lithiation reaction itself.
The temperature profile of the calcination experiments was aligned to industrial feasibility, too. A heating rate of 3 °C min^{-1} was used, which can be considered as a typical value in CAM production in order to reduce the mechanical stress that acts upon the ceramic crucibles. An intermediate step at a moderate temperature of 400 °C for several hours was applied to remove the H_2O from the Li source and the precursor and to initiate the lithiation reaction already between the solid phases. Afterwards, the samples were heated to the maximum calcination temperature without an additional cooling and grinding step, as e.g., applied by Li et al.[30] The overall calcination time disregarding the cooling added up to ∼ 14 h, which is in an acceptable range for large-scale production.

High-brilliance synchrotron radiation was applied as source for the powder XRD measurements, leading to considerably larger scattering intensities and less angular spread compared to a conventional laboratory X-ray source. Thus, a precise evaluation of the Ni excess and the average crystallite size was performed in this thesis. Moreover, the determined off-stoichiometries of the samples were validated by comparison with the results from magnetization measurements and careful analysis of features in the dQ/dV plots from coin half-cell testing.
An automated SEM image segmentation method was introduced to assess the size of a large number of primary particles for several individual secondary particles per sample. With this approach, a proper evaluation of the primary particle sizes and the particle

size distributions was performed. Furthermore, *in situ* analysis of the surface area between CAM and electrolyte was done by an impedance-based method („capacitance measurement"), which has recently been introduced, validated and applied for NCM samples with high Ni content.[59,60] The aforementioned fracturing of the secondary particle structure during electrochemical cycling will alter the surface area between CAM and electrolyte and this can be monitored by the capacitance method. Thus, not only the size of the secondary particle agglomerate and the primary particle size distribution could be determined using SEM imaging, but also the changes concomitant with the fracturing could be assessed. With the detailed analysis of off-stoichiometry and particle morphology of the pristine powder and its changes during cycling, potential correlations of these physicochemical properties with the electrochemical performance in the LIB could be tested.

Electrochemical data published for LNO samples can lead to confusion, too, when comparing the results from different research groups. This can be attributed to a large extent to the differences in the testing setup and the used cycling conditions. Important parameters are the cathode properties (electrode composition regarding the ratio of active material:binder:conductive carbon, mass loading, thickness, press density), the electrolyte solution (concentration of lithium salts, type and ratio of organic solvents), the anode (e.g., Li metal or graphite), the separator (e.g., polypropylene or glass fiber), the temperature present during the cycling test and the test procedure (lower and upper cut-off voltage, charge/discharge current, etc.) A few examples will be given in the following to illustrate this point.
Studies with the synthesis of LNO as topic very often used electrochemical testing conditions far away from today's standards. Bianchi et al. pressed the cathode mixture on a stainless steel grid, used Li metal wires as counter and reference electrode and 1M $LiClO_4$ in propylene carbonate as electrolyte.[40] The upper cut-off voltage was set to 4.1 V vs. Li^+/Li, which limited the achievable charge capacity considerably, compromising the significance of the results for real applications.[45] The current rate was provided in terms of C/10 or C/20 without further specifying to which capacity value C this was related to. Moreover, no information was given regarding the temperature that was present during the test, which can alter the results significantly.[61]
Chang et al. prepared the cathodes using slurry casting and a mixture of CAM, copolymer binder and acetylene black in a 87:5:8 mass ratio.[48] The electrochemical testing was performed with 1M $LiPF_6$ in ethylene carbonate (EC)/dimethyl carbonate (DMC) (2:1 mass ratio) as electrolyte and in a voltage range between 3.1V and 4.4V vs. Li^+/Li. Ronduda et al. used a similar process to prepare the cathodes, but a mixture of CAM, polyvinylidene fluoride (PVDF) and carbon black in a 84:8:8 mass ratio.[54] They used 1M $LiPF_6$ in EC/DMC (1:1 mass ratio) as electrolyte and performed the cycling tests „at room temperature" between 3.0 V and 4.4 V vs. Li^+/Li. Another LNO calcination study utilized a cathode mixture of CAM, PVDF and carbon in a 92:4:4 mass ratio,

1M $LiPF_6$ in EC/diethyl carbonate (DEC)/DMC (1:1:1 mass ratio) as electrolyte and a voltage range between 2.6 V and 4.3 V vs. Li^+/Li.[49]
There were many more differences in the experimental setups used in these studies, but the examples provided herein already show that consistent testing conditions are not observed throughout the literature of synthesis and characterization of LNO. In this thesis, it was intended to partly overcome this issue by providing as many details on the testing procedure as possible. Furthermore, electrode preparation, cathode composition and testing conditions were chosen such that they are close to what is currently used at BASF for CAM evaluation.

2.5 Large-scale cathode active material production

Throughout this thesis, special emphasis was laid on processes that, in principle, could be transferred to industrial production of LNO or the related NCM and NCA materials. Examples are the $Ni(OH)_2$ precursors made by co-precipitation, the rather moderate number of Li equivalents per mol of Ni and the heating rates and dwell times during calcination that represent typical temperature profiles used in CAM production.
At the moment, the CAM manufacturing industry faces severe challenges. First of all, the costs of the CAM represent a significant fraction of the overall LIB cell costs and need to be reduced in order to make BEVs completely competitive with cars powered by an internal combustion engine. The average price of a LIB cell has declined from US$ 290/kWh in 2014 to US$ 110/kWh in 2020, mainly due to economies of scale effects.[62] However, the speed of price decline has slowed down because raw material prices have experienced a significant increase and a supply shortage for certain raw materials comes into sight.[63] This also means that an increase of the LIB cell price in the near future cannot be ruled out.
Nevertheless, the LIB cell production capacity will see a tremendous growth in the next years, which is mainly driven by the ambitious targets of the automotive industry. A recent survey of more than 1000 executives in this field has revealed that BEVs are expected to constitute about 50% of the automotive market in China, Japan, the U.S. and Western Europe by 2030.[64] In 2021 the global production capacity of LIB cells amounted to 755 GWh and with all planned cell production facilities („gigafactories“) taken together it will reach $\sim$ 3.4 TWh in 2030, which corresponds to an increase by a factor of 4.5.[65] Similarly, the annual CAM production capacity is expected to increase from 750 kt in 2021 to $\sim$ 4200 kt in 2030, corresponding to an increase by a factor of 5.6.[66] Of course, these values constitute forecasts and as such are fraught with uncertainty, but the overall trend towards largely increased demand for CAM and LIB cell production capacities will remain. As a consequence, CAM manufacturers are seeking after methods to reduce production costs and to increase production throughput.
Several options are currently under investigation regarding potential cost savings. One

possibility is to reduce the costs on the precursor production stage, where the co-precipitation of transition metal hydroxides is accompanied by the generation of huge amounts of contaminated effluent, which needs to be reprocessed before disposal. Alternative methods are proposed that reuse large parts of the solution from the precipitation process and minimize the amount of generated effluent.[67]
Besides, alternative calcination concepts are under investigation which completely relinquish the co-precipitation process and start from other precursors, e.g., transition metal oxide powders.[68] This „all-dry synthesis“ approach has recently been reported to yield promising results, when a homogeneous distribution of the oxides in the mixture is achieved by appropriate milling conditions.[69] This method admittedly hampers the formation of a spherical secondary particle structure as achieved by co-precipitation. However, it is especially interesting for the synthesis of a relatively new type of CAM, which does not require this secondary particle morphology, as will be pointed out later on.

In this thesis, the idea was to increase the CAM production throughput by the investigation of alternative calcination concepts, but with the commonly used starting materials for the synthesis of LNO, which are $Ni(OH)_2$ precursors made by co-precipitation and $LiOH{\cdot}H_2O$. In large-scale CAM production, the calcination is performed in a continuous process using furnaces, which are called „roller hearth kilns“ (RHKs). These furnaces were originally developed for the mass production of tiles and chinaware and were later on adapted for the high temperature synthesis of cathode and anode active materials. The mixture of starting materials is filled into crucibles („saggers“), which are then transported through the hearth of the kiln with a conveyor made of ceramic rollers. The advantage of this setup compared to batch-type kilns (e.g., shuttle kilns) is that the heating zones of the furnace are constantly at the desired temperature, which means that the overall processing time is shorter. Moreover, no additional kiln furniture needs to be heated up as it is the case for the kiln cars used in tunnel kilns, corresponding to an improved energy efficiency.
Inside the RHK, electric or combustion-type heating elements are placed below and above the saggers to provide heat from both sides and to achieve a preferably narrow temperature distribution in the powder bed. Further progress has been made in recent years to reduce the net CO_2 emission of this technology, e.g., by using hydrogen combustion to fuel the furnace.[70] Preheated gases can be introduced into the hearth compartment to control the atmosphere during calcination.
The heat input is introduced from the sagger walls and, due to the low thermal conductivity of the mixture of precursor and Li source, significant temperature gradients are present and a prolonged time is required to equilibrate the temperature in the powder bed. Note that the temperature gradients occur during both heating and cooling of the powder in the saggers and lead to inhomogeneities in the final product. Depending on the actually present temperature, the lithiation reaction in different sections of the

sagger is progressed or delayed. The same effect is commonly observed to have a significant impact on the crystallite size of CAM powder sampled from specific sections in the sagger. As discussed above, overheating of the material might lead to partial thermal decomposition and to concomitantly worsened electrochemical properties.
At the current development stage, the widely used „RHK 4x2“ configuration includes four saggers side by side, two saggers on top of each other and the total length of the furnace varies between $\sim$ 40 m and 60 m. In order to increase CAM production throughput, an intuitive approach would be to increase the length of the RHK as well as the number of saggers in a row and the number of layers (e.g., „RHK 4x3“ or „RHK 6x2“ configuration). However, this could lead to issues regarding gas flow control and with achieving proper temperature homogeneity.[71] As discussed above, temperature gradients will occur even for the single sagger configuration and it is easy to imagine that this situation will become worse when several saggers are stacked on top of each other. Proper control of the atmosphere during calcination requires a careful adjustment of the gas inlet pipes and becomes increasingly challenging for RHK configurations with a large number of saggers in the cross section of the kiln. Besides, a larger amount of saggers in one row increases the probability for a misalignment of the saggers during operation („meandering“), which will lead to costly production downtime.
A second possibility to increase the production throughput would be to optimize the amount of CAM that is obtained per sagger and heating cycle. For the exemplary starting materials $Ni(OH)_2$ and $LiOH{\cdot}H_2O$, a significant mass loss occurs during calcination, which is caused by H_2O evaporation (see reaction in equation 2.5).

$$LiOH \cdot H_2O + Ni(OH)_2 + \frac{1}{4}O_2 \rightarrow LiNiO_2 + \frac{5}{2}H_2O \tag{2.5}$$

Using the molar masses of $LiOH{\cdot}H_2O$, $Ni(OH)_2$ and $LiNiO_2$ ($41.96\,g\,mol^{-1}$, $92.71\,g\,mol^{-1}$ and $97.63\,g\,mol^{-1}$, respectively), the theoretical mass loss can be calculated and yields $\sim$ 27.5%. Moreover, the bulk density of the mixture of Li source and precursor is quite low, which significantly limits the amount of material that can be loaded into the saggers. This can be attributed to the morphology of the LiOH monohydrate, which is represented by irregularly shaped chunks and leads to an inefficient stacking. The $LiOH{\cdot}H_2O$ used in this thesis was grinded beforehand with an air classifying mill to particle sizes in the range of 10 µm to 20 µm, but the mixture of precursor and the milled LiOH monohydrate still had a bulk density as low as $\sim 1\,g\,cm^{-3}$.
The production throughput could be distinctly improved, if the water is removed before the calcination step, meaning that the $Ni(OH)_2$ is „pre-calcined“ to NiO and the $LiOH{\cdot}H_2O$ is dehydrated to form anhydrous LiOH. In this case, the formation of LNO follows the reaction given in equation 2.6.

$$LiOH + NiO + \frac{1}{4}O_2 \rightarrow LiNiO_2 + \frac{1}{2}H_2O \tag{2.6}$$

Using the above stated molar mass of LNO and the molar masses of LiOH and NiO ($23.95\,\mathrm{g\,mol^{-1}}$ and $74.69\,\mathrm{g\,mol^{-1}}$, respectively), the theoretical mass loss is determined to be $\sim 1\%$ and thus much smaller compared to the one for the reaction in equation 2.5. However, the use of the energy-intensive RHK technology for the separate pre-treatment of precursor and Li source would not be feasible regarding production costs. The pre-calcination of hydroxide precursors and the dehydration of LiOH monohydrate are comparably fast reactions and do not require a long furnace, which predetermines a certain minimum dwell time due to its dimensions. Instead, the water release from the starting materials could be performed in rotary kilns. These furnaces enable fast heating rates of several tens of K per minute, short dwell times and continuous operation. The use of rotary kilns for the formation of anhydrous LiOH has already been documented in patents and is most likely implemented in the industrial production of CAMs.[72] Moreover, the actual application of rotary kilns for the pre-treatment of the precursor materials can be deduced from information provided on the websites of kiln manufacturers.

Nevertheless, the separate pre-treatment and subsequent mixing of Li source and precursor does not solve the issue of low bulk density and poor stacking in the saggers of the RHK. Therefore, CAM producers started to investigate the separation of the chemical reaction between precursor and Li source (afterwards called „partial-lithiation“) at moderate temperatures from the final formation of the layered structure and crystallite growth at high temperatures and disclosed this two-stage process in patents.[73,74] Performing the partial-lithiation in a rotary kiln capable of fast heating and with a uniform temperature distribution in the powder bed could lead to an intermediate product with a low moisture content and increased bulk density, given that the lithiation reaction is fast enough and the process parameters are chosen accordingly. This intermediate product would then be loaded into the saggers for a high temperature calcination step in the RHK, but with much higher sagger loadings compared to a process using a pre-calcined precursor and anhydrous LiOH.

As the completeness of information disclosed in patents is naturally quite limited, a detailed investigation of the intermediate product from the partial-lithiation step is missing. The same holds true for the relationship between the quality of the intermediate product and the properties of the finally calcined CAM and no optimization of the partial-lithiation process parameters has been published until the present day.

Scientific literature on this topic is rather scarce as the investigation of an advanced production process is seldom a target of academia. One study reported the crystal structure of a mixture of $LiOH{\cdot}H_2O$ and $Ni(OH)_2$ after a pre-annealing at 350 °C for 12 h and the authors found a significant degree of lithiation although the temperature was still far below the melting point of LiOH at $\sim 460\,^{\circ}\mathrm{C}$.[75] These findings motivated a deeper investigation of the process parameters of the partial-lithiation step as a progressed lithiation seems to be achievable at rather moderate temperatures. This work was done for LNO as an example, but the outcomes are expected to be transferable to

the related NCM and NCA phases, too.

2.6 Outlook

The publications associated with this thesis revealed that particle morphology is an often overlooked yet decisive parameter for the electrochemical performance of CAMs. It was found that the influence of synthesis conditions on both the crystal structure and the morphology needs to be understood in great detail to be able to achieve optimized materials.

Particle morphology is expected to become even more relevant in the near future as the interest in so-called „single crystal" CAMs has seen a steep increase in recent years. These CAMs do not feature a secondary particle structure, but consist of single or few agglomerated primary particles with diameters of a few µm. The starting point of the excitement related to this material class was most likely a publication by Harlow et al., who presented battery cells comprising single crystal NCM CAM with 50% Ni content, a graphite anode and optimized electrolytes and stated that these cells would be able to power a BEV for more than one million miles.[76] The improved cycling stability of these materials is attributed to the absence of inter-particle fracturing as no cracking of the secondary particle structure can occur for single crystalline materials. However, other degradation mechanisms, e.g., local gradients in Li content and „planar gliding" observed for single particles when charged to too high delithiation degrees, are discussed instead.[77–79]

The synthesis of single crystal CAMs displays new challenges: higher maximum calcination temperatures and larger numbers of Li equivalents per mol of transition metals are used for the solid state reaction compared to polycrystalline materials, which leads to a higher amount of structural defects, more Li residual salts and severe agglomeration of the single particles.[80] Calcination concepts using a large amount of Li excess or molten salts are often discussed in this context, which on the one hand promote the particle growth, but on the other hand require subsequent washing and annealing steps, which should be avoided in industrial-scale production.[81–85]

Without the use of Li excess and molten salts, the single crystal morphology can be achieved by calcination temperatures, which are about 50 °C to 100 °C higher compared to the polycrystalline counterpart. The dwell time at highest temperature might also be extended in order to provide enough energy input to grow particles with the required size. Both scenarios lead to lower calcination throughput and pose a severe challenge to large-scale CAM production. A recently published study revealed that doping elements with large ionic radii (e.g., Cs, K and Ba) can boost the particle growth of single crystalline NCM CAM.[86] This could be a viable approach as it is easy to implement in the existing process, has the potential to lower the maximum calcination temperature and it also seems to reduce the agglomeration degree to some

extent, but more research efforts need to be assigned to this topic. Besides the production throughput issue, single crystal CAMs suffer from lattice defect formation at the high calcination temperatures due to partial thermal decomposition. This could be mitigated by a „temperature-swing synthesis“ , which comprises a first step at very high temperatures for a short time to obtain the single crystal morphology followed by a longer step at moderate temperatures to cure the formed structural defects.[87] This concept was shown to result in better material quality compared to a conventionally prepared single crystal CAM with only one step at very high calcination temperature. However, it was only demonstrated for a CAM with 60% Ni content and future work will show whether this method is also applicable to Ni-rich compositions.
It is evident that particle size and size distribution play a critical role for the electrochemical performance of single crystal cathode materials as well. Thus, the characterization techniques applied in the course of this thesis (automated SEM image segmentation, capacitance method, voltage profile analysis) are believed to be valuable tools for the optimization of these materials. A better understanding of the interplay between structural defects, particle size distribution and electrochemical performance is needed for a successful application of single crystal CAMs. Provided that this knowledge will be generated, these materials can be especially interesting as CAMs for all-solid-state batteries (ASSBs), where mechanical degradation of the cathode-solid electrolyte framework, due to the volume changes of the currently used polycrystalline CAM, has been identified as one important failure mechanism.[88–90] Promising results have been published with the use of single crystal CAMs in ASSBs and further efforts in this direction are highly recommended.[91–94]

Chapter 3

Results and Discussion

$LiNiO_2$ is a well-known compound and several decades have passed since the first observation of its electrochemical activity. Despite the large number of publications dealing with LNO, many open questions regarding its synthesis and characterization remained at the time of the start of this thesis. This can be attributed to a large extent to the lack of detailed information on the preparation conditions, key physical properties and the electrochemical test procedures.
Thus, one goal of this thesis was to perform a calcination study with careful control of the synthesis parameters and special attention to industrial relevance of the used process. The sample preparation was published together with the characterization of the structural chemistry (publication 1). Three independent techniques were applied to assess the deviation of the materials prepared in this thesis from the crystal structure of a perfectly stoichiometric (yet purely hypothetical) LNO sample. Electrochemical tests revealed that for this set of samples the structural chemistry alone cannot explain important aspects of their performance as cathode active materials.
Therefore, special attention was paid to the morphology of the LNO samples (publication 2). Newly implemented methods were used to quantify the particle size and its distribution of the pristine LNO powder as well as the changes during electrochemical cycling. Clear correlations were found and particle morphology was shown to be of utmost importance for the performance of LNO in electrochemical tests.
After a better understanding of the interdependencies between synthesis conditions, physical properties and electrochemical behavior had been established, the focus was laid on the lithiation reaction during LNO preparation in order to obtain a more cost-efficient production process (publication 3). This topic has been addressed by some CAM manufacturers as can be observed in patents, but many open questions remained from a scientific point of view. The synthesis of LNO was again taken as a model system to evaluate a modified preparation process, which would enable a much higher production throughput. Different kiln concepts were used and process parameters were varied for the best suited option. The characterization techniques developed in the

course of the previous work (publication 1 and 2) were applied to the samples prepared with the modified process as well. The minor differences in physicochemical properties and electrochemical performance compared to the conventional preparation opened up a new direction for CAM manufacturing in order to improve the efficiency of the process and to increase the production throughput.

3.1 Publication 1:

The $LiNiO_2$ Cathode Active Material: A Comprehensive Study of Calcination Conditions and their Correlation with Physicochemical Properties. Part I. Structural Chemistry

The first publication of this thesis discussed the sample preparation and the analysis of the structural chemistry. Overall 18 LNO samples were synthesized by using two $Ni(OH)_2$ precursors with different secondary particle size, three maximum calcination temperatures and three numbers of Li equivalents per mol of Ni. The off-stoichiometry values of the LNO samples, meaning the amounts of divalent Ni ions in the Li layer, were evaluated using three independent techniques: powder XRD, magnetization measurements and analysis of the voltage profiles in coin half-cells.
All three techniques yielded the same off-stoichiometry trends when changing the synthesis conditions. However, no correlation between the amount of Ni in the Li layer and the 1^{st} cycle capacity loss was observed, contrary to the common understanding in the literature. A plot of the capacity loss as a function of average crystallite size from Rietveld refinement suggested an important role of particle morphology.

The publication was written by the author and F. Riewald and edited by the co-authors. The experiments were planned by the author, F. Riewald and H. Sommer. The material preparation and electrochemical testing was done by the author and F. Riewald. The powder XRD experiments were performed by F. Fauth and the BL04-MSPD beamline team at the ALBA synchrotron and the Rietveld refinement was done by the author, F. Riewald and M. Bianchini. The SEM imaging was perfomed by the author and F. Riewald. The magnetization measurements were done at the group of Prof. T. Fässler at the Technical University of Munich and were evaluated by F. Riewald.

P. Kurzhals, F. Riewald, M. Bianchini, H. Sommer, H.A. Gasteiger, J. Janek, *A Comprehensive Study of Calcination Conditions and their Correlation with Physicochemical Properties. Part I. Structural Chemistry*, Journal of the Electrochemical Society **168**, 110518 (2021)

Journal of The Electrochemical Society, 2021 **168** 110518

The $LiNiO_2$ Cathode Active Material: A Comprehensive Study of Calcination Conditions and their Correlation with Physicochemical Properties. Part I. Structural Chemistry

Philipp Kurzhals,[1,2,=,z] Felix Riewald,[1,3,=] Matteo Bianchini,[1,4,*] Heino Sommer,[1] Hubert A. Gasteiger,[3,] and Jürgen Janek[2,z,*]**

[1]*BASF SE, New Battery Materials and Systems, D-67056 Ludwigshafen, Germany*
[2]*Institute of Physical Chemistry & Center for Materials Research, Justus Liebig University, D-35392 Giessen, Germany*
[3]*Chair of Technical Electrochemistry, Department of Chemistry and Catalysis Research Center, Technical University of Munich, D-85748 Garching, Germany*
[4]*Battery and Electrochemistry Laboratory (BELLA), Institute of Nanotechnology, Karlsruhe Institute of Technology (KIT), Hermann-von-Helmholtz-Platz 1, 76344 Eggenstein-Leopoldshafen, Germany*

Following the demand for increased energy density of lithium-ion batteries, the Ni content of the Nickel-Cobalt-Manganese oxide (NCM) cathode materials has been increased into the direction of $LiNiO_2$ (LNO), which regained the attention of both industry and academia. To understand the correlations between physicochemical parameters and electrochemical performance of LNO, a calcination study was performed with variation of precursor secondary particle size, maximum calcination temperature and Li stoichiometry. The structural properties of the materials were analyzed by means of powder X-ray diffraction, magnetization measurements and half-cell voltage profiles. All three techniques yield good agreement concerning the quantification of Ni excess in the Li layer (1.6%–3.7%). This study reveals that the number of Li equivalents per Ni is the determining factor concerning the final stoichiometry rather than the calcination temperature within the used calcination parameter space. Contrary to widespread belief, the Ni excess shows no correlation to the 1st cycle capacity loss, which indicates that a formerly overlooked physical property of LNO, namely primary particle morphology, has to be considered.
 [DOI: 10.1149/1945-7111/ac33e5]

Manuscript submitted August 29, 2021; revised manuscript received October 20, 2021. Published November 9, 2021.

The current generation of lithium-ion batteries (LIBs) requires further improvements to ease the commercialization and strengthen the market share of battery electric vehicles (BEVs).[1–3] While all parts of the battery cells are targeted by researchers, one of the key components under investigation is the cathode active material (CAM), as it is the main cost driver of the overall electrochemical cell and it strongly affects the achievable energy and power density.[4] Although the interest in olivine $LiFePO_4$ as low-cost CAM with moderate specific capacity recently has risen and other alternatives such as spinel $Li(Mn,Ni)_2O_4$ and overlithiated Li-rich and Mn-rich cathodes are currently examined,[5] the predominant choice of materials are the layered transition metal oxides $Li(Ni_{1-x-y}Co_xMn_y)O_2$ (NCM) and $Li(Ni_{1-x-y}Co_xAl_y)O_2$ (NCA). These show a good compromise between high power and high energy density applications at sufficiently low cost and, provided that the Co content is minimized, raw material abundancy.[6] Driven by the requirements of BEV manufacturers for further driving range increase and reduction of costs, the Ni content of these layered transition metal oxides has been increased over the past years and the market share of BEVs using LIBs with Ni contents of 80% and above is expected to significantly increase in the near future.[7] With increasing Ni fraction in the CAM, the extractable amount of Li increases (and thus, the achievable capacity and resulting energy density at a fixed voltage cut-off), but this comes at the cost of reduced cycling stability.[8,9] Ni-rich NCM and NCA phases tend to show increased degradation, involving the bulk and most importantly the surface of the CAM. For example, oxygen loss at high degree of delithiation is connected with decomposition of the surface structure (densification towards rock salt-like structure), while large anisotropic crystal lattice changes (total change of unit cell volume during charge of e.g. $\sim$ 5% for $Li(Ni_{0.8}Co_{0.1}Mn_{0.1})O_2$) eventually lead to particle fracture.[10–13] Major efforts have been spent to chemical stabilization approaches like bulk substitution with other elements or surface modification in form of thin coatings on the particles.[14–18] Novel approaches also involve material modifications to address the fracturing issue by optimizing the particle morphology (single crystal or rather monolithic materials).[19] Moreover, intentional orientation of primary particles in radial direction was introduced to better accommodate the volume changes during cycling. Materials with transition metal concentration gradients were also investigated, which reduce the amount of reactive Ni in contact with the liquid electrolyte.[20–22]

Unfortunately, in comparison to the originally commercialized layered compound $LiCoO_2$, NCM- and NCA-type materials suffer from poor 1st cycle coulombic efficiencies, a clear limitation that has to be better understood to fully exploit the potential of this class of cathode active materials.[23–26] Due to such a 1st cycle capacity loss, not all the deintercalated Li can be reintroduced into the CAM structure during discharge. $LiNiO_2$ (LNO) as the 100% Ni end member of the NCM and NCA materials is the natural model system to investigate this effect. Early research showed that LNO always tends to be Li deficient and contains an excess of Ni^{2+} ("Ni excess" or "off-stoichiometry") in the Li layers, despite optimized calcination conditions, leading to a stoichiometry of $Li_{1-z}Ni_{1+z}O_2$.[27–29] Incomplete oxidation and deficiency of Li_2O leads to the solid solution of $LiNiO_2$ ($z = 0$) and NiO ($z = 1$), where $2z$ Ni^{2+} ions are present with half of them located in the Li layer and the other half in the Ni layer. This Ni excess was shown to have a significant impact on physical and electrochemical properties, e.g. on magnetic properties and phase transitions during cycling.[30]

A commonly found hypothesis throughout the literature is the connection between the poor 1st cycle coulombic efficiency and the excess Ni^{2+} in the Li layers.[31–33] Numerous reports on the synthesis of near-stoichiometric LNO were published, but the general approach in the literature is to vary one or more calcination parameter(s) in large steps to see clear effects on the resulting physicochemical properties and electrochemical performance.[27,31,34–36] Unfortunately, this often leads to conclusions that are hard to generalize and could be easily misinterpreted. Furthermore, in industrial optimization processes narrow parameter ranges are considered in contrast to academia, where a more fundamental understanding is intended.

Therefore, the goal of this study is to systematically vary multiple calcination parameters (secondary particle size of hydroxide

[=]These authors contributed equally to this work.
*Electrochemical Society Member.
**Electrochemical Society Fellow.
[z]E-mail: philipp.kurzhals@basf.com; juergen.janek@pc.jlug.de

precursor, number of Li equivalents per mole of Ni, maximum calcination temperature) with the aim to prepare $Li_{1-z}Ni_{1+z}O_2$ with minimized z values, and to thoroughly analyze the resulting physicochemical properties. In this first part of the study, synchrotron powder X-ray diffraction (PXRD), measurements of the magnetic properties and 1st cycle voltage profile analysis are performed to properly quantify the stoichiometry of the samples in terms of Ni excess in the Li layers. Afterwards, the obtained values are compared to the 1st cycle capacity loss. In a forthcoming and complementary study, we will investigate the relationship between primary particle morphology, its evolution upon cycling and the electrochemical performance.

Experimental

Calcination of $LiNiO_2$.—LNO samples were calcined through a solid-state synthesis route starting from the base materials $Ni(OH)_2$ and $LiOH{\cdot}H_2O$. Two commercial batch-type $Ni(OH)_2$ precursors (Hunan Zoomwe Zhengyuan Advanced Material Trade Co., Ltd.) with two distinct secondary particle sizes (d_{50} values of (12 ± 0.5) μm and (4 ± 0.5) μm, respectively, Fig. 1c) were utilized, further on referred to as "12 μm precursor" and "4 μm precursor." $LiOH \cdot H_2O$ was used as Li source (Albemarle Corporation), which was ground prior to the synthesis with an air classifying mill to obtain particles of ∼ 10–20 μm. 50 g of $Ni(OH)_2$ and the respective amount of $LiOH \cdot H_2O$ to get the defined number of Li equivalents per mol of Ni were mixed using a laboratory blender (Kinematica AG). Three different numbers of Li equivalents (0.98, 1.01 and 1.04) were utilized in this study. Afterwards, this premix was filled into a ceramic crucible and fired in a laboratory box-type furnace (Linn High Therm GmbH). An overview of the used calcination conditions and the color and shape coding for the samples used in all figures throughout this study are shown in Fig. 1a. A schematic of the calcination profile is shown in Fig. 1b. First, the temperature was ramped up to 400 °C and fixed for four hours and then the temperature was ramped up to the respective maximum calcination temperature T_{max} (680 °C, 700 °C and 720 °C, respectively) and was kept for six hours. For both steps a heating rate of 3 °C min^{-1} was chosen. This calcination profile was selected to be as close as possible to an industrially feasible process. Thus, a moderate heating ramp and dwell times, that result in an overall calcination time of ∼ 14 h, were chosen. An additional cool-down and grinding step after the 400 °C hold was avoided as this would not be part of industrial practice. All experiments were run in pure oxygen atmosphere (flow rate of 100 liters per hour corresponding to about ten furnace-volume exchanges per hour). After the synthesis the samples were cooled down to 120 °C and brought to a dry room (21 °C, dew point < −40 °C) inside a gas-tight box to prevent reactions with ambient moisture and CO_2. Handling of dry CAM powders was generally done in the dry room. Prior to characterization of the materials and the electrode preparation, the powders were sieved using sieves with a mesh size of 32 μm (Retsch GmbH).

Scanning electron microscopy (SEM) imaging.—A small amount of cathode powder was fixed on a SEM pin holder (Agar Scientific, Ltd.) covered with conducting carbon cement (Plano GmbH). A 6 nm thick platinum layer was added by sputter deposition (SCD 500 Sputter Coater, Bal-Tec AG). Measurements were performed using a SEM with a thermal field emission cathode and an Everhart-Thornley secondary electron detector at an operating voltage of 5 kV (Ultra 55, Carl Zeiss AG).

Powder X-ray diffraction.—Synchrotron powder X-ray diffraction (PXRD) measurements were performed at the ALBA synchrotron. The measurements at ALBA were carried out at the BL04-MSPD beamline[37] at a wavelength of $\lambda = 0.62001$ Å (calibrated using a Si NIST standard) using a Si 111 monochromator and the MYTHEN position sensitive detector in 2θ angular range of 2°−82°.

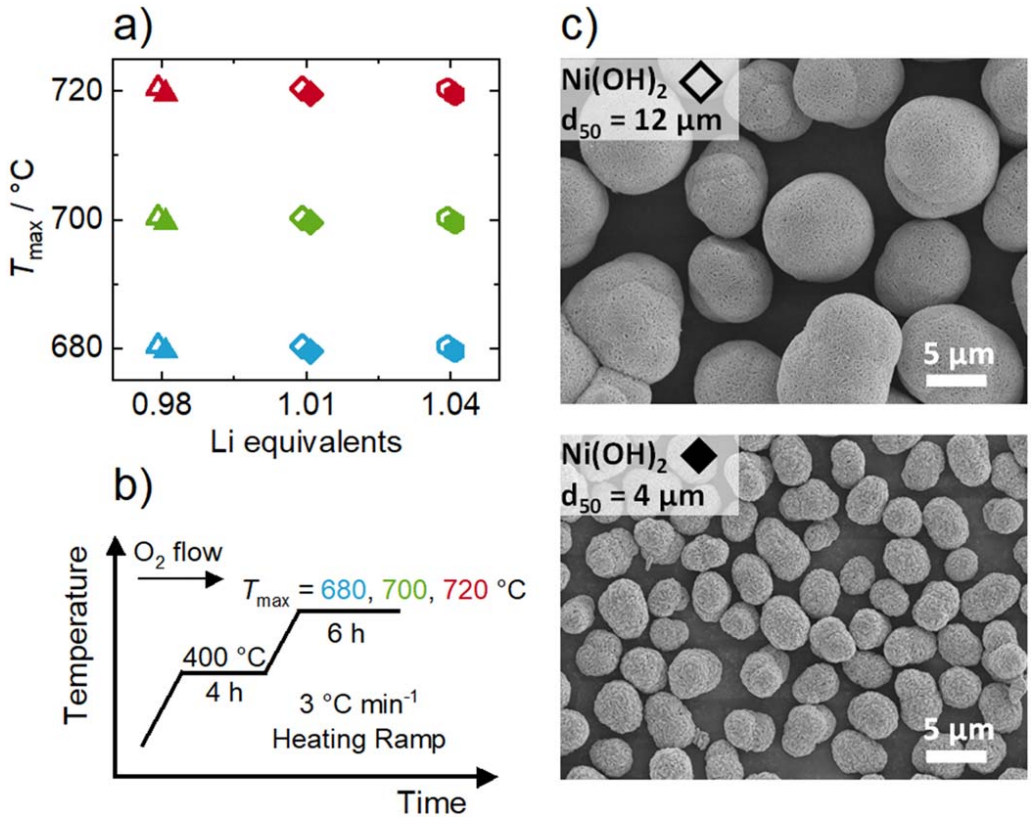

Figure 1. Overview of the samples prepared for this study. (a) Calcination conditions employed, with color referring to three different maximum calcination temperatures T_{max} (680 °C: blue, 700 °C: green, 720 °C: red) and symbols indicating three different Li equivalents per mol of Ni (0.98: triangles, 1.01: diamonds, 1.04: hexagons). (b) Temperature profile used for calcination. (c) Top view SEM images of the two chosen $Ni(OH)_2$ precursors (precursor with d_{50} of ∼ 12 μm marked by empty symbols and precursor with d_{50} of ∼ 4 μm marked by filled symbols in (a), respectively). In summary, 18 different samples were prepared.

The LNO samples were filled in borosilicate capillaries of 0.7 mm diameter, sealed by flame, and mounted on a spinning sample holder. Data were collected in Debye–Scherrer geometry for 27 different positions of the detector, and a long data acquisition time of 30 s was chosen for each position in order to obtain high intensity patterns. Rietveld refinement was done using the Fullprof software package.[38] For each sample a new background for the measured diffraction pattern was determined with the WinPLOTR software[39] and corrected by visual inspection. The refinements were based on a hexagonal α-$NaFeO_2$ structure with the $R-3m$ space group.[40] The instrumental broadening was determined by measuring a NAC ($Na_2Ca_3Al_2F_{14}$) standard in the same sample configuration. The model used for the fitting is based on Thompson-Cox-Hastings pseudo-Voigt convoluted with axial divergence asymmetry functions. Using the instrumental resolution function, the sample contribution to the peak broadening was determined: with the angular dependence of the peak broadening related to a finite crystallite size described by the Scherrer equation, a volume-averaged value of the crystallite size was obtained.[41] Refinement of the parameters of the structural model was done for consecutive iteration cycles until convergence was reached and the quality of the fit was checked by inspection of R_{wp} (weighted profile factor with all non-excluded points) and R_{Bragg} (Bragg R-factor) as well as χ^2 (reduced chi-square). For all samples, in the final iteration 12 parameters were refined: scale factor, zero shift, a and c unit cell parameters, U, X, Y as parameters of the Gaussian (U) and Lorentzian (X, Y) contribution to the pseudo-Voigt function, fractional atomic coordinate of oxygen z_{ox}, occupancy of Ni on Li site (assuming site remains fully occupied), B_{iso} (isotropic displacement parameter) of O, Ni and of Li. According to the recent report of Yin et al., Li and O were treated using the ionic form factors while the atomic form factor was applied for Ni.[42] Note that fully atomic and fully ionic form factors were also tested; these resulted in acceptable fits but with slightly larger R_{Bragg} values and too low $B_{iso}(Li) \approx 0.3$ Å^2. Yet, all trends reported in this paper would be preserved by a different choice, with an offset of Ni on the Li site of only $z \approx 0.003$. For the two samples of this study (720 °C and 1.04 li equiv.) having the largest crystallite size and therefore smallest peak broadening, the asymmetric shape of the Bragg peaks at low θ was accounted for by two additional parameters refined at a LeBail fit stage, but then constrained later during the Rietveld fit. For all refinements, final values of $R_{wp} < 11$ and $R_{Bragg} < 3$ were obtained. Error bars are reported as 3σ, where $\sigma$is the error obtained from the Fullprof software.

Magnetization measurements.—The temperature and field dependent magnetization of the pristine powders was measured by a Superconducting Quantum Interference Device (SQUID, MPMS 5XL, Quantum Design Inc.). For each measurement $\sim$ 40 mg of the respective powder was filled into a gelatine capsule, which was then centrally fixed in a plastic straw. The straw was mounted onto the sampling rod of the SQUID. For the field dependent magnetization, the external magnetic field was scanned between −50 and 50 kOe (−5 to 5 T). The measurement was repeated at 300 and 2 K. For the determination of the Weiss constant, a field warming curve of the magnetic susceptibility at an external magnetic field of 10 kOe between 2 and 300 K was recorded. The diamagnetic contribution of the capsule was substracted from the signal. To account for the diamagnetic contribution of the Li and O ions, the susceptibility was corrected by the use of Pascal's constants.[43]

Electrochemical characterization.—Electrodes for electrochemical characterization were prepared by mixing the CAM powders with conductive carbon (C65, Imerys Graphite & Carbon) and PVDF binder (Solef 5130, Solvay GmbH) in a 94:3:3 mass ratio. For this, a 7.5 wt% binder solution in N-methyl-2-pyrrolidone (NMP, BASF SE) was mixed with additional NMP and the conductive carbon, and mixed for at least 24 min at 2000 rpm in a planetary mixer (ARE 250, Thinky Corporation). The CAM powders were added to the obtained slurry and were mixed for additional 10 min. The solid content of the final slurries was 61 wt%. The slurries were cast onto an Al-foil (thickness 20 μm, Nippon Light Metal Co., Ltd.) using a box-type coater (wet-film thickness 100 μm, width 6 cm, Erichsen GmbH & Co. KG) and an automated coating table (5 mm s^{-1}, Coatmaster 510, Erichsen GmbH & Co. KG). The coated tapes were placed in a vacuum oven (VDL 23, Binder GmbH) and heated to 120 °C under vacuum for drying overnight. The dried cathode tapes were compressed using a calender (CA5, Sumet Systems GmbH) at a set line-force of 30 N mm^{-1} and a roller speed of 0.5 m min^{-1}. Circular electrodes with a diameter of 14 mm were punched out using a high-precision handheld punch (Nogamigiken Co., Ltd). After weighing, the electrodes were transferred to an Ar filled glovebox for cell assembly. An average loading of (8.0 ± 0.5) mg cm^{-2} and an electrode density of (3.0 ± 0.2) g cm^{-3} were obtained. Coin half-cells were built using a 2032 coin cell geometry. The cell stack consisted of the cathode, a glass fiber separator (ø 17 mm, 300 μm thickness, GF/D, VWR International, LLC.) soaked with 95 μl electrolyte (LP57, BASF SE) and a pre-punched Li anode (ø 15.8 mm, thickness 0.58 mm, purity 99.9%, Shandong Gelon LIB Co., Ltd). After assembly the cells were crimped and closed in an automated crimper (Hohsen Corp.). The cells were then transferred to a climate chamber (Binder GmbH) and connected to a battery cycler (Series4000, MACCOR, Inc.). All tests were performed at 25 °C and the C rates were defined according to 1 C = 200 mAg^{-1}.

Results and Discussion

Synchrotron PXRD measurements and refinement.—The layered compound $LiNiO_2$ is known to crystallize in a rhombohedral unit cell, isostructural with α-$NaFeO_2$ with the space group $R-3m$.[30,44,45] The layered character of this structure is induced by the different ionic radii of $r(Li^+) = 76$ pm, $r(Ni^{2+}) = 69$ pm and $r(Ni^{3+}{}_{LS}) = 56$ pm (LS = low spin).[46] The oxygen anions on the 6c sites form a cubic close packed lattice and the octahedral interstices are occupied by the Ni and Li cations in the 3a (0, 0, 0) and 3b (0, 0, 0.5) sites, respectively. In this work, only small deviations from perfect stoichiometry in the form of $Li_{1-z}Ni_{1+z}O_2$ were assumed for the Rietveld refinement, which will be substantiated in the following chapter.

Exemplary results of three selected samples from this study with clear variation of calcination conditions are shown in Fig. 2. PXRD patterns of the samples prepared with the 12 μm $Ni(OH)_2$ (blue: 680 °C, 0.98 li equiv.; green: 700 °C, 1.01 li equiv.; red: 720 °C, 1.04 li equiv.) are depicted in Fig. 2a, demonstrating that LNO with good crystallinity and characteristic reflections is obtained for all employed calcination conditions. The low background and high signal-to-noise ratio indicate the high data quality of the synchrotron setup, which was also observed in other studies on LNO.[47,48] The magnified views of the 003 peak and of the 108 and 110 peaks in Figs. 2b and 2d, respectively, illustrate the distinct impact of the calcination conditions on crystal structure and morphology. A shift of the peak position to higher scattering angles concomitant with a decrease in full-width-at-half-maximum (FWHM) with increasing maximum calcination temperature T_{max} and Li equivalents is observed. The different angular peak positions are related by Bragg´s law to different lattice parameters for the investigated samples, whereas changes of the peak FWHM are connected to different average crystallite sizes. The observations made for increasing T_{max} and Li equivalents are in line with a decrease in unit cell volume and an increase in average crystallite size. Figure 2c shows a selected angular range, where peaks from Li-containing impurities arise, which can be assigned to LiOH, Li_2CO_3 and Li_2SO_4. LiOH and Li_2CO_3 are present as products of unreacted Li_2O with moisture and CO_2 from ambient air after calcination,[49,50] despite fast transfer to a dry room. In the literature, these impurities were shown to be located on the surface of the secondary particles.[51,52] The formation of Li_2SO_4 is plausible regarding the residual sulfur content of the precursor after precipitation starting

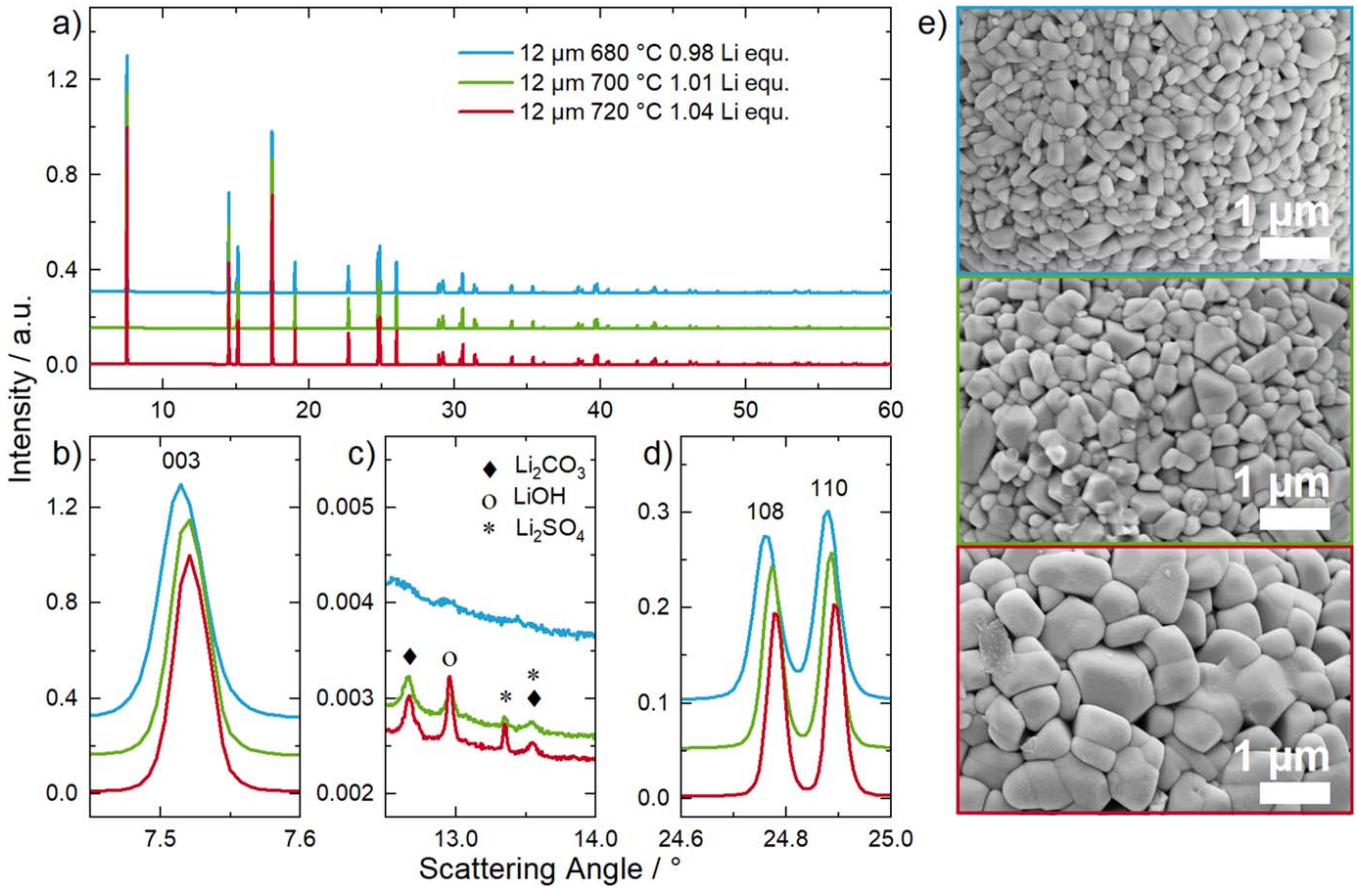

Figure 2. Synchrotron X-ray diffraction patterns and top view SEM images of three exemplary samples prepared from the 12 μm $Ni(OH)_2$ precursor, for which 0.98 Li equivalents and 680 °C (blue), 1.01 Li equivalents and 700 °C (green) and 1.04 Li equivalents and 720 °C (red) were used as calcination conditions. (a) Full PXRD pattern in the range of $2\theta = 5°-60°$. (b) Zoom-in of the 003 Bragg peak. (c) Selected peaks assigned to the Li impurities Li_2CO_3 (diamond), LiOH (circle) and Li_2SO_4 (asterisks). (d) Zoom-in of the 108 and 110 Bragg peaks. The data was collected at the BL04-MSPD beamline of the ALBA synchrotron at a set wavelength of $\lambda = 0.62$ Å. (e) Top view SEM images of the three samples in 20 k magnification.

from $NiSO_4$ feeds, as found for other Ni-rich compositions as well.[53] Nevertheless, the contribution of these impurities to the overall PXRD patterns is very small as a large magnification (x200) is required to make them visible. Therefore, the impurities are assumed to not have a detrimental impact on the subsequent refinement of the structural model. To give an overview of the samples' morphology, top view SEM images in 20 k magnification are depicted in Fig. 2e. All CAM samples show distinct primary particles that form a secondary particle agglomerate, which resembles the morphology of the $Ni(OH)_2$ precursor. Increasing both the number of Li equivalents and T_{max} leads to a clear increase of primary particle size, which will be studied in more detail in a forthcoming report.

To quantify the aforementioned observations, Rietveld refinement of the parameters of the structural model against the PXRD data was performed. The main results of the refinement are summarized in Fig. 3 and all results including error bars can be found in Table I. In Figs. 3a and 3b, the Ni occupancy on the Li site is depicted as a function of T_{max} and the Li equivalents, respectively. Thermal decomposition is an often discussed topic for the synthesis of LNO, as it already occurs at temperatures close to the calcination temperature required to form the stoichiometric compound.[47,54] In this case, the layered LNO decomposes towards the parent rock salt-type NiO phase (i.e. z increases in $Li_{1-z}Ni_{1+z}O_2$), releasing O_2 and Li_2O, following the backward reaction shown in Eq. 1. The formed Li_2O is hypothesized to be oxidized to Li_2O_2, which is assumed to be very volatile.[54,55] However, this topic is still under debate and there is evidence in the literature that the proposed mechanism is not very likely to happen.[56] Although a slight increase in off-stoichiometry at a higher T_{max} is observed in Fig. 3a, the differences between samples with the same number of Li equivalents are very small and could presumably not be resolved with a conventional laboratory X-ray setup in contrast to the data acquired at the synchrotron. Therefore, the PXRD analysis shown in Fig. 3a suggests that there is no evidence for a significant impact of thermal decomposition or Li loss into the vapor phase at these calcination temperatures. However, with increasing Li equivalents, a clear decrease in Ni excess in the Li site can be seen in Fig. 3b, indicating the formation of a more stoichiometric LNO with a higher Li excess in the calcination process. Considering reaction Eq. 1, this observation follows Le Chatelier´s principle, because a higher amount of Li excess in the calcination pushes the chemical reaction towards the formation of $LiNiO_2$ as part of the solid solution with NiO.

$$\frac{1}{1+z}Li_{1-z}Ni_{1+z}O_2 + \frac{z}{1+z}Li_2O + \frac{z}{2(1+z)}O_2 \rightleftharpoons LiNiO_2 \quad [1]$$

The results are in good agreement with literature reports showing that the synthesis of LNO samples close to ideal stoichiometry requires a sufficient amount of Li excess.[36,57] However, these studies often used large increments of Li excess or such high amounts (starting from 7–10 mol% and up to 300 mol%), that a washing step afterwards is necessary to remove residual Li salts after calcination. In terms of raw material costs, this approach is not economically feasible and a washing step should be avoided, which is why the Li excess in this work was limited to 4 mol%. Finally, it should be mentioned that it is possible to synthesize Li-rich compounds related to Li_2NiO_3 by a simple solid-state method using the same starting materials employed in this study, even though more oxidizing

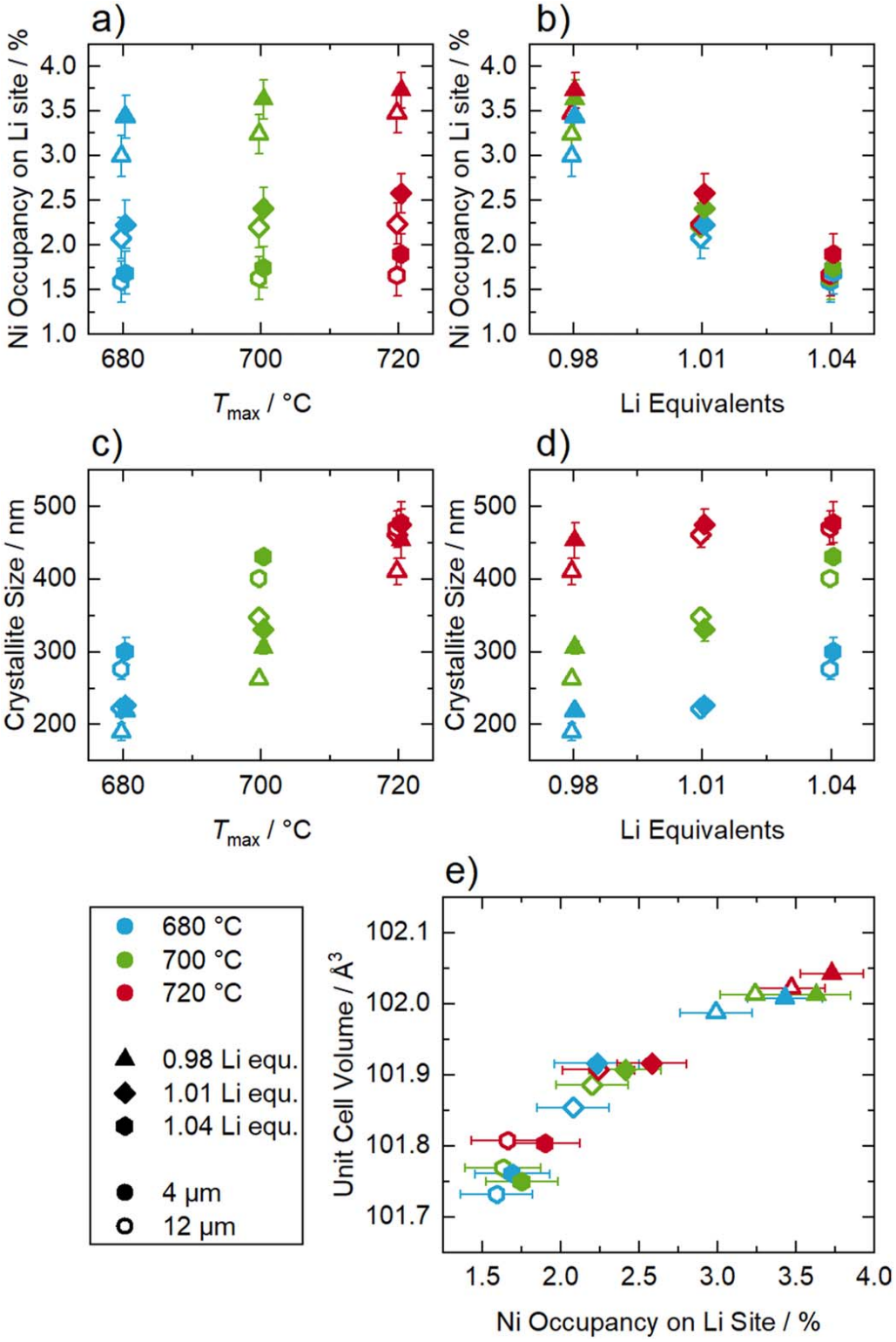

Figure 3. Results of the Rietveld refinement for all LNO samples prepared in this study. All samples were refined assuming Ni excess in the Li layer (sum formula of $Li_{1-z}Ni_{1+z}O_2$). (a) Ni occupancy on the Li site vs the maximum calcination temperature T_{max} (680 °C: blue, 700 °C: green, 720 °C: red) and (b) Ni occupancy on the Li site vs the Li equivalents per mol of Ni added to the calcination (0.98: triangles, 1.01: diamonds, 1.04: hexagons). Samples prepared from the 4 μm precursor are depicted as filled, samples prepared from the 12 μm precursor are shown as empty symbols. (c) and (d) depict the refined crystallite size vs T_{max} and Li equivalents, respectively. For better readability, 4 μm and 12 μm samples are slightly offset in x-direction. e) Correlation between the Ni occupancy on the Li site and the refined unit cell volume.

conditions are needed in this case to raise the oxidation state of Ni to values larger than +3 (lower calcination temperature and higher Li excess).[48] Thus, the occurrence of overlithiation can be excluded for the materials prepared in this work.

Figures 3c and 3d depict the average crystallite size from Rietveld refinement as a function of maximum calcination temperature and the Li equivalents. Here, the refined crystallite size shows a clear dependence on T_{max} (from 680 °C to 720 °C) leading to an

Table I. Results of the Rietveld refinement for all samples calcined in this study: Ni occupancy on the Li sites, unit cell volume (UCV), average crystallite size, fractional atomic coordinate of oxygen z_{ox}, B_{iso} of O, Ni and Li. R_{Bragg}, R_{wp} and χ^2 are depicted to underline the goodness of the refinement.

Sample	Ni occ./%	UCV/Å^3	Size/nm	z_{ox}	B_{iso} O	B_{iso} Ni	B_{iso} Li	R_{Bragg}	R_{wp}	χ^2
				12 μm						
0.98 680 °C	3.0(2)	101.987	189(12)	0.2585(2)	0.94(4)	0.358(8)	0.7(1)	2.33	9.51	33.8
0.98 700 °C	3.2(2)	102.013	263(6)	0.2586(2)	0.92(3)	0.346(8)	0.8(1)	2.03	8.96	33.2
0.98 720 °C	3.5(2)	102.022	410(19)	0.2585(2)	0.97(3)	0.395(8)	0.9(1)	1.72	8.82	40.0
1.01 680 °C	2.1(2)	101.854	222(11)	0.2586(2)	0.92(4)	0.354(8)	0.8(1)	2.21	9.54	35.6
1.01 700 °C	2.2(2)	101.886	348(10)	0.2586(2)	0.99(3)	0.426(8)	0.9(1)	1.85	9.14	44.4
1.01 720 °C	2.2(2)	101.907	461(16)	0.2586(2)	0.97(3)	0.407(8)	0.9(1)	1.71	9.40	47.4
1.04 680 °C	1.6(2)	101.732	277(15)	0.2586(2)	0.92(3)	0.384(8)	0.9(2)	1.84	9.41	48.2
1.04 700 °C	1.6(2)	101.769	401(4)	0.2586(2)	0.93(3)	0.377(8)	0.9(2)	1.62	9.52	47.5
1.04 720 °C	1.7(2)	101.808	470(23)	0.2587(2)	0.93(3)	0.386(8)	0.9(1)	1.74	9.26	44.2
				4 μm						
0.98 680 °C	3.4(2)	102.008	219(7)	0.2583(2)	0.97(4)	0.383(9)	0.9(1)	2.07	9.85	61.9
0.98 700 °C	3.6(2)	102.012	306(9)	0.2583(2)	0.96(3)	0.386(8)	0.9(1)	2.11	9.14	63.1
0.98 720 °C	3.7(2)	102.042	453(25)	0.2583(1)	1.02(3)	0.442(7)	0.9(1)	1.86	7.98	46.2
1.01 680 °C	2.2(3)	101.916	227(9)	0.2585(2)	1.02(4)	0.428(10)	0.9(2)	1.87	10.8	81.0
1.01 700 °C	2.4(2)	101.907	331(17)	0.2585(2)	0.94(4)	0.369(8)	0.9(1)	1.78	9.39	57.3
1.01 720 °C	2.6(2)	101.916	475(21)	0.2584(2)	0.97(3)	0.402(8)	0.9(1)	1.70	8.86	57.8
1.04 680 °C	1.7(2)	101.761	301(19)	0.2585(2)	0.96(4)	0.414(9)	1.0(2)	1.74	9.66	69.5
1.04 700 °C	1.8(2)	101.750	432(9)	0.2586(2)	0.95(3)	0.409(8)	1.0(2)	1.53	8.99	64.1
1.04 720 °C	1.9(2)	101.804	478(28)	0.2586(2)	0.99(3)	0.443(8)	1.0(1)	1.51	8.64	53.7

increase of average crystallite size by a factor of ~ 2 (200−300 nm to 400−600 nm) for the two utilized precursors. During the high temperature hold, larger crystallites grow at the expense of smaller ones to reduce the free surface energy of the system, a process which is promoted by higher calcination temperatures.[58] Few reports exist on the dependence of the crystallite size on the calcination temperature for polycrystalline LNO or NCM compounds.[59,60] However, these reports claim average crystallite sizes below 100 nm for LNO and Ni-rich NCM calcined under comparable conditions, which could be ascribed to the very different starting precursors or to limitations of the PXRD setups used in these studies.

For a given T_{max}, an increase in average crystallite size with increasing Li equivalents is also observed (Fig. 3d), although the impact is less pronounced compared to the one of the calcination temperature (Fig. 3c). Parts of the molten Li source can act as a flux before it completely reacts with NiO at elevated temperatures, which can promote the growth of already present crystallites similar to other flux methods.[61] However, in the chosen range of calcination parameters, the calcination temperature is always the more decisive factor for the crystallite size compared to the number of Li equivalents. Following the current trend in research moving from polycrystalline materials to single crystal morphology, the finding that the crystallite size increases with T_{max} and Li excess is in good agreement with typical approaches to calcine materials with monolithic structures.[19,62] In comparison to these methods, the calcination conditions from this study are however rather moderate, with the final CAM still maintaining the polycrystalline secondary particle structure of the precursors. It must be mentioned that the crystallite size should not be confused with the primary particle size that can be seen in the SEM images in Fig. 2e. The term "crystallite size" here refers to the size of the coherently scattering domains, and each primary particle can consist of one or more of these crystallites.[63] Moreover, the Rietveld refinement provides only values of the crystallite size averaged over the whole powder sample. There are methods to extract the particle size distribution from Rietveld refinement, although they depend on the assumption of a certain distribution function.[64] Quantitative information on the primary particle size distribution can be obtained with SEM image segmentation and the respective results for this calcination study will be presented in a forthcoming report.'

Figure 3e depicts the unit cell volume as a function of the Ni occupancy on the Li site. As shown in the literature, the unit cell volume shows a linear increase with increasing Ni excess (Vegard´s law along the NiO-$LiNiO_2$ solid solution).[36,65] So far it was difficult to show this relation for $Li_{1-z}Ni_{1+z}O_2$ with small values of z due to the scattering of data points for materials made by different groups and measured with different instruments. However, here this relationship can be confirmed even for $0.016 \leqslant z \leqslant 0.037$, refining the parameters of the structural model, which is based on the observed high-quality synchrotron PXRD data. Extrapolation to $z = 0$ leads to a unit cell volume of 101.56 Å^3, which is in line with other reported extrapolations for LNO with ideal stoichiometry.[30]

In principle, a second scenario in competition to the off-stoichiometry would be possible with Li/Ni antisite defects, i.e. a site exchange of small amounts of Li and Ni (often called "Li/Ni disorder" or "Li/Ni exchange").[28] This kind of defect is often discussed for NCM compositions, and the formation energy of such defects was shown to be dependent on the total fraction of Ni^{2+} ions.[66] Thus, it is frequently observed for materials which contain Mn^{4+} as this requires an equal amount of Ni^{2+} for charge compensation. For LNO, however, which contains virtually no Ni^{2+}, the energy required to form antisite defects is very large (> 340 meV defect^{-1}) and off-stoichiometry is considered the dominating source of defects. Due to the small Li X-ray cross-section, directly proving the defects´ nature is difficult. However, neutron diffraction studies showed that for small Li deficiency (namely $z = 0.02$ or 0.07), no Li/Ni disorder occurred and mixing was only determined for a large deficiency of $z = 0.25$.[67] In other studies, researchers also suggested oxygen vacancies in LNO in the context of synthesis under pressurized oxygen atmosphere and claimed the representation $Li_{1-z}Ni_{1+z}O_{2-y}$ to account for these oxygen vacancies.[68] The formation energy of oxygen vacancies was examined by DFT calculations, and vacancy formation could become energetically favorable at high temperatures during calcination, but this is more likely to happen at the surface and especially in the delithiated state.[69,70] However, as oxygen vacancies were never confirmed for LNO using neutron diffraction measurements, they were not included in the structural model used in this study. The general goodness of the Rietveld refinement for all investigated samples (see Table I) and the observed continuation of the linear

relationship between unit cell volume and Ni excess in the tested parameter space strengthen the assumption of off-stoichiometry and of absence of intrinsic antisite defects and overlithiation.

Magnetic properties of $LiNiO_2$.—The procedure of determining the Ni occupancy on the Li site by Rietveld refinement is model-dependent and thus a cross-validation with other methods is highly desirable. An often overlooked property of the materials that correlates with its crystallographic properties is the magnetic behavior. Even before its application as cathode active material, the magnetic properties of the $Li_{1-z}Ni_{1+z}O_2$ system have been investigated by Goodenough et al.[45] The electronic configuration of Ni^{3+} in an octahedral coordination environment and the view along the *c*-axis on top of the Ni slab of the stoichiometric LNO crystal structure are depicted in Fig. 4a. With the orbital energetic levels being split into two e_g and three t_{2g} states and the Ni^{3+} electron configuration being $3d^7$, a doublet electronic configuration (S = ½) with a single unpaired electron is expected, which can interact with an external magnetic field. Even if LNO is reported as a "non-cooperative" or "dynamic" Jahn-Teller system, the material remains a S = ½ system.[71] Because the Ni ions sit on a triangular lattice for perfectly crystallized $LiNiO_2$, no long-range magnetic ordering is expected to form due to quantum mechanical frustration of the electron spins,[72] which motivated the investigation of near-stoichiometric LNO compounds.[73–75] Given the interest in LNO as CAM, several authors investigated the magnetic properties of $Li_{1-z}Ni_{1+z}O_2$ in narrow ranges of *z*.[34,36,76,77] All authors observed a transition from paramagnetic behavior at high temperature towards a state of magnetic long-range ordering below a certain temperature, coming with a rapid increase of the magnetic susceptibility. Due to the fact that magnetic ordering is correlated to the presence of excess Ni^{2+} in the Li layers, coupling different Ni layers, it was found that this transition shifted towards higher temperatures with increasing values of *z*. This makes the measurement of temperature-dependent magnetization a powerful tool to investigate site occupation and lattice defects in LNO.

Figure 4b shows the field dependent magnetization curves of one exemplary LNO sample measured at 2 K and 300 K. The inset shows a magnification of the magnetization in a range of −2 to 2 kOe. While paramagnetic behavior is observed at 300 K, a hysteretic feature is observed at 2 K, indicative of magnetic ordering. Although the exact mechanism of this magnetic ordering is still under debate in the literature, as mentioned above there is consensus that it is related to the excess Ni^{2+} on the Li site. Materials showing a transition between the paramagnetic regime and magnetic ordering can be described by the Curie-Weiss law shown in Eq. 2.

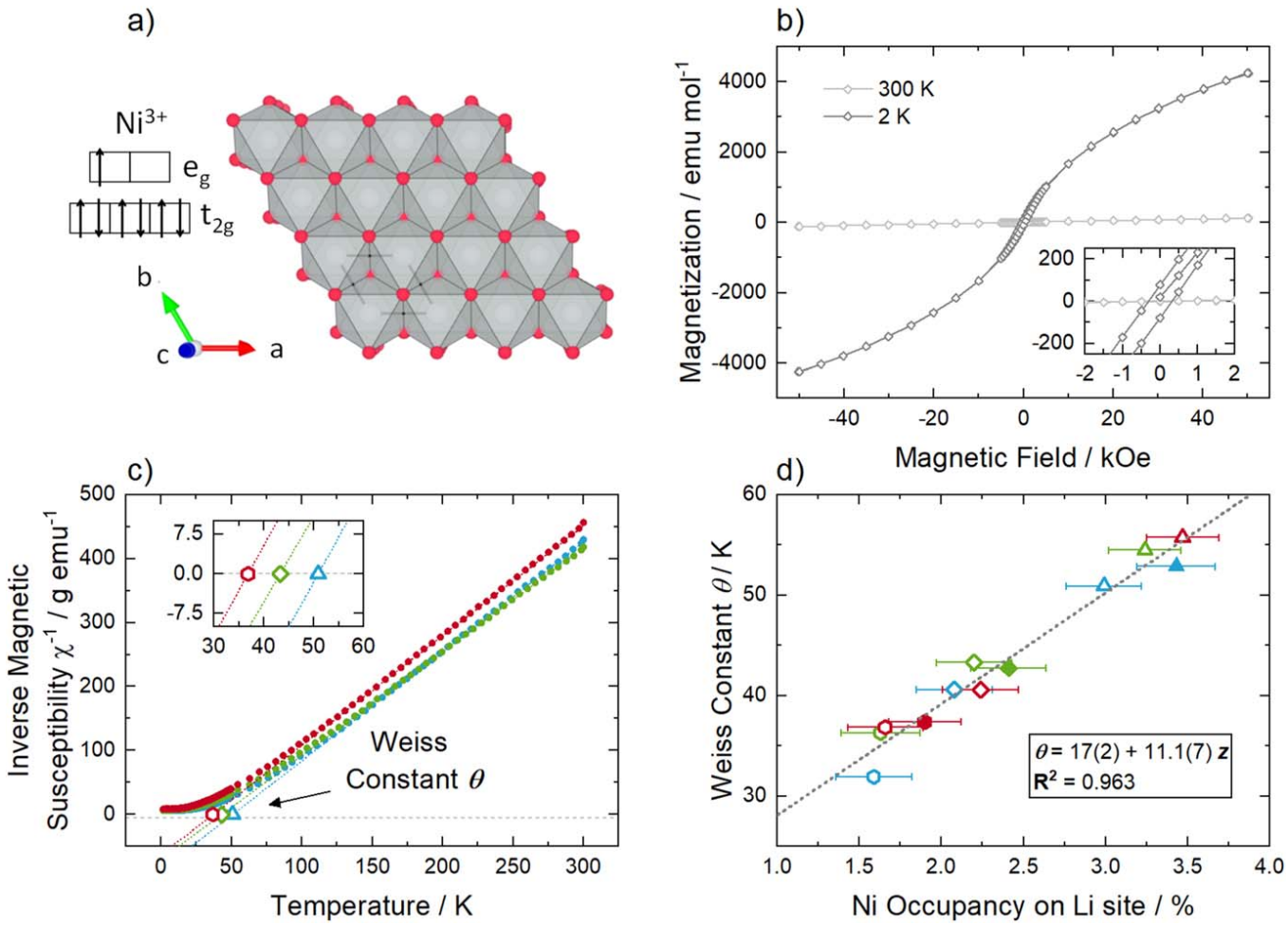

Figure 4. Magnetization results obtained from SQUID-measurements for selected samples. (a) Electronic configuration of $Ni^{3}{}_{+}$ in octahedral coordination and view along the *c*-axis on top of the Ni slab. (b) Magnetization curve of the LNO sample prepared from the 12 μm precursor with 1.01 Li equivalents per mol of Ni at a maximum calcination temperature of 700 °C. Two sets of measurements between −50 and 50 kOe were performed at 2 K (dark grey) and 300 K (light grey), respectively. The inset shows a magnified view of the magnetization at low external field values, highlighting the hysteretic behavior at the low measurement temperature. (c) Dependence of the inverse magnetic susceptibility on the measurement temperature at an external field of 10 kOe for three LNO samples prepared from the 12 μm precursor (blue: 680 °C Li equiv., green: 700 °C 1.01 Li equiv., red: 720 °C 1.04 Li equiv.). The Weiss constant θ was determined by performing a linear regression between 150 and 300 K and interpolating on the *x*-axis. (d) Correlation of the determined Weiss constant θ with the Ni occupancy on the Li site. The grey dotted line represents a linear regression through all data points.

Table II. Results from magnetization measurements for all samples calcined from the 12 μm $Ni(OH)_2$ precursor and for three exemplary samples calcined from the 4 μm $Ni(OH)_2$ precursor: weiss constant θ and Curie constant C.

Sample	θ/K	C/m^3 K mol^{-1}
	12 μm	
0.98 680 °C	50.90	0.59
0.98 700 °C	54.50	0.59
0.98 720 °C	55.73	0.58
1.01 680 °C	40.59	0.56
1.01 700 °C	43.29	0.62
1.01 720 °C	40.60	0.62
1.04 680 °C	29.93	0.62
1.04 700 °C	36.30	0.59
1.04 720 °C	36.85	0.58
	4 μm	
0.98 680 °C	53.00	0.58
1.01 700 °C	42.91	0.59
1.04 720 °C	37.60	0.57

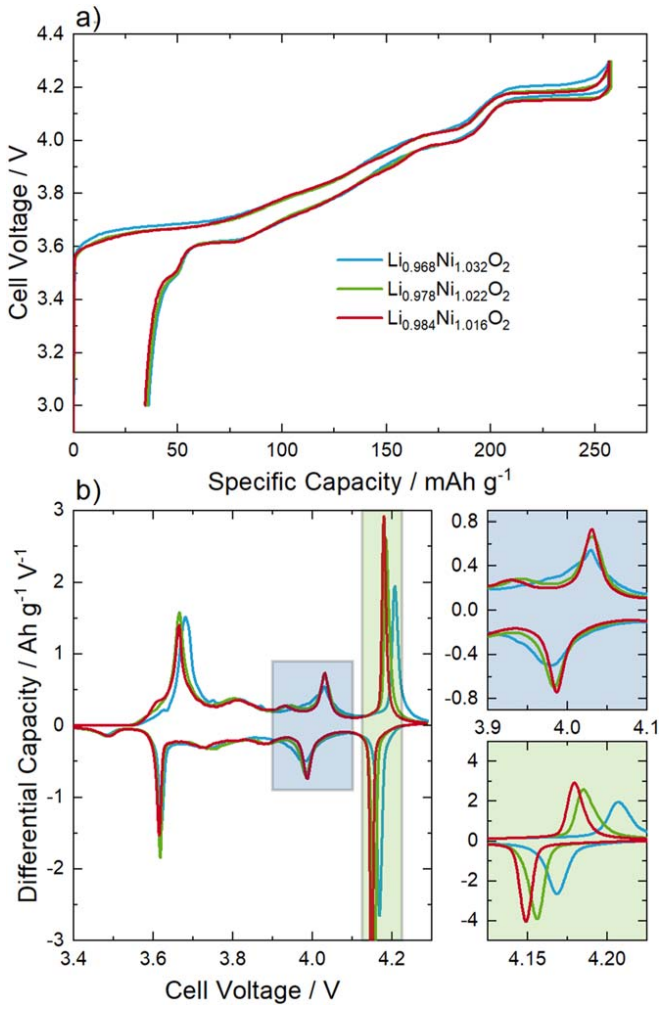

Figure 5. Voltage profile analysis of LNO samples with distinctly different values of z in $Li_{1-z}Ni_{1+z}O_2$. The samples correspond to the materials prepared from the 12 μm precursor at the same maximum calcination temperature of 700 °C and varying number of Li equivalents per mol of Ni. (a) Cell voltage vs specific capacity of the 1st cycle for z = 0.032(2) (blue), z = 0.022(2) (green) and z = 0.016(2) (red) with the stoichiometry determined by Rietveld refinement. b) Differential capacity vs cell voltage. Two magnifications of the data in the range of 3.9–4.1 V and 4.125–4.225 V are shown. The cells were cycled at C/10.

$$\chi = \frac{C}{T - \theta} \quad [2]$$

Here χ denotes the magnetic susceptibility, C is the Curie constant, T is the measurement temperature and θ is the Weiss constant, which is the transition temperature between paramagnetic and hysteretic magnetic behavior. The Weiss constant can be determined by a linear regression of the inverse magnetic susceptibility in the paramagnetic regime (150−300 K) and extrapolating to the temperature axis. The inverse magnetic susceptibility χ^{-1} as a function of temperature and the regression are depicted in Fig. 4c for three exemplary LNO samples prepared from the 12 μm $Ni(OH)_2$ (blue: 680 °C, 0.98 li equiv.; green: 700 °C, 1.01 li equiv.; red: 720 °C, 1.04 li equiv., analogous to Fig. 2). The results for θ for all materials from this study are well correlated to the Ni occupancy on the Li site determined by Rietveld refinement, as shown in Fig. 4d (all measured values of θ are depicted in Table II). The linear dependency indeed indicates a clear correlation between Ni excess and magnetic behavior of the LNO samples and is in good agreement with the results of the above-cited groups, even for very small values of z.[76,77] Although this finding corroborates the trend of Ni excess in its qualitative nature, it alone is not a confirmation of the assumed model and the absence of antisite defects. Another information that can be derived from the fit of χ^{-1} is the Curie constant C. For a given material with n unpaired electrons that behaves like a paramagnet, the expected Curie constant in the spin-only case (no spin–orbit coupling) follows Eq. 3.

$$\chi T = C = \frac{1}{8}(n(n + 2)) \quad [3]$$

Hence, a Curie constant of 0.375 (unit: m^3 K mol^{-1}) is expected for stoichiometric $LiNiO_2$. In the applied model for Rietveld refinement, an increase in the off-stoichiometry z comes with the generation of $2z$ Ni^{2+} ions and thus additional unpaired electrons. An increase of z by 0.01 in theory would equal an increase of C by 0.05. However, the determined Curie constants for the different samples, as shown in Table II, range from 0.56 to 0.62 (with a large scatter, but the appearance of decreasing C with increasing z) and clearly deviate from the single unpaired electron picture. Nevertheless, the results are in line with other reports.[34,77] Possible explanations for this deviation might lie in the enhancement of Landé g factor caused by a local Jahn-Teller effect, as for $NaNiO_2$, or orbital contributions.[78,79]

These results confirm that magnetization measurements using a SQUID are a valuable tool for the characterization of battery active materials, even for samples with only minor differences in crystal structure. With magnetization measurements becoming feasible in situ inside an assembled cell, where changes of magnetic properties during electrochemical (de-)lithiation can be monitored, these investigations are expected to attract more interest of CAM researchers in the future.[80,81]

Impact of structural chemistry on the voltage profile.—After determining the crystal structure, crystallite size and magnetic properties of the calcined samples, their electrochemical behavior was investigated by employing galvanostatic cycling and analysis of the differential capacity (dQ/dV) plots.

The measured voltage of a given electrochemical reaction is the sum of the thermodynamic voltage of the reaction and the overpotentials corresponding to the cell impedance. For a LNO half-cell, the occurring reaction during oxidation is shown in Eq. 4.

$$Li_xNi_{1+z}O_2 \rightleftharpoons Li_{x-\delta}Ni_{1+z}O_2 + \delta\, e^- + \delta\, Li^+ \quad [4]$$

In this case x is in the range between 0 and $1-z$ in case of full delithiation and lithiation, respectively, and δ denotes the number of transferred electrons. The thermodynamic (open cell) voltage E is intrinsically linked to the Gibbs free energy Δ_rG of the underlying

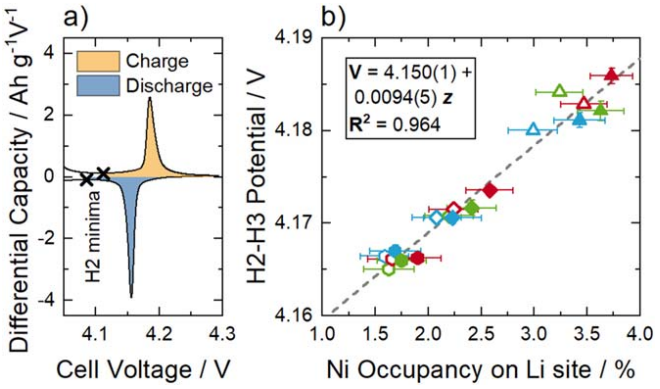

Figure 6. Correlation of the mean potential of the H2–H3 phase transition with the Ni occupancy on the Li site. (a) The potential of the phase transition was determined by taking the mean potential between the minimum of the dQ/dV curve before the H2–H3 peak onset and 4.3 V for charge and discharge. (b) Mean potential of the H2–H3 phase transition as a function of the Ni occupancy on the Li site determined by Rietveld refinement for all samples of this study. The y-error bars depict the standard deviation over at least three cells (only small deviations are obtained). The grey dashed line depicts a linear regression through all data points.

reaction and is depicted for the case of oxidation of LNO during charge in Eq. 5 as:

$$E = -\frac{\Delta_r G}{nF} = -\frac{G_{\mathrm{Li}_x\mathrm{Ni}_{1+z}\mathrm{O}_2} - \delta G_{\mathrm{Li}} - G_{\mathrm{Li}_{x-\delta}\mathrm{Ni}_{1+z}\mathrm{O}_2}}{\delta F} \quad [5]$$

Here, $n = \delta$ is the number of transferred electrons and F is the Faraday constant. With a change in LNO stoichiometry described by the value of z, the underlying reaction changes and might impact the state of charge-dependent thermodynamic voltage, that can easily be probed by a simple electrochemical measurement when a correction for the overpotential is considered. Figure 5a shows the voltage profiles of three exemplary LNO samples from this study prepared from the 12 μm $Ni(OH)_2$ precursor with distinct values of Ni excess that were determined by Rietveld refinement (blue: $z = 0.032(2)$, green: $z = 0.022(2)$ and red: $z = 0.016(2)$). At first sight, all voltage profiles look very similar, again highlighting the proper crystallization of all samples as indicated by the PXRD results. However, small changes in the voltage profiles can be made visible by calculating the *dQ/dV* curves, which are shown in Fig. 5b. For LNO, distinct voltage plateaus (peaks in the *dQ/dV* curve) are observed, which are the result of several phase transitions of the material during (de−)lithiation. These individual phases can be distinguished in ex situ as well as in situ PXRD measurements, as confirmed by the work of several groups.[31,40,82–88] In the general consensus, there are three phase transitions identifed by PXRD during continuous delithiation, separating four single-phase domains occurring in the following order: H1 ($1 > x > 0.75$) to M ($0.63 > x > 0.4$) to H2 ($0.33 > x > 0.25$) to H3 ($0.12 > x > 0$). The phases are named by their symmetry (H: hexagonal, M: monoclinic) and their order of appearance during delithiation. Due to the Gibbs' phase rule, the two-phase regions correspond to voltage plateaus as observed in Fig. 5a, while single-phase regions show relatively steep voltage changes. The single-phase regions are easier to spot in the *dQ/dV* representation, where they occur as local minima. However, it is important to note that only four phases have ever been observed by PXRD, while seven minima are identified on the *dQ/dV* curve. They coincide with certain values of x (1, 3/4, 5/8, 1/2, 2/5, 1/4, 1/8). This is well in line with recent first-principles calculations, where all those degrees of lithiation are predicted to form ordered Li arrangements that are energetically favorable.[88] Yet some of these states are only stable at 0 K, while at higher temperatures they are destabilized by entropic contributions. As a consequence, for example, only one monoclinic region is observed structurally by PXRD, instead of a sequence of stable phases $x = 5/8$, 1/2, 2/5. Nonetheless, the thermodynamic signature of these phases is visible in the *dQ/dV* curve, and it is possible that they are still stabilized at the local scale, which would be hard to detect by means of PXRD and electron diffraction would be needed to observe them.[89]

The differential capacity peaks associated with the discussed phase transitions can be found for all samples with different values of z. Nevertheless, with a change of z in $Li_{1-z}Ni_{1+z}O_2$, some differences are observed in two distinct voltage ranges, which are highlighted in the magnified segments of Fig. 5b. In the voltage range between 3.9–4.1 V (marked by the blue shaded area and the blue shaded inset), materials with a small Ni excess show two distinct peaks with a clear local minimum (red and green lines in Fig. 5b). This minimum corresponds to a stable phase that was predicted by first-principles calculations ($Li_{0.4}NiO_2$, $x = 2/5$).[88,90] With an increasing amount of Ni in the Li layer, this minimum vanishes as observed for the sample with $z = 0.032$ (blue line in Fig. 5b). This indicates that the presence of a critical Ni excess is disrupting the arrangement of the Li ions and vacancies, thus making the formation of that phase energetically less favorable. However, the most pronounced change in the voltage profile is observed in the range between 4.125–4.225 V, marked by the green shaded area/inset, i.e. where the H2 to H3 phase transition occurs. Here, for increasing values of z, a shift of the phase transition (peak position in the *dQ/dV*) to higher potentials is clearly observed. The fact that this happens both during charge and discharge excludes overpotentials to be causing this effect and thus indicates that a change of the thermodynamics related to the phase transition must occur. Besides the peak position changes, also a widening of the peak width is seen in the *dQ/dV* plots with increasing z, which is often discussed to be related to a suppression of the phase transition, i.e. to the progressive narrowing of the H2–H3 miscibility gap.[16,91,92]

A clear assignment of the z values to a peak voltage is difficult, which is why we tried to define clear and stringent rules for calculating the mean potential of the phase transition. By assuming that minima in the *dQ/dV* curve correspond to single-phase regions, the minimum in the *dQ/dV* curve between 4.0 V and 4.16 V was determined (related to the H2 phase), which is depicted in Fig. 6a. Individually for charge and discharge, the mean potential of the *dQ/dV* peak between the H2 minimum and the upper cut-off voltage of 4.3 V was calculated. Then, the mean was taken again between the charge and discharge value to cancel out the overpotential and obtain the thermodynamically defined potential. Our correction of the overpotential assumes that it is symmetric for both oxidation and reduction processes. We have observed that indeed this assumption is verified in our case, as the cells were cycled at low currents (20 mA g^{-1}). Asymmetries may be expected only at higher C rates.[93] The results for all samples from this study are shown in Fig. 6b as a function of the Ni occupancy on the Li site determined by Rietveld refinement. This comparison shows a clear linear correlation between these values, with an increase of the potential of the phase transition of ~ 9 mV per increase of 1% Ni excess. This observation confirms a correlation between the exact LNO stoichiometry and the hereby determined thermodynamic potentials of the LNO phases.

Equation 5 can be used to understand this behavior and can be rewritten to reflect the H2–H3 phase transition voltage change as a function of z, i.e. ΔE_z, as shown in Eq. 6.

$$\Delta E_z = -\left(\frac{G_{\mathrm{H2},z} - G_{\mathrm{H3},z} + (x_{\mathrm{H2},z} - x_{\mathrm{H3},z})G_{\mathrm{Li}}}{(x_{\mathrm{H2},z} - x_{\mathrm{H3},z})F} - \frac{G_{\mathrm{H2,LNO}} - G_{\mathrm{H3,LNO}} + (x_{\mathrm{H2,LNO}} - x_{\mathrm{H3,LNO}})G_{\mathrm{Li}}}{(x_{\mathrm{H2,LNO}} - x_{\mathrm{H3,LNO}})F}\right) \quad [6]$$

Here, $G_{\mathrm{H2},z}$ and $G_{\mathrm{H3},z}$ represent the Gibbs free energy of the H2 and H3 phases of a off-stoichiometric LNO, respectively, while $G_{\mathrm{H2,LNO}}$

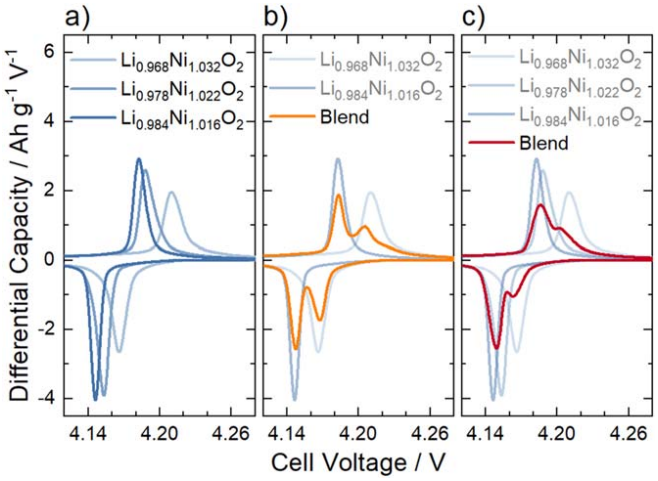

Figure 7. 1st cycle differential capacity of the H2–H3 phase transition of LNO electrodes consisting of different blends of off-stoichiometric LNO samples. (a) Differential capacity of pure materials already discussed in Fig. 5. (b) Differential capacity of a 50/50 blend of two LNOs that differ significantly with regards to their off-stoichiometry. The blended electrode is depicted in orange, with the curves of the pure materials being shown as transparent overlays. (c) 33/33/33 blend of all three materials.

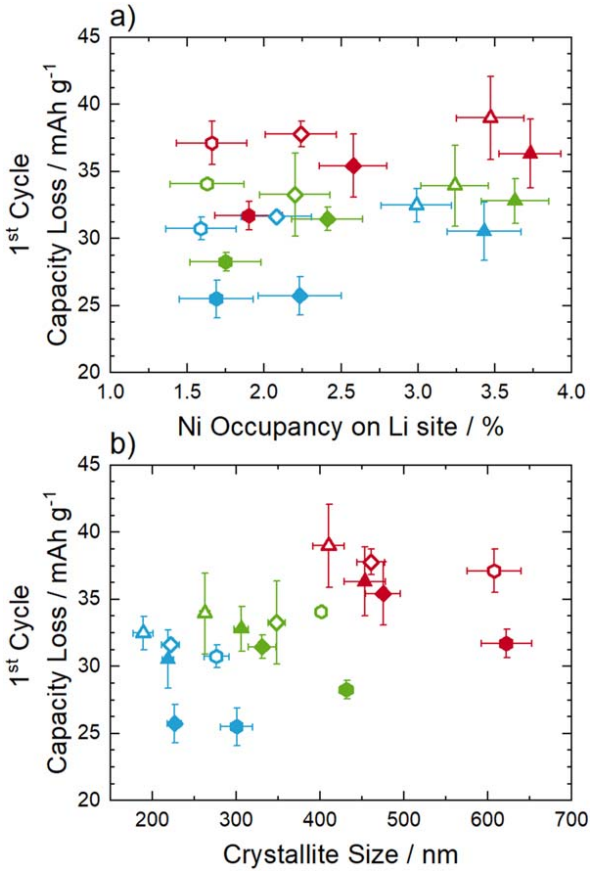

Figure 8. 1st cycle capacity loss vs (a) Ni occupancy on the Li site and (b) crystallite size from Rietveld refinement. In (a) no correlation can be observed. In (b) a weak correlation is present. The cells were cycled at C/10 at a temperature of 25 °C.

and $G_{H3,LNO}$ represent the Gibbs free energy of the H2 and H3 phases of a hypothetical perfectly stoichiometric LNO, respectively. The different x values represent the compositions at which the H2 and H3 phases occur. Experimentally, Fig. 5a demonstrated that for small values of z, the compositional span of the H2 to H3 transition is not significantly narrowed with increasing z ($x_{H2,z}$—$x_{H3,z} \approx x_{H2,LNO}$—$x_{H3,LNO} \triangleq x_{H2}$—$x_{H3}$). Likewise, the voltage at which the H2 single phase occurs does not appear to be affected for small values of z as the relative minimum in the dQ/dV plot in Fig. 5b does not shift, which means that $G_{H2,z}$—$G_{H2,LNO} \approx 0$. This ultimately leads to an approximation of ΔE_z depicted in Eq. 7:

$$\Delta E_z = -\left(\frac{G_{H3,LNO} - G_{H3,z}}{(x_{H2} - x_{H3})F}\right) \quad [7]$$

In light of Eq. 7, an increased voltage of the H2–H3 phase transition indicates a larger energetic difference between the Gibbs free energy of the H2 and H3 phases. In other words, as z increases, the H3 phase becomes thermodynamically destabilized compared to the others, and to H2 in particular. We speculate this is due to the H3 phases having a significantly smaller c unit cell parameter and hence Li interlayer thickness, where accomodating a Ni cation can be less favourable.

The hereby reported clear correlation between z and the average H2–H3 transition potential allows to draw conclusions about the stoichiometry of the samples by a rather simple quantitative analysis of the voltage profiles. This can be an extremely valuable tool to complement the stoichiometry obtained by PXRD refinement.

As mentioned above, the dQ/dV plot does not only reveal an increase of the average transition potential with increasing off-stoichiometry, but also a broadening of the H2–H3 peak related to a larger average slope of the voltage curve. A broadening of the peak in the dQ/dV curve is often associated with a narrower miscibility gap, namely the phase transition is progressively evolving towards the formation of a solid solution. This implies that crystallographic stresses are reduced by avoiding the sudden anisotropic volume changes of the H2 to H3 phase transition. This peak shape is known for mid-Ni NCM materials, where the anisotropic volume changes are less pronounced.[11] However, here we show that care must be taken in interpreting dQ/dV peak broadening behavior, as the broadening can also be mimicked by the formation of sample inhomogeneities, where severe phase transitions inside the individual particles still occur, but the overlapping H2 to H3 transition peaks merge to yield broad features in the dQ/dV plots. This phenomenon is demonstrated in Fig. 7. In Fig. 7a the dQ/dV curves of three individual LNO samples are shown, which have already been depicted in Fig. 5. In Fig. 7b, the dQ/dV curve of a 50/50 weight ratio mixture of the samples with $z = 0.016(2)$ and $z = 0.032(2)$ is depicted (the individual dQ/dV profiles are again shown in transparent colors). Figure 7c analogously shows the dQ/dV features for the 33/33/33 weight ratio mixture of all three samples (additionally including the sample with $z = 0.022(2)$).

Blending different CAMs leads to a superposition of the voltage profiles according to their relative weight contents.[94] Only a slight shift of the overpotentials is observed due to an inhomogeneous current load at different SOCs.[95] Already in the measurement with a blend of three samples, the peak broadening due to different stoichiometries can be observed and the individual peaks cannot be perfectly resolved any more. This indicates that samples with more material inhomogeneities will show only one peak with a large width. In large-scale production, one can easily imagine that due to difficulties of keeping constant calcination parameters (temperature, atmosphere, mixing of individual components) severe powder inhomogeneities can occur.[96] In this case, the peak width can be used as a measure for the powder inhomogeneity. However, in studies where a suppression of the detrimental phase transition is targeted by modification of the materials (e.g. doping and coating), the possibility of powder inhomogeneities causing the peak broadening is often overlooked. Thus, additional information on the structural properties going beyond the electrochemical testing is always needed to deconvolute the two effects.

Correlation with 1st cycle capacity loss.—Since the early investigations of LNO as cathode active material, researchers have

sought to draw a connection between the Ni excess in the Li layer and the poor 1st cycle reversibility.[31,32,57] Some authors tried to find empirical correlations between those values, but looked at very large variations of z (0.01–0.12).[36] Even for samples in which Ni was substituted for other elements, the decrease of the 1st cycle coulombic efficiency is linked to the increase of excess Ni in the Li layer.[97] An early explanation for this phenomenon in case of LNO was found in the oxidation of the intralayer Ni^{2+} to Ni^{3+}, leading to a local contraction of the crystal lattice and hence poor Li mobility.[32]

The large 1st cycle capacity loss is not only an inherent property for LNO, but is also found for most NCMs, making the narrowing of this gap a key target to maximize energy density.[24] The origin of the poor reversibility was shown to be of kinetic origin by a multitude of studies and can for example be reduced by the application of a CV step at the end of discharge[25] or an increase of cycling temperature.[26] Experiments looking at the apparent diffusion coefficients[98] or Li mobility by NMR experiments[99] further underline this problem. While a negative effect of excess Ni on the Li mobility is certain, we used our calcined samples to further investigate correlations between small variations of z and the 1st cycle capacity loss.

As the Ni excess has been carefully quantified in this study for a large set of samples and as the observed trends were confirmed by several independent techniques, this alleged correlation can be probed. The 1st cycle capacity loss as a function of the Ni excess determined by PXRD refinement is depicted in Fig. 8a. In contrast to the aforementioned belief, *no correlation* between these quantities is observed. **S**amples with similar values of z show substantial differences in 1st cycle capacity loss up to 10 mAh g^{-1}. Furthermore, only a slight systematic difference between the CAMs based on the 4 μm and 12 μm precursors is observed, indicating a low impact of secondary particle morphology onto the electrochemical performance. In view of the narrow parameter space of this study and the precise data, another underlying physical parameter must therefore cause the observed differences.

Besides the broadly discussed crystallographic properties and the difference in secondary particle structure, the influence of the primary particle structure should thus be considered. The correlation of the average crystallite size from Rietveld refinement (Figs. 3c and 3d) with the 1st cycle capacity loss is shown in Fig. 8b. Although an increase of the 1st cycle capacity loss with crystallite size is apparent, the rather weak correlation still allows for different interpretations. However, it again must be emphasized that the crystallite size only reflects an average over the whole sample powder, whereas in reality a distribution of primary particle sizes is present. A mere interpretation of size effects by PXRD refinement is therefore not sufficient. Even more importantly, the link between primary particles size and the accessible particles surfaces, *which evolve upon cycling*, must be addressed. A detailed study of the primary particle morphology and its impact on electrochemistry therefore will be part of an upcoming study.

Conclusions

Through the comparison of three methods with fundamentally different physical principles (X-ray diffraction, magnetism, electrochemical analysis), the validity of the generally applied structural model of LNO—the "off-stoichiometry model"—could be further reinforced. Within an industrially relevant parameter space for synthesis of polycrystalline LNO materials, the values of z in $Li_{1-z}Ni_{1+z}O_2$ were found to mainly depend on the Li excess applied in the calcination, whereas the calcination temperature mainly affected the average crystallite size. Besides PXRD being still the most robust technique for the determination of the crystallographic properties, the values of z are also correlated with magnetic properties, i.e. the Weiss constant, and with the half-cell potential of the H2–H3 phase transition, enabling an estimation of the stoichiometry by electrochemical measurements. However, it is pointed out that the absence of a sharp dQ/dV peak related to that phase transition does not necessarily indicate the suppression of the phase transition, but can also be the result of sample inhomogeneity. Although being widely discussed in the literature, *no clear correlation* of a small Ni excess in the Li slab and the 1st cycle capacity loss was found for samples within an industrially reasonable physical parameter space.

Thus, we propose a correlation between the 1st cycle capacity loss and the different primary particle morphologies, as a (weak) correlation between 1st cycle reversibility and average crystallite size is present. Particle morphology has a direct impact on the surface area between cathode active material and electrolyte and is a key parameter to look at to understand the Li intercalation kinetics. However, a quantification of primary particle morphology is not a trivial task, as measuring a single value (average crystallite size) by PXRD is not sufficient and rather a distribution of particle sizes is needed. Moreover, the morphology will change during cyling due to fracturing of the secondary particle agglomerates, further complicating the task. Therefore, to further conclude the impact on the electrochemical performance, a detailed study on the primary particle morphology and its evolution upon cycling was performed and will be presented in a forthcoming publication.

Acknowledgments

The magnetization measurements were conducted at the Chair of Inorganic Chemistry with Focus on Novel Materials (Prof. Thomas Fässler) at the Technical University of Munich. François Fauth and the BL04-MSPD beamline team at the ALBA synchrotron are gratefully acknowledged for their support to the PXRD measurements.

ORCID

Philipp Kurzhals https://orcid.org/0000-0002-7013-080X
Felix Riewald https://orcid.org/0000-0001-9002-3633
Matteo Bianchini https://orcid.org/0000-0003-4034-7706
Hubert A. Gasteiger https://orcid.org/0000-0001-8199-8703
Jürgen Janek https://orcid.org/0000-0002-9221-4756

References

1. A. Masias, J. Marcicki, and W. A. Paxton, *ACS Energy Lett.*, **6**, 621 (2021).
2. Y. Ding, Z. P. Cano, A. Yu, J. Lu, and Z. Chen, *Electrochemical Energy Reviews*, **2**, 1 (2019).
3. C. Xu, Q. Dai, L. Gaines, M. Hu, A. Tukker, and B. Steubing, *Communications Materials*, **1**, 99 (2020).
4. W. Li, E. M. Erickson, and A. Manthiram, *Nat. Energy*, **5**, 26 (2020).
5. L. Croguennec and M. R. Palacin, *JACS*, **137**, 3140 (2015).
6. S.-T. Myung, F. Maglia, K.-J. Park, C. S. Yoon, P. Lamp, S.-J. Kim, and Y.-K. Sun, *ACS Energy Lett.*, **2**, 196 (2017).
7. D. Karabelli, S. Kiemel, S. Singh, J. Koller, S. Ehrenberger, R. Miehe, M. Weeber, and K. P. Birke, *frontiers in Energy Research*, **8**, 1 (2021).
8. J.-H. Kim, H.-H. Ryu, S. J. Kim, C. S. Yoon, and Y.-K. Sun, *ACS Appl. Mater. Interfaces*, **11**, 30936 (2019).
9. H.-J. Noh, S. Youn, C. S. Yoon, and Y.-K. Sun, *J. Power Sources*, **233**, 121 (2013).
10. A. O. Kondrakov, H. Geßwein, K. Galdina, L. De Biasi, V. Meded, E. O. Filatova, G. Schumacher, W. Wenzel, P. Hartmann, and T. Brezesinski, *The Journal of Physical Chemistry C*, **121**, 24381 (2017).
11. A. O. Kondrakov, A. Schmidt, J. Xu, H. Geßwein, R. Mönig, P. Hartmann, H. Sommer, T. Brezesinski, and J. R. Janek, *The Journal of Physical Chemistry C*, **121**, 3286 (2017).
12. L. de Biasi, A. Schiele, M. Roca-Ayats, G. Garcia, T. Brezesinski, P. Hartmann, and J. Janek, *ChemSusChem*, **12**, 2240 (2019).
13. R. Jung, M. Metzger, F. Maglia, C. Stinner, and H. A. Gasteiger, *J. Electrochem. Soc.*, **164**, A1361 (2017).
14. W. Yan, S. Yang, Y. Huang, Y. Yang, and Y. Guohui, *J. Alloys Compd.*, **819**, 153048 (2020).
15. L. Mu, W. H. Kan, C. Kuai, Z. Yang, L. Li, C.-J. Sun, S. Sainio, M. Avdeev, D. Nordlund, and F. Lin, *ACS Appl. Mater. Interfaces*, **12**, 12874 (2020).
16. L. Mu et al., *Chem. Mater.*, **31**, 9769 (2019).
17. K. Min, K. Park, S. Y. Park, S.-W. Seo, B. Choi, and E. Cho, *J. Electrochem. Soc.*, **165**, A79 (2018).
18. J.-M. Kim, X. Zhang, J.-G. Zhang, A. Manthiram, Y. S. Meng, and W. Xu, *Mater. Today*, **46**, 155 (2021).
19. J. Langdon and A. Manthiram, *Energy Storage Mater.*, **37**, 143 (2021).
20. J.-Y. Hwang, S.-M. Oh, S.-T. Myung, K. Y. Chung, I. Belharouak, and Y.-K. Sun, *Nat. Commun.*, **6**, 6865 (2015).
21. U. H. Kim, H. H. Ryu, J. H. Kim, R. Mücke, P. Kaghazchi, C. S. Yoon, and Y. K. Sun, *Adv. Energy Mater.*, **9**, 1803902 (2019).

22. H. H. Sun, H.-H. Ryu, U.-H. Kim, J. A. Weeks, A. Heller, Y.-K. Sun, and C. B. Mullins, *ACS Energy Lett.*, **5**, 1136 (2020).
23. S.-H. Kang, W.-S. Yoon, K.-W. Nam, X.-Q. Yang, and D. P. Abraham, *J. Mater. Sci.*, **43**, 4701 (2008).
24. M. D. Radin, S. Hy, M. Sina, C. Fang, H. Liu, J. Vinckeviciute, M. Zhang, M. S. Whittingham, Y. S. Meng, and A. Van der Ven, *Adv. Energy Mater.*, **7**, 1602888 (2017).
25. J. Kasnatscheew, M. Evertz, B. Streipert, R. Wagner, R. Klöpsch, B. Vortmann, H. Hahn, S. Nowak, M. Amereller, and A.-C. Gentschev, *Phys. Chem. Chem. Phys.*, **18**, 3956 (2016).
26. H. Zhou, F. Xin, B. Pei, and M. S. Whittingham, *ACS Energy Lett.*, **4**, 1902 (2019).
27. R. Kanno, H. Kubo, Y. Kawamoto, T. Kamiyama, F. Izumi, Y. Takeda, and M. Takano, *J. Solid State Chem.*, **110**, 216 (1994).
28. W. Li, J. Reimers, and J. Dahn, *Physical Review B*, **46**, 3236 (1992).
29. A. Hirano, R. Kanno, Y. Kawamoto, Y. Takeda, K. Yamaura, M. Takano, K. Ohyama, M. Ohashi, and Y. Yamaguchi, *Solid State Ionics*, **78**, 123 (1995).
30. M. Bianchini, M. Roca-Ayats, P. Hartmann, T. Brezesinski, and J. Janek, *Angew. Chem. Int. Ed.*, **58**, 10434 (2019).
31. H. Arai, S. Okada, H. Ohtsuka, M. Ichimura, and J. Yamaki, *Solid State Ionics*, **80**, 261 (1995).
32. C. Delmas, J. P. Pérès, A. Rougier, A. Demourgues, F. Weill, A. Chadwick, M. Broussely, F. Perton, P. Biensan, and P. Willmann, *J. Power Sources*, **68**, 120 (1997).
33. V. Bianchi, S. Bach, C. Belhomme, J. Farcy, J. P. Pereira-Ramos, D. Caurant, N. Baffier, and P. Willmann, *Electrochim. Acta*, **46**, 999 (2001).
34. A. Rougier, P. Gravereau, and C. Delmas, *J. Electrochem. Soc.*, **143**, 1168 (1996).
35. R. V. Moshtev, P. Zlatilova, V. Manev, and A. Sato, *J. Power Sources*, **54**, 329 (1995).
36. V. Bianchi, D. Caurant, N. Baffier, C. Belhomme, E. Chappel, G. Chouteau, S. Bach, J. P. Pereira-Ramos, A. Sulpice, and P. Wilmann, *Solid State Ionics*, **140**, 1 (2001).
37. F. Fauth, I. Peral, C. Popescu, and M. Knapp, *Powder Diffr.*, **28**, S360 (2013).
38. J. Rodríguez-Carvajal, *Physica B*, **192**, 55 (1993).
39. T. Roisnel and J. Rodríquez-Carvajal, *Mater. Sci. Forum*, **378–381**, 118 (2001).
40. T. Ohzuku, A. Ueda, and M. Nagayama, *J. Electrochem. Soc.*, **140**, 1862 (1993).
41. J. Rodríguez-Carvajal, *Study of Micro-Structural Effects by Powder Diffraction Using the Program FULLPROF*, Laboratoire Léon Brillouin (CEA-CNRS) (2003), https://cdifx.univ-rennes1.fr/fps/Microstructural_effects.pdf.
42. L. Yin, G. S. Mattei, Z. Li, J. Zheng, W. Zhao, F. Omenya, C. Fang, W. Li, J. Li, and Q. Xie, *Rev. Sci. Instrum.*, **89**, 093002 (2018).
43. G. A. Bain and J. F. Berry, *J. Chem. Educ.*, **85**, 532 (2008).
44. L. D. Dyer, B. S. Borie Jr, and G. P. Smith, *JACS*, **76**, 1499 (1954).
45. J. B. Goodenough, D. G. Wickham, and W. J. Croft, *J. Phys. Chem. Solids*, **5**, 107 (1958).
46. R. D. Shannon, *Acta crystallographica Section A: Crystal Physics, Diffraction, Theoretical and General Crystallography*, **32**, 751 (1976).
47. M. Bianchini, F. Fauth, P. Hartmann, T. Brezesinski, and J. Janek, *J. Mater. Chem. A*, **8**, 1808 (2020).
48. M. Bianchini et al., *Chem. Mater.*, **32**, 9211 (2020).
49. H. S. Liu, Z. R. Zhang, Z. L. Gong, and Y. Yang, *Electrochem. Solid-State Lett.*, **7**, A190 (2004).
50. D.-H. Cho, C.-H. Jo, W. Cho, Y.-J. Kim, H. Yashiro, Y.-K. Sun, and S.-T. Myung, *J. Electrochem. Soc.*, **161**, A920 (2014).
51. D. Pritzl, T. Teufl, A. T. S. Freiberg, B. Strehle, J. Sicklinger, H. Sommer, P. Hartmann, and H. A. Gasteiger, *J. Electrochem. Soc.*, **166**, A4056 (2019).
52. Y. Kim, H. Park, J. H. Warner, and A. Manthiram, *ACS Energy Lett.*, **6**, 941 (2021).
53. S. Ahmed et al., *ACS Nano*, **13**, 10694 (2019).
54. E. McCalla, G. H. Carey, and J. R. Dahn, *Solid State Ionics*, **219**, 11 (2012).
55. T. Sata, *Ceram. Int.*, **24**, 53 (1998).
56. H. Beyer, S. Meini, N. Tsiouvaras, M. Piana, and H. Gasteiger, *Phys. Chem. Chem. Phys.*, **15**, 11025 (2013).
57. H. Arai, S. Okada, Y. Sakurai, and J.-i. Yamaki, *Solid State Ionics*, **95**, 275 (1997).
58. R. M. German, *Crit. Rev. Solid State Mater. Sci.*, **35**, 263 (2010).
59. J. Zheng, P. Yan, L. Estevez, C. Wang, and J.-G. Zhang, *Nano Energy*, **49**, 538 (2018).
60. H. Ronduda, M. Zybert, A. Szczęsna-Chrzan, T. Trzeciak, A. Ostrowski, D. Szymański, W. Wieczorek, W. Raróg-Pilecka, and M. Marcinek, *Nanomaterials*, **10**, 2018 (2020).
61. J. Zhu and G. Chen, *J. Mater. Chem. A*, **7**, 5463 (2019).
62. J. Li, H. Li, W. Stone, R. Weber, S. Hy, and J. R. Dahn, *J. Electrochem. Soc.*, **164**, A3529 (2017).
63. S.-Y. Lee, G.-S. Park, C. Jung, D.-S. Ko, S.-Y. Park, H. G. Kim, S.-H. Hong, Y. Zhu, and M. Kim, *Adv. Sci.*, **6**, 1800843 (2019).
64. S. Permien, T. Neumann, S. Indris, G. Neubüser, L. Kienle, A. Fiedler, A.-L. Hansen, D. Gianolio, T. Bredow, and W. Bensch, *Phys. Chem. Chem. Phys.*, **20**, 19129 (2018).
65. L. Vegard, *Z. Phys.*, **5**, 17 (1921).
66. L. Yin, Z. Li, G. S. Mattei, J. Zheng, W. Zhao, F. Omenya, C. Fang, W. Li, J. Li, and Q. Xie, *Chem. Mater.*, **32**, 1002 (2019).
67. C. Pouillerie, E. Suard, and C. Delmas, *J. Solid State Chem.*, **158**, 187 (2001).
68. A. Mesnier and A. Manthiram, *ACS Appl. Mater. Interfaces*, **12**, 52826 (2020).
69. W. Hu, H. Wang, W. Luo, B. Xu, and C. Ouyang, *Solid State Ionics*, **347**, 115257 (2020).
70. F. Kong, C. Liang, L. Wang, Y. Zheng, S. Perananthan, R. C. Longo, J. P. Ferraris, M. Kim, and K. Cho, *Adv. Energy Mater.*, **9**, 1802586 (2019).
71. A. Rougier, C. Delmas, and A. V. Chadwick, *Solid State Commun.*, **94**, 123 (1995).
72. P. W. Anderson, *Mater. Res. Bull.*, **8**, 153 (1973).
73. K. Hirakawa, H. Kadowaki, and K. Ubukoshi, *J. Phys. Soc. Jpn.*, **54**, 3526 (1985).
74. J. P. Kemp, P. A. Cox, and J. W. Hodby, *J. Phys. Condens. Matter*, **2**, 6699 (1990).
75. K. Hirota, Y. Nakazawa, and M. Ishikawa, *J. Phys. Condens. Matter*, **3**, 4721 (1991).
76. A. Rougier, C. Delmas, and G. Chouteau, *J. Phys. Chem. Solids*, **57**, 1101 (1996).
77. K. Yamaura, M. Takano, A. Hirano, and R. Kanno, *J. Solid State Chem.*, **127**, 109 (1996).
78. E. Chappel, M. D. Núñez-Regueiro, G. Chouteau, O. Isnard, and C. Darie, *The European Physical Journal B - Condensed Matter and Complex Systems*, **17**, 615 (2000).
79. M. D. Radin and A. Van der Ven, *Chem. Mater.*, **30**, 607 (2018).
80. G. Klinser, S. Topolovec, H. Krenn, and R. Würschum, *Encyclopedia of Interfacial Chemistry*, ed. K. Wandelt (Elsevier, Amsterdam: Oxford) 849 (2018).
81. Y. Hu, G. Z. Iwata, M. Mohammadi, E. V. Silletta, A. Wickenbrock, J. W. Blanchard, D. Budker, and A. Jerschow, *Proc. Natl Acad. Sci.*, **117**, 10667 (2020).
82. C. Delmas, M. Ménétrier, L. Croguennec, S. Levasseur, J. P. Pérès, C. Pouillerie, G. Prado, L. Fournès, and F. Weill, *Int. J. Inorg. Mater.*, **1**, 11 (1999).
83. W. Li, J. N. Reimers, and J. R. Dahn, *Solid State Ionics*, **67**, 123 (1993).
84. J. R. Dahn, U. von Sacken, and C. A. Michal, *Solid State Ionics*, **44**, 87 (1990).
85. E. Levi, M. D. Levi, G. Salitra, D. Aurbach, R. Oesten, U. Heider, and L. Heider, *Solid State Ionics*, **126**, 97 (1999).
86. X. Q. Yang, X. Sun, and J. McBreen, *Electrochem. Commun.*, **1**, 227 (1999).
87. H. Li, N. Zhang, J. Li, and J. Dahn, *J. Electrochem. Soc.*, **165**, A2985 (2018).
88. M. Mock, M. Bianchini, S. Sicolo, F. Fauth, and K. Albe, *J. Mater. Chem. A*, **9**, 14928 (2021).
89. J. P. Peres, F. Weill, and C. Delmas, *Solid State Ionics*, **116**, 19 (1999).
90. M. E. Arroyo y de Dompablo, A. Van der Ven, and G. Ceder, *Physical Review B*, **66**, 064112 (2002).
91. A. Aishova, G.-T. Park, C. S. Yoon, and Y.-K. Sun, *Adv. Energy Mater.*, **10**, 1903179 (2020).
92. H.-H. Ryu, G.-T. Park, C. S. Yoon, and Y.-K. Sun, *J. Mater. Chem. A*, **7**, 18580 (2019).
93. J. Park et al., *Nat. Mater.*, **20**, 991 (2021).
94. C. Heubner, T. Liebmann, M. Schneider, and A. Michaelis, *Electrochim. Acta*, **269**, 745 (2018).
95. T. Liebmann, C. Heubner, C. Lämmel, M. Schneider, and A. Michaelis, *ChemElectroChem*, **6**, 5728 (2019).
96. J. K. A. Park, S.-Y. Han, J. Paulsen, K.-T. Lee, and R. De Palma, *Precursor And Method For Preparing Ni Based Cathode Material For Rechargeable Lithium Ion Batteries*, WO/2018/158078 (2018).
97. L. Croguennec, E. Suard, P. Willmann, and C. Delmas, *Chem. Mater.*, **14**, 2149 (2002).
98. R. Ruess, S. Schweidler, H. Hemmelmann, G. Conforto, A. Bielefeld, D. A. Weber, J. Sann, M. T. Elm, and J. Janek, *J. Electrochem. Soc.*, **167**, 100532 (2020).
99. A. Grenier, P. J. Reeves, H. Liu, I. D. Seymour, K. Märker, K. M. Wiaderek, P. J. Chupas, C. P. Grey, and K. W. Chapman, *JACS*, **142**, 7001 (2020).

3.2 Publication 2:

The $LiNiO_2$ Cathode Active Material: A Comprehensive Study of Calcination Conditions and their Correlation with Physicochemical Properties. Part II. Morphology

The second publication of this thesis dealt with the morphology of the LNO samples prepared according to the procedure described in publication 1. The investigated materials consisted of secondary particle agglomerates, whose sizes were set by the applied $Ni(OH)_2$ precursors as determined by laser scattering. These agglomerates were built up from primary particles in the size range of several hundreds of nm.
Top view SEM imaging indicated the impact of changes in the calcination conditions on the primary particle growth. A quantitative evaluation of the primary particle size and the size distribution was performed by means of an automated segmentation of the SEM images. The results were used to calculate the primary particle specific surface areas of the LNO samples, representing the case of completely isolated primary particles, and these values were compared to physisorption measurements of the pristine powders. It was found that the specific surface areas of the untreated materials were close to the values estimated from the secondary particle sizes.
An impedance-based „capacitance method“ was used to *in situ* monitor the development of the specific surface area between CAM and electrolyte during cycling in coin half-cells. The measurements yielded that fracturing of the secondary particle agglomerates led to a significant increase of this surface area and that these changes were finalized after only a few cycles. The 1^{st} cycle capacity losses, which could not be explained by the different off-stoichiometries of the samples in publication 1, showed a clear correlation with the capacitance values after the first charge-discharge process. Further key electrochemical properties were shown to heavily depend on the primary particle specific surface area, underlining the importance of particle morphology for the use of LNO as CAM.

The publication was written by the author and F. Riewald and edited by the co-authors. The experiments were planned by the author, F. Riewald and H. Sommer. The SEM imaging, laser scattering and electrochemical testing were performed by the author and F. Riewald. The physisorption measurements were done by C. Ching and L. Hartmann from the Chair of Technical Electrochemistry at the Technical University of Munich. P. Holzmeister and S. Fritsch developed the image segmentation algorithm which was applied by the author and F. Riewald to evaluate the primary particle size distributions.

F. Riewald, P. Kurzhals, M. Bianchini, H. Sommer, H.A. Gasteiger, J. Janek, *A Com-*

prehensive Study of Calcination Conditions and their Correlation with Physicochemical Properties. Part II. Morphology, Journal of the Electrochemical Society **169**, 20529 (2022)

Journal of The Electrochemical Society, 2022 **169** 020529
1945-7111/2022/169(2)/020529/13/$40.00 © 2022 The Electrochemical Society ("ECS"). Published on behalf of ECS by IOP Publishing Limited

The $LiNiO_2$ Cathode Active Material: A Comprehensive Study of Calcination Conditions and their Correlation with Physicochemical Properties Part II. Morphology

Felix Riewald,[1,2,=,z] Philipp Kurzhals,[1,3,=] Matteo Bianchini,[1,4,*] Heino Sommer,[1] Jürgen Janek,[3,*] and Hubert A. Gasteiger[2,]**

[1]*BASF SE, New Battery Materials and Systems, D-67056 Ludwigshafen, Germany*
[2]*Chair of Technical Electrochemistry, Department of Chemistry and Catalysis Research Center, Technical University of Munich, D-85748 Garching, Germany*
[3]*Institute of Physical Chemistry & Center for Materials Research, Justus Liebig University, D-35392 Giessen, Germany*
[4]*Battery and Electrochemistry Laboratory (BELLA), Institute of Nanotechnology, Karlsruhe Institute of Technology (KIT), 76344 Eggenstein-Leopoldshafen, Germany*

A better understanding of the cathode active material (CAM) plays a crucial role in the improvement of lithium-ion batteries. We have previously reported the structural properties of the model cathode material $LiNiO_2$ (LNO) in dependence of its calcination conditions and found that the deviation from the ideal stoichiometry in $LiNiO_2$ (Ni excess) shows no correlation to the 1st cycle capacity loss. Rather, the morphology of LNO appears to be decisive. As CAM secondary agglomerates fracture during battery operation, the surface area in contact with the electrolyte changes during cycle life. Thus, particle morphology and especially the primary particle size become critical and are analyzed in detail in this report for LNO, using an automated SEM image segmentation method. It is shown that the accessible surface area of the pristine CAM powder measured by physisorption is close to the secondary particle geometric surface area. The interface area between CAM and electrolyte is measured by an in situ capacitance method and approaches a value proportional to the estimated primary particle surface area determined by SEM image analysis after just a few cycles. This interface area is identified to be the governing factor determining the 1st cycle capacity loss and long-term cycling behavior.
 [DOI: 10.1149/1945-7111/ac4bf3]

Manuscript received January 9, 2022. Published February 11, 2022.

In part I of this study,[1] the impact of the crystal structure on the initial reversibility of $Li_{1-z}Ni_{1+z}O_2$ was investigated and it was shown that, for small off-stoichiometry (z = 0.016–0.037), the excess Ni^{2+} in the Li layer does not explain the observed differences of the 1st cycle capacity loss. Besides the crystal structure, a key property of cathode active materials (CAMs) is their morphology. For commonly used CAMs, e.g., the commercially relevant layered transition metal oxides $Li(Ni_{1-x-y}Co_xMn_y)O_2$ (NCM) and $Li(Ni_{1-x-y}Co_xAl_y)O_2$ (NCA), the morphology can be subdivided into the secondary particle and primary particle scale.[2] The secondary particle morphology can typically be described as approximately spherical agglomerates in the size range of 5–15 μm that are built up from primary particles in the size range of a few hundred nm, with the primary particles in turn consisting of one or a few crystal domains.[3] The size of the secondary particle agglomerates is set during precipitation of the transition metal precursor,[4–6] and the primary particle size is determined by the calcination conditions as well as the chemical composition and morphology of the respective precursor.[7–10] In the first part of this study, it was found that there is some correlation, albeit not fully satisfactory, between the 1st cycle capacity loss and the average crystallite size determined by Rietveld refinement of synchrotron powder X-ray diffraction patterns. However, it was also highlighted that the refined crystallite size values just reflect averages over the whole powder samples.

Particle morphology of NCM materials has been in the focus of many recent studies, reporting improved electrochemical performances for "single crystal" materials[11–15] or materials with tailored orientation of the primary particles in regard to their secondary particle microstructure.[16–18] Liu et al. reported a correlation of the 1st cycle capacity loss of Ni-rich CAMs with increasing primary and secondary particle sizes.[19] However, a quantitative analysis of the particle size influence is still lacking. Thus, in this study a quantitative evaluation of the primary particle size distribution using an automated SEM image analysis is performed on a set of 18 LNO samples. The resulting primary particle size distributions as well as the secondary particle size distributions determined by laser scattering are compared to the outcome of krypton physisorption measurements for the pristine CAM powders. Furthermore, it is shown that post-processing of the CAM can change the specific surface area, for example by washing, which is often applied in industry to reduce the amount of Li residual salts after calcination.[20–22]

Using an in situ capacitance measurement approach introduced by Oswald et al.,[23] the interface area between CAM and electrolyte is monitored in half-cells during the initial cycles. For LNO it has repeatedly been reported that fracturing of the secondary particle agglomerates occurs when cycled over a critical voltage cut-off[24,25] and the concurrent intrusion of the electrolyte into the inner parts of the secondary particle structure increases the said interface area. Thus, as shown by Ruess et al., the increased interface area leads to a decrease of the areal current density when referenced to the electrochemically active surface area, and thus to improved lithiation kinetics during discharge.[26] Here, we report that the interface area becomes proportional to the primary particle specific surface area estimated by SEM image segmentation, and therefore remarkably impacts the electrochemical properties. In this regard, the differences in 1st cycle capacity loss for a large set of LNO samples can be explained. Further correlations with key electrochemical parameters (resistance build-up, cycling stability) have also been found and will be described. Finally, the importance of morphological control in future studies is highlighted.

Experimental

Sample preparation.—The investigated LNO samples were synthesized by a solid-state reaction starting from LiOH monohydrate and $Ni(OH)_2$ precursors, as described in part I of this study.[1] The secondary particle size of the $Ni(OH)_2$ precursor (nominally 4 μm and 12 μm), the maximum calcination temperature (680 °C, 700 °C and 720 °C), and the number of Li equivalents per mol of Ni (0.98, 1.01, 1.04) were varied.

*Electrochemical Society Member.
**Electrochemical Society Fellow.
=These authors contributed equally to this work.
[z]E-mail: felix.riewald@tum.de

Scanning electron microscopy (SEM) imaging.—For the measurement of top-view images, a small amount of cathode powder was fixed on a SEM pin holder (Agar Scientific, Ltd.) covered with conducting carbon cement (Plano GmbH). It was coated with a 6 nm thick platinum layer by sputter deposition (SCD 500 Sputter Coater, Bal-Tec AG). Measurements were performed using a SEM with a thermal field emission cathode and an Everhart-Thornley secondary electron detector at an operating voltage of 5 kV (Ultra 55, Carl Zeiss AG). Samples for cross section measurements were prepared by initially mixing 2 g of epoxy resin and 0.5 g of epoxy hardener (Buehler, ITW Test & Measurement GmbH), adding a few drops of the mixture to a small amount of cathode powder in a gelatine capsule, followed by 2 min of mixing with a spatula. Afterwards, the slurries were cast onto an Al-foil using a manual coater with a gap size of 0.5 mm and dried in an oven (Heraeus Holding GmbH) at 40 °C over night. Smaller sections were prepared with a scalpel, mounted on a customized mask and aligned with an optical microscope. Then, the samples were transferred to an ion milling system (ArBlade 5000, Hitachi, Ltd.), and cross sections were prepared by milling with an Ar ion beam at an operating voltage of 6 kV for two h. Images were taken as described above for the top-view measurements.

Image segmentation.—The algorithm used for image segmentation is based on a convolutional neural network using the U-Net architecture, which was initially developed for applications in biomedical image segmentation.[27] The algorithm takes the measured SEM intensity image as input and generates a score image, which assigns every pixel to an index of the particle it belongs to. A training data set was manually generated to train the algorithm with exemplary SEM images depicting typical CAM secondary agglomerates in the desired magnification. Raw lengths and areas were reported in the dimension of pixels and were afterwards converted to actual lengths and areas using a calibration factor from the image metadata. To increase the robustness of the segmentation, a post-processing step was performed. Firstly, regions touching the boundary of the image were rejected. Secondly, only objects were quantitatively evaluated, which fulfilled the following three criteria: the object had to have an area of 200 pixels or more, the compactness (ratio between the object's area and its convex hull) had to be $\geqslant 0.8$, and the circularity (4π times the area divided by the perimeter squared; circularity equals one for a perfect circle) had to be $\geqslant 0.6$. These criteria ascertained that only primary particles which did not deviate too much from the expected nearly spherical shape were recognized. The size of a primary particle was quantified by taking the area of the particle ($\boldsymbol{A}$) after segmentation and calculating the diameter of a circle with the same area, referred to as equivalent diameter d_{eq} in Eq. 1.

$$\boldsymbol{d_{\mathrm{eq}} = 2\sqrt{A/\pi}} \qquad [1]$$

Ten top view SEM images in 20 k magnification were measured for each of the 18 LNO samples to have a sufficient amount of particles for proper statistical evaluation.

To validate that the segmentation model worked properly for the LNO samples under study and to exclude any potential bias of the algorithm, a comparison with manually segmented images was made. For this purpose, manual segmentation was done for three representative samples and three images per sample using the ImageJ software.[28,29] Moreover, for a comparison of the particle size distribution between the surface of a secondary particle and its inner parts, cross section SEM images were analyzed for the same three representative samples again using the manual segmentation method with ImageJ.

Particle size distribution by laser scattering.—Samples were prepared by dispersing a small amount of cathode powder in deionized H_2O. Measurement of the particle size distribution was performed using laser scattering based on the Mie scattering theory (Mastersizer 2000, Malvern Panalytical GmbH). The cathode particles were assumed to have a refractive index of 2.19 (refractive index of NiO as specified by the supplier), and 1.33 was taken for deionized H_2O as dispersant. The intensity of the scattered laser beam was measured as a function of the scattering angle for particle sizes in the range of 0.05 μm to 70 μm (a combination of red and blue light was utilized). Three measurements per sample were performed, and average values were calculated.

Physisorption.—Physisorption measurements were performed to analyze the specific surface area of the pristine CAM powders. For this purpose, ~1 g of CAM was filled into the chamber of a gas sorption analyzer (Autosorb-iQ, Quantachrome Instruments, Anton Paar GmbH). Prior to the measurement, the powders were degassed at 120 °C for three hours. Krypton was used as adsorptive due to its higher accuracy when measuring low surface areas (typically $< 1\ \mathrm{m}^2$ for CAMs and small sample amounts), and the temperature during experiments was set to 77 K. Specific surface areas could be extracted from the adsorption isotherms in the relative pressure range of $0.05 < p/p_0 < 0.30$ using the Brunauer-Emmet-Teller (BET) theory.

Washing of CAMs was performed by adding deionized H_2O in a CAM:H_2O weight ratio of 1:5 and stirring for 20 min at a stirring speed of 200 rpm on a magnetic stirrer plate at room temperature. Afterwards, the washed CAMs were filtrated and dried in a glass oven (B585, Büchi Labortechnik AG) at 120 °C under dynamic vacuum for 12 h.

Electrode preparation.—Electrodes for electrochemical characterization were prepared by mixing the sample powders with conductive carbon (C65, Imerys Graphite & Carbon) and PVDF binder (Solef 5130, Solvay GmbH) at a 94:3:3 mass ratio. For this, a 7.5 wt% binder solution in N-methyl-2-pyrrolidone (NMP, BASF SE) was mixed with additional NMP and the conductive carbon, and mixed for at least 24 min at 2000 rpm in a planetary mixer (ARE 250, Thinky Corporation). The CAM powders were added to the obtained slurry and were mixed for additional 10 min. The solid content of the final slurries was 61 wt%. The slurries were cast onto an Al-foil (thickness 20 μm, Nippon Light Metal Co., Ltd.) using a box-type coater (wet-film thickness 100 μm, width 6 cm, Erichsen GmbH & Co. KG) and an automated coating table (5 mm s^{-1}, Coatmaster 510, Erichsen GmbH & Co. KG). The coated tapes were placed in a vacuum oven (VDL 23, Binder GmbH) and heated to 120 °C under dynamic vacuum for drying overnight. The dried cathode tapes were compressed using a calender (CA5, Sumet Systems GmbH) at a set line force of 30 N mm^{-1} and a roller speed of 0.5 m min^{-1}. Circular electrodes with a diameter of 14 mm were punched out using a high-precision handheld punch (Nogamigiken Co., Ltd). After weighing, the electrodes were transferred to an Ar filled glovebox for cell assembly. An average loading of (8.0 ± 0.5) mg cm^{-2} and an electrode density of (3.0 ± 0.2) g cm^{-3} were obtained (corresponding to a porosity of ~35%).

Half-cell testing.—Coin half-cells were built using a 2032 coin cell geometry. The cell stack consisted of the cathode, a glass fiber separator (ø 17 mm, 300 μm thickness, GF/D, VWR International, LLC.) soaked with 95 μl electrolyte (LP57, BASF SE), and a pre-punched lithium metal anode (ø 15.8 mm, thickness 0.58 mm, purity 99.9%, Shandong Gelon LIB Co., Ltd). After assembly the cells were crimped and closed in an automated crimper (Hohsen Corp.). The cells were then transferred to a climate chamber (Binder GmbH) and connected to a battery cycler (Series4000, MACCOR, Inc.). All tests were performed at 25 °C and the C-rate was chosen according to 1 C ≡ 200 mAg^{-1}. To calculate the 1st cycle capacity loss, the cells were charged at C/10 to 4.3 V and discharged at C/10 to 3.0 V.

Moreover, a test protocol was applied to calculate the capacitance of the half-cells as a function of cycle number, which will be described in detail in an upcoming publication.[30] Briefly, the cells were continuously cycled at C/10 with 4.3 V as upper voltage cut-off

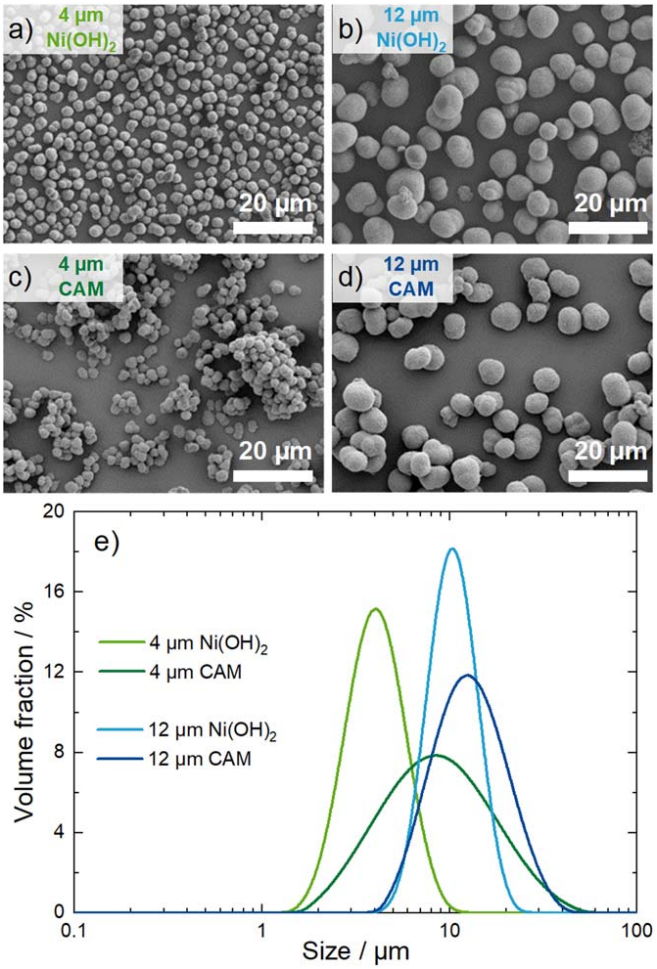

Figure 1. Secondary particle morphology of the $Ni(OH)_2$ precursors and selected lithiated and calcined (1.01 Li equivalents and 700 °C) LNO CAM samples from this study. SEM images of: (a) the nominal 4 μm precursor; (b) the nominal 12 μm precursor; (c) the LNO CAM based on the nominal 4 μm precursor; and (d) the LNO CAM based on the nominal 12 μm precursor. All images were recorded in 20 k magnification with an acceleration voltage of 5 kV. For better contrast, on top of all samples a 6 nm thick Pt layer was sputtered. The length of the white scale bar equals 20 μm. (e) Volume based particle size distribution measured by laser scattering of the nominal 4 μm (green) and 12 μm (blue) samples before (light) and after (dark) lithiation and calcination. As underlying model, the Mie scattering theory was used.

and a discharge to 2.5 V followed by a constant voltage step until the current dropped below C/250; in this fully lithiated state, the charge transfer resistance of layered transition metal oxide based CAMs becomes very large, leading to a so-called *blocking condition* response of the impedance.[23] In this condition, an alternating current with an amplitude of C/50 and a frequency of $f = 100$ mHz was modulated onto the C/250 base current. Both the modulated current and the respective voltage response were fitted to sine functions, from which the phase shift (θ) between voltage and current as well as the voltage/current amplitude ratio ($\hat{E}/\hat{I}$) were obtained. These in turn were used to compute the imaginary part of the impedance at 100 mHz ($\mathrm{Im}(Z_f) = \hat{E}/\hat{I}\cdot\sin(\theta)$). As shown by Oswald et al.,[23] the electrode capacitance (C) of CAMs is well represented by a single impedance measurement under blocking condition at frequencies near 180 mHz ($C \approx -1/(2\pi\cdot f\cdot \mathrm{Im}(Z_f))$; normalizing this value to the mass of the electrode yields the specific capacitance of the electrode (in units of $F\ g^{-1}_{electrode}$). As proven in a separate study,[30] the imaginary part of the impedance of the lithium counter electrode in this frequency range is neglibible, so that the determined capacitance closely corresponds to that of the cathode electrode. To account for the contribution of conductive carbon and PVDF binder to the measured electrode capacitance, electrodes without CAM were prepared at the same C:PVDF weight ratio of 1:1 as in the electrode, and half-cells were built as described above. Their impedance at 2.5 V and at a frequency of 100 mHz was measured with an impedance analyzer (VMP3, BioLogic GmbH & Co.KG), yielding a carbon-only electrode capacitance of $1.68\ F\ g^{-1}_{electrode}$ (note the higher specific capacitance in comparison to Oswald et al. due to the utilization of a carbon with higher specific surface area[23]); based on the weight fraction of C and PVDF in the LNO electrodes (i.e., 6 wt%), the contribution of carbon and binder to the LNO electrode capacitance is estimated to be $0.107\ F\ g^{-1}_{electrode}$ allowing then for the determination of the specific capacitance of the LNO active material only (in units of $F\ g^{-1}_{LNO}$).

Table I. The percentiles d_{10}, d_{50}, d_{90} and spans (calculated as $(d_{90}—d_{10})/d_{50}$)) of the $Ni(OH)_2$ precursors and two selected lithiated and calcined LNO materials from this study (with Li:Ni = 1.01, calcined at 700 °C) as measured by laser scattering.

Sample	d_{10} [μm]	d_{50} [μm]	d_{90} [μm]	Span
4 μm $Ni(OH)_2$	2.7	4.3	6.7	0.9
4 μm CAM	3.9	9.1	21.8	2.0
12 μm $Ni(OH)_2$	7.7	11.1	15.9	0.8
12 μm CAM	7.8	13.6	21.1	1.2

Full-cell testing.—Coin full-cells were built using a 2032 coin cell geometry. The cell stack consisted of the cathode, a polypropylene separator (ø 17 mm, C2500, Celgard, LLC.) soaked with 21 μl electrolyte (LP57, BASF SE), and a commercial graphite anode (ø 15 mm, loading of $7\ mg\ cm^{-2}$ and density of $1.5\ g\ cm^{-3}$, Elexcel Co.). To compensate for the thinner separator and anode compared to the half-cells, an additional stainless-steel spacer was added. All other steps were performed analogously to coin half-cells. All tests were performed at 25 °C and the C-rate was chosen according to $1\ C \equiv 200\ mAg^{-1}$.

The cells were first charged to 4.2 V and discharged to 3.0 V at constant current (CC) at a rate of C/10. In all following cycles, the charging condition was set to CCCV, with a constant current at C/2 to 4.2 V and a constant voltage (CV) step (until the current dropped below C/100 or after a CV time of 30 min). The cells were discharged at CC to 3.0 V and the discharge rate was varied with two cycles at C/10 and C/3, respectively, and 26 cycles at 1 C before repeating this procedure until a total number of 127 cycles was reached. At each second C/10 cycle, the cells were initially discharged to 50% state-of-charge (SOC, calculated relating to the discharge capacity of the former C/10 cycle) and a C/2 current pulse was applied for 30 s to calculate the direct current internal resistance (DCIR) of the cell, which was determined from the difference of the potentials just before the pulse and after a pulse time of 30 s.

Results and Discussion

Secondary particle morphology.—Figure 1e shows the particle size distributions of the nominal 4 μm (green) and 12 μm (blue) $Ni(OH)_2$ precursors and the respective calcined materials using 1.01 Li equivalents and 700 °C calcination temperature as measured by laser scattering. Numerically, the size distribution can be illustrated in terms of the percentile values, which represent the particle diameter below which 10%, 50% or 90% of all particles of the sample volume are found (d_{10}, d_{50}, d_{90}), as shown in Table I. The width of the distribution is represented by the so-called span, which is calculated as $(d_{90}–d_{10})/d_{50}$. For the two $Ni(OH)_2$ precursors, a clear particle size difference is observed with span values < 1. For the calcined samples, both the d_{50} values and the respective spans increase. This confirms that during calcination not only intraparticle, but also interparticle growth happens, leading to agglomeration of the secondary particles that can be discerned by comparing the

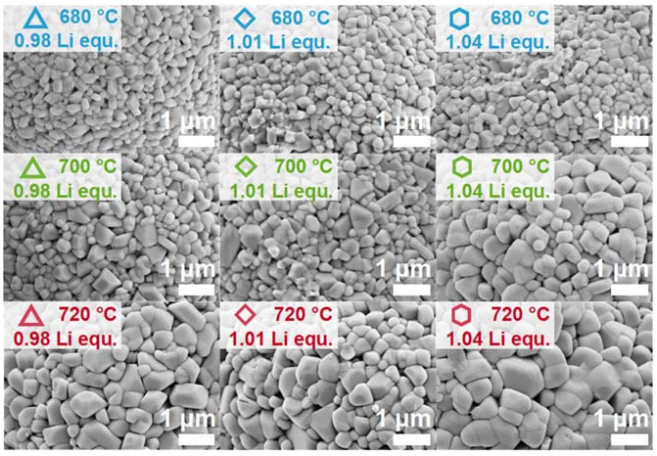

Figure 2. Top-view SEM images of the nominal 12 μm LNO samples made with different Li equivalents and at different calcinations temperatures (see legends). All images were recorded in 20 k magnification with an acceleration voltage of 5 kV. A 6 nm thick Pt layer was sputtered onto all samples. The length of the white scale bar equals 1 μm.

top-view SEM images of the precursors (Figs. 1a and 1b) with those of the respective CAMs (Figs. 1c and 1d). Considering the close-to-spherical shape of the secondary agglomerates of the precursor and the final LNO particles, their specific surface area (SSA) can be estimated by the spherical approximation for monodisperse solid and smooth spheres, using their d_{50} values given in Table I and considering the density of the $Ni(OH)_2$ precursor ($\rho = 4.1$ g cm^{-3}) or of the final LNO CAM ($\rho = 4.77$ g cm^{-3}):

$$SSA = \frac{A_{Particle}}{V_{Particle} \cdot \rho} \approx \frac{6}{d_{50} \cdot \rho} \quad [2]$$

For the nominal 4 μm and 12 μm diameter precursors, this SSA estimation on the basis of the d_{50} values in Table I results in SSA values of 0.34 and 0.13 m^2 g^{-1}, respectively; for the LNO CAMs derived from the 4 μm and 12 μm precursors, these estimated SSA values decrease to 0.14 and 0.09 m^2 g^{-1}, respectively. However, in reality the secondary particles can not be described as perfectly dense, smooth, and spherical, particularly in the case of the LNO CAMs where the above discussed agglomeration leads to porosity and surface roughness. In addition, for a more precise estimate (even in the case of solid and smooth spheres), the particle size distribution would have to be considered in Eq. 2. Therefore, the here given SSA values are only a first-order estimate and as such are expected to somewhat deviate from SSA values obtained by the krypton physisorption measurements that will be discussed later.

Primary particle morphology.—The primary particle size is more difficult to access as there is no direct way to measure its distribution. Although Rietveld refinement using powder X-ray diffraction (PXRD) data and an appropriate structural model yields values for the crystallite size, as was done in part I of this study, only average values are obtained and no information on the size distribution can be gained. In general, the primary particle morphology of CAMs is mainly investigated by the use of SEM imaging. Representative top-view SEM images for the LNO materials prepared with the nominal 12 μm $Ni(OH)_2$ precursor are depicted in Fig. 2. A clear impact of the calcination temperature and the number of Li equivalents per mol of Ni on the primary particle size was found, with an increase of both synthesis parameters leading to larger primary particle sizes. However, this approach only delivers a *qualitative* information and might lead to wrong conclusions if the examined section of the secondary particle agglomerate is not representative for the whole sample.

A *quantitative* information of the primary particle size was obtained by segmentation and subsequent determination of the primary particles' dimensions. By use of image processing software (ImageJ), this segmentation was done manually. However, for a thorough statistical analysis, a large number of SEM images and primary particles needs to be processed and segmentation merely by hand is a tedious and time-consuming task. With the ongoing improvements of computer vision methods and convolutional neural networks, such segmentation processes can now be automatized,

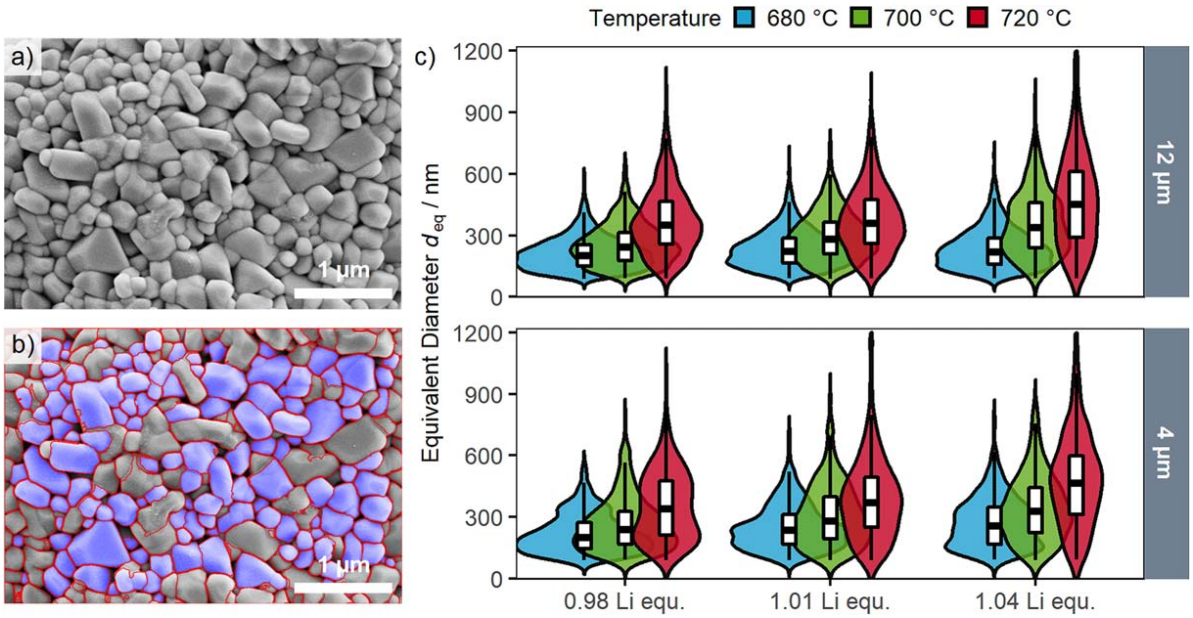

Figure 3. Analysis of the primary particle size distribution by top-view SEM analysis. (a) Top-view SEM image of an LNO sample (nominally 12 μm precursor, 1.01 Li equivalents, calcined at 700 °C) before and (b) after primary particle segmentation. The segmented particles are highlighted with a blue overlay. 10 images of individual secondary particles per sample were analyzed. (c) Violin plots of the primary particle size distributions derived from the automated image segmentation of all 18 LNO samples in this study. The upper panel depicts the samples prepared from the nominal 12 μm precursor, the lower panel the samples from the nominal 4 μm precursor, with the colors indicating the calcination temperature (blue: 680 °C, green: 700 °C, red: 720 °C). The *y*-axis shows the equivalent diameter and the width in *x*-axis direction indicates the probability density distribution as a kernel smoothed histogram. The boxes indicate the median as well as the 25% and 75% percentiles, with the whiskers extending to the 10% and 90% percentiles.

which is applied in various research fields from biomedicine to mineral characterization.[27,31] The feasibility of this method was further demonstrated for nanoscale agglomerated inorganic particles.[32] Hence, this approach was also used in this study, and an automatized segmentation of 10 top-view SEM images in 20 k magnification was performed for each sample to analyze a sufficiently large number of primary particles. Figures 3a and 3b show one top-view SEM image before and after the segmentation process for one representative LNO sample (nominally 12 μm precursor, with a Li:Ni molar ratio of 1.01, calcined at 700 °C). On average, more than 700 primary particles per LNO sample were evaluated, with a smaller number of primary particles being identified in case of larger primary particle sizes (less particles visible in the images). Table II shows the numerical results of this SEM analysis for the differently synthesized LNOs, viz., the equivalent primary particle diameter and its standard error of the mean for a given sample (d_{eq}), the volume/surface averaged diameter ($d_{v/a}$ as described later), the resulting primary particle SSA, and the number of segmented particles per sample that were used to determine these values.

The equivalent diameter as a measure for the primary particle size is depicted in Fig. 3c for all 18 LNO samples from this study as a function of the calcination temperature and of the number of Li equivalents, broken down by the size of the used $Ni(OH)_2$ precursor. The size distributions are depicted as violin plots with overlayed box plots that show the median values and the 10%, 25%, 75% and 90% percentiles. All size distributions roughly follow a log normal distribution, which is commonly found for materials with Ostwald ripening as underlying growth mechanism.[33,34] The qualitative information from Fig. 2 can be confirmed by evaluation of the size distributions, as increasing calcination temperature and number of Li equivalents both lead to larger median primary particle sizes. Additionally, this quantitative evaluation also shows that the width of the size distribution increases as the primary particles become larger. No large differences between the two used $Ni(OH)_2$ precursors were observed, indicating that the secondary particle size of the precursor (and thus of the final LNO CAM) is not impacting primary particle growth.

To exclude systematic errors by this newly implemented computer vision method, two additional validation tests were made. As seen in Fig. 3b, the computer vision method is not able to segment all primary particles shown in the SEM image, as it rejects particles which touch the boundaries of the image, deviate to a large extent from the expected particle shape, or for which the junctions between the primary particles are not fully clear (this occurs, e.g., when primary particles are covered with residual Li salts from the calcination process). Therefore, a manual segmentation (three selected samples and three images per sample) was performed to investigate a possible bias of the segmentation algorithm in regards of which particles are segmented and which are rejected (Fig. 4). The overall shape of the particle size distributions is similar for both methods, and a deviation $< 10\%$ for the mean primary particle sizes is found. This minor deviation can be ascribed to a selection bias (only three images were analyzed by hand) or to the fact that sometimes the junctions between particles cannot be clearly identified.

Another systematic deviation could potentially arise from differences between the size of the primary particles located on the exterior surface of the secondary particles, which are measured by top-view SEM, and the size of the primary particles located in the

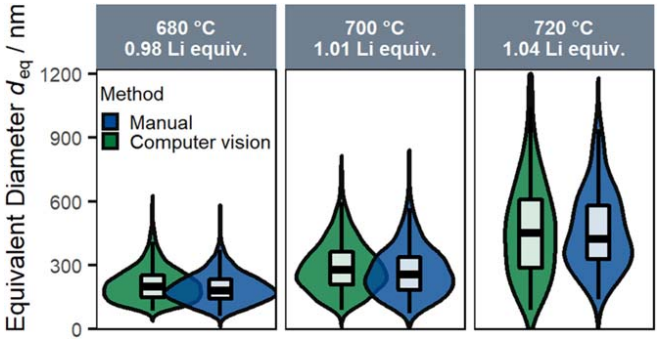

Figure 4. Comparison of the primary particle size distributions derived from top-view SEM images, obtained by the computer vision segmentation (green) and by manually mapping the primary particle segmentation (blue), shown exemparily for three LNO samples prepared from the nominal 12 μm precursor (the Li equivalents and the calcination temperature are specified in the legends). For the manual mapping, three selected SEM images in 20 k magnification were analyzed using the ImageJ software.

Table II. Results from the top-view SEM image analysis by segmentation for all 18 LNO samples of this study, providing the Li:Ni molar ratio and the calcination temperature ($T_{calc.}$). The table depicts the primary particle size by means of the average equivalent diameter d_{eq} (see Eq. 1) and its standard error of the mean, the resulting volume/area averaged diameter ($d_{v/a}$) for each sample (calculated with Eq. 4), and the corresponding primary particle specific surface area (SSA) calculated with Eq. 3. The last column gives the total number of segmented particles per sample.

LNO sample Li:Ni | $T_{calc.}$	d_{eq} values [nm]	$d_{v/a}$ diameter [nm]	Primary part. SSA [m^2 g^{-1}]	# of segmented particles
		Prepared from nominally 12 μm precursor		
0.98 | 680 °C	210 ± 2	270	4.7	1672
0.98 | 700 °C	254 ± 3	335	3.8	1463
0.98 | 720 °C	371 ± 6	503	2.5	683
1.01 | 680 °C	234 ± 2	305	4.3	1598
1.01 | 700 °C	294 ± 4	385	3.3	1072
1.01 | 720 °C	375 ± 7	505	2.5	539
1.04 | 680 °C	235 ± 3	316	3.9	1336
1.04 | 700 °C	359 ± 6	487	2.6	661
1.04 | 720 °C	475 ± 12	701	1.7	382
		Prepared from nominally 4 μm precursor		
0.98 | 680 °C	220 ± 4	301	4.2	649
0.98 | 700 °C	263 ± 6	389	3.0	447
0.98 | 720 °C	353 ± 10	497	2.4	274
1.01 | 680 °C	250 ± 4	345	3.6	594
1.01 | 700 °C	306 ± 7	442	2.8	418
1.01 | 720 °C	386 ± 14	577	2.1	192
1.04 | 680 °C	274 ± 5	378	3.3	498
1.04 | 700 °C	345 ± 8	484	2.5	386
1.04 | 720 °C	478 ± 17	666	1.7	171

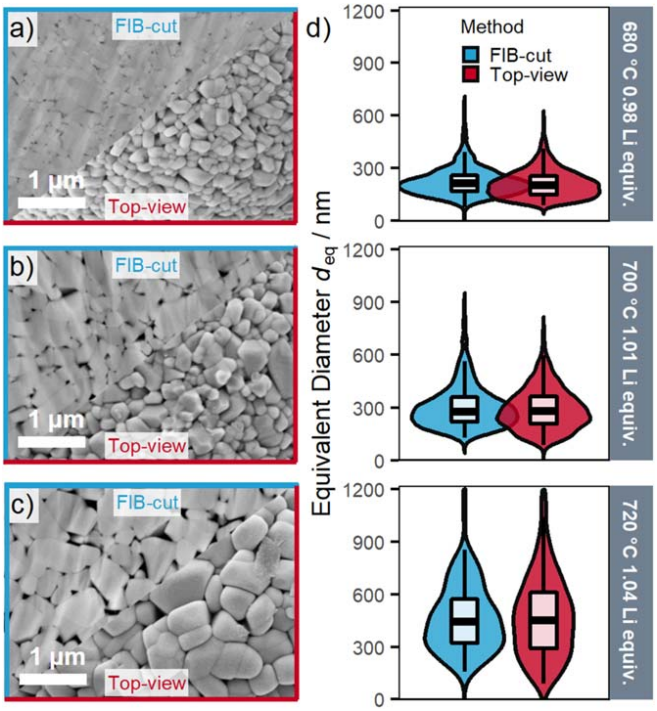

Figure 5. Comparison of the LNO primary particle size distributions obtained by analyzing top-view SEM images or SEM images obtained from ion-milled SEM cross-sections. For this, LNO samples derived from the nominal 12 μm precursor and showing the largest differences in primary particle size were chosen to compare the cross-section (blue-framed upper left sections) and top-view (red-framed lower right sections) SEM images: (a) for the sample calcined at 680 °C with 0.98 Li equivalents per mol of Ni; (b) for the sample calcined at 700 °C with 1.01 Li equivalents; and (c) for the sample calcined at 720 °C with 1.04 Li equivalents. (d) Comparison of the primary particle size distributions between cross-section (blue) and top-view (red) SEM image segmentation. For the cross-section images, particle segmentation was performed manually, using the ImageJ software.

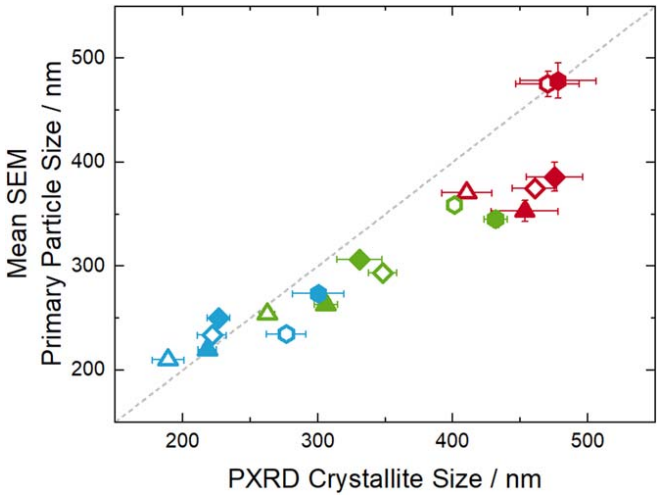

Figure 6. Comparison of the LNO average crystallite sizes obtained from Rietveld refinement using synchroton PXRD data with the mean primary particle size obtained from the segmentation of top-view SEM images. The colors refer to the three different maximum calcination temperatures (680 °C: blue, 700 °C: green, 720 °C: red), symbols indicate three different Li equivalents (0.98: triangles, 1.01: diamonds, 1.04: hexagons) and open/closed symbols represent LNO derived from the nominal 12 and 4 μm precursors, respectively. The gray dashed line represents a line through the origin with the slope of 1.

interior of the secondary particles, which can be accessed by FIB-cut cross-section images as shown in Fig. 5. Due to the poor contrast between the primary particles and the background, the cross-section images (three selected samples and three images per sample) were evaluated by manual segmentation. Only minor differences can be found between top-view and cross-section SEM images, which shows that the primary particle sizes on the exterior surface of the secondary particles and those located in the interior region are comparable. However, for the cross-section images it must be considered that the primary particle size could be underestimated, as the FIB-cut might not perfectly intersect the equator of the secondary particle. The cross-section images further reveal that not only the primary particle size increases with an increase of the calcination temperature and of the number of Li equivalents, but also the size of the pores inside the secondary particle agglomerates increases.

The above determined SEM top-view based primary particle size distribution in terms of the equivalent diameter can now be used to estimate the SSA values of the primary particles, using the spherical approximation of solid and smooth spheres and an LNO density of $\rho = 4.77$ g cm^{-3}.[35]

$$SSA = \frac{\sum A_{Particle(i)}}{\sum V_{Particle(i)} \cdot \rho} = \frac{\pi \cdot \sum d_{eq\,(i)}^2}{\pi/6 \cdot \sum d_{eq\,(i)}^3 \cdot \rho} = \frac{6}{d_{v/a} \cdot \rho} \quad [3]$$

Hereby, the volume/area averaged diameter $d_{v/a}$ is defined as:

$$d_{v/a} = \frac{\sum d_{eq\,(i)}^3}{\sum d_{eq\,(i)}^2} \quad [4]$$

The $d_{v/a}$ values for the different LNO samples are listed in Table II, together with the resulting primary particle SSA values based on Eq. 3. The primary particle SSA values shown in Table II range from 4.7 m^2 g^{-1} for the smallest primary particles to 1.7 m^2 g^{-1} for the largest primary particles, and thus are roughly one order of magnitude larger compared to the values estimated from the secondary particle sizes.

Figure 6 compares the average primary particle size values from the top-view SEM image segmentation (in terms of d_{eq}) with the crystallite diameters obtained from Rietveld refinement using synchrotron powder X-ray diffraction (PXRD) data shown in Part I of this study.[1] These two methods should yield the same primary particle size values, if a primary particle consists of only one crystal domain. As a matter of fact, a good agreement is found, with the primary particle size determined by the SEM analysis and the average crystallite size agreeing reasonably well for most of the 18 LNO samples. However, it should be noted that the observed small differences are to be expected due to the different physical nature of the two methods: in PXRD, larger crystallites contribute more to the overall diffraction pattern (volume-based method), whilst for SEM imaging each particle contributes equally to the mean (number-based method). The advantage of the latter method is that the primary particle size distribution that can be obtained from top-view SEM image segmentation allows to obtain a more accurate primary particle SSA, which is necessarily less accurate for the single size value obtained by PXRD.

Ex situ krypton physisorption.—Experimental values of specific surface areas of LNO powders are obtained *ex situ* from physisorption measurements, where the amount of adsorbed gaseous species to the surface of the material is measured. The accuracy of this method is limited by the used adsorptive and can be increased by the use of Kr instead of the more commonly applied N_2, which is due to the lower vapor pressure of Kr at the measurement temperature of 77 K (boiling point of liquid nitrogen). In the case of low absolute surface areas of a given sample (i.e., when the total surface area of

the sample is < 1 m^2), only measurements using krypton can yield sufficiently accurate values.[23,36]

Kr physisorption measurements (Kr-BET) were performed for six selected LNO samples (i.e., for three LNO samples for each $Ni(OH)_2$ precursor, which exhibit large differences in primary particle size), and the results are shown in Table III, together with the SSA estimates for the secondary particle size obtained by laser scattering (using the d_{50} value and Eq. 2) and for the primary particle size obtained by top-view SEM segmentation (values also listed in Table II, based on Eq. 3). For the LNO powders based on the nominal 12 μm precursor, Kr-BET values between 0.18 m^2 g^{-1} and 0.34 m^2 g^{-1} were obtained (fourth column from the left in Table III), with an increase of specific surface area for samples with a larger primary particle size. Comparing those values with the estimated SSAs on the secondary and primary particle level for each LNO sample (second and third row from the left, respectively) reveals that the Kr-BET values are closer to the estimated SSAs of the secondary particles. This means that the inner pore structure is not accessible to the krypton adsorptive, which, e.g., may be due to residual lithium salts from the LNO synthesis blocking the pores. However, the measured Kr-BET values are still larger than the estimated SSAs of the corresponding secondary agglomerates, which is likely due to a small fraction of accessible pores in the secondary agglomerates, whereby the larger pores formed with larger primary particles (see Figs. 5a–5c) would explain the increase of the Kr-BET values with primary particle size. For the LNO powders based on the nominal 4 μm precursor, generally larger Kr-BET values were observed. This is in line with the observation that it is indeed the secondary particle structure that most affects the Kr-BET value, so that smaller secondary particles yield higher Kr-BET values.

Given that the inner pore network appears to be likely blocked by residual Li salts, removal of these impurities is expected to increase the measurable specific surface area. The amount of residual salts can be substantially reduced by washing with H_2O, subsequent filtering and drying, which was done for the three LNO samples based on the nominal 12 μm precursor. As shown in Table III (rightmost column), for all of these three samples a very pronounced increase in the Kr-BET SSA can be observed, ranging between a factor of $\sim$4 (from 0.34 to 1.24 m^2 g^{-1}) and $\sim$8 (from 0.18 to 1.50 m^2 g^{-1}). A similar increase of the Kr-BET surface area upon washing was also observed for NCM811.[37]

To further illustrate the emerging trends of the SSAs, Fig. 7 shows the estimates of the primary particle and secondary particle specific surface areas as well as the Kr-BET values before and after washing, plotting the data given in Table III. This makes it very obvious that the Kr-BET SSA values of the pristine LNO powders (labeled as B in Fig. 7) come rather close to the SSA estimated for the corresponding secondary particles (labeled as A). After washing, the Kr-BET SSA values are significantly increased (labeled as C) and move more towards the estimated SSA for the primary particles (labeled as D). Although the sample with the smallest primary particles (0.98 Li equivalents and 680 °C calcination temperature, marked in blue) has the largest measured Kr-BET value after washing (1.50 m^2 g^{-1}), this value is still significantly lower than the estimate for completely separated primary particles (4.7 m^2 g^{-1}). For the samples with the largest primary particles (1.04 Li equivalents and 720 °C calcination temperature, marked in red), the measured SSA after washing comes closer to the estimated primary particle SSA. The cross-section SEM images already shown in Fig. 5 can be used to explain this phenomenon: with increasing primary particle size also the average pore size between the primary particles increases (with a concomitant decrease of the overall number of pores). These larger pores can be opened more easily by washing compared to the smaller pores of samples with small primary particles, which makes more of the inner pore network accessible by an improved percolation.

LNO electrode and LNO CAM capacitance.—As already shown by the Kr-BET data, the SSA values can experience drastic changes depending on sample treatment. However, for the electrochemical performance, the actual interface area between CAM and electrolyte is assumed to be the decisive parameter. The fracturing of the secondary particle structure during electrochemical cycling is a well-known phenomenon for Ni-rich NCM materials.[38–41] However, most investigations of this phenomenon rely on post mortem SEM analysis of the cycled electrodes, which only delivers qualitative information on a small section of the electrode and requires the destruction of the cell after cycling in order to conduct the analysis. Recently a method has been published that delivers the cathode capacitance (proportional to the electrochemically active specific interface area between CAM and electrolyte) in situ during battery operation by an impedance-based analysis in a three electrode set-up using a gold-wire reference and a prelithiated LTO anode.[23] Moreover, it will be shown in an upcoming report that similar results can be achieved in a simple two-electrode half-cell set-up using a Li metal anode, as is done in the present study.[30]

To investigate the changes of the SSA during cycling, this method was applied to all 18 LNO samples of this study and the results are depicted in Fig. 8. The principle of the test procedure is shown in the voltage profile in Fig. 8a (for further details see Oswald et al.[23]): after an initial charge to 20 mAh g^{-1} (referred to as "conditioning"), the cells were deep-discharged to 2.5 V followed by a CV step until the current dropped below C/250 (0.4 mA g^{-1}). The impedance was measured by imposing a 100 mHz current perturbation with a current amplitude corresponding to C/50 on top of the baseline current and analyzing the voltage response. The cells were cycled for five more full cycles up to 4.3 V, followed again by a deep discharge to 2.5 V after each cycle and by an impedance measurement at 100 mHz.

The specific electrode capacitance values as a function of cycle number are shown in Fig. 8b. After the conditioning step and before the first charge to 4.3 V, the capacitance values of the LNO samples based on the nominal 4 μm precursor are generally larger compared to those based on the nominal 12 μm precursor, which is in line with the higher SSA values measured by Kr-BET. However, for all samples the capacitance values drastically increase even after the 1st cycle with 4.3 V upper cut-off voltage. After the 5th cycle, no further increase of the capacitance values is noticed. This differs from previous observations made for NCM622 materials (60% Ni content), where capacitance increase over several hundreds of cycles was measured.[23] This seems consistent with the reported larger anisotropic volume changes during cycling for LNO compared to a NCM material with less Ni content,[42,43] even though it must be considered that the difference might also arise from a lower SOC for the NCM622 material, since the volume changes of NCMs with different Ni contents only depend on the SOC rather than the voltage.[44] A clear dependence of the maximum LNO electrode capacitance values after the 5th cycle on the calcination conditions is observed (Fig. 8b), with higher capacitances obtained for lower calcination temperatures (high impact) and lower Li equivalents (moderate impact). This is in good agreement with the observed trends of primary particle growth (Fig. 3c) and respective decrease of the primary particle SSA (see Table II).

Figure 8c shows the correlation between the specific LNO capacitance after the conditioning step, after the 1st cycle, and after the 5th cycle plotted against the primary particle SSA values determined from top-view SEM image segmentation (listed in Table II). After conditioning, the measured specific LNO capacitance values depend mostly on the secondary particle size, yielding higher values for the smaller secondary particles obtained for the LNO materials based on the nominal 4 μm precursor (i.e., for the LNO samples with lower secondary agglomerate SSA), while there is no clear correlation with the primary particle SSA. After the 1st cycle, a weak correlation of specific LNO capacitance with the primary particle SSA can be observed, which is further enhanced after the full five cycles. The samples with smaller primary particles tend to show a delayed particle fracturing and a slower increase of capacitance. The nearly linear correlation after the 5th cycle

Table III. Estimated secondary and primary particle specific surface areas (SSAs) for selected LNO samples with large differences in primary particle size, as well as the SSAs measured by krypton physisorption (Kr-BET) of the the pristine LNO powder and, in case of the LNO samples derived from the nominal 12 μm precursor, also for the washed LNO powders.

LNO sample Li:Ni | $T_{calc.}$	Secondary particle SSA[a] [$m^2\ g^{-1}$]	Primary particle SSA[b] [$m^2\ g^{-1}$]	Kr-BET of pristine LNO powder [$m^2\ g^{-1}$]	Kr-BET of washed LNO powder [$m^2\ g^{-1}$]
		Prepared from nominally 12 μm precursor		
0.98 | 680 °C	0.09	4.7	0.18	1.50
1.01 | 700 °C	0.09	3.2	0.26	1.34
1.04 | 720 °C	0.09	1.7	0.34	1.24
		Prepared from nominally 4 μm precursor		
0.98 | 680 °C	0.14	4.2	0.50	—
1.01 | 700 °C	0.14	2.8	0.51	—
1.04 | 720 °C	0.14	1.7	0.52	—

a) determined from the d_{50} diameter obtained by laser scattering, using Eq. 2. b) determined from segmentation of top-view SEM images, using Eq. 3 (also listed in Table II).

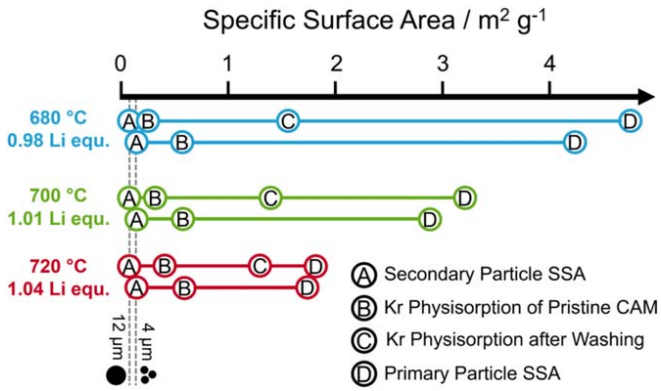

Figure 7. Specific surface areas (SSAs) of the samples with large differences in primary particle sizes for LNO materials prepared from the nominal 12 μm and 4 μm $Ni(OH)_2$ precursors. The SSA increases from the left to the right. The symbols labeled A indicate the estimated SSA of the secondary particles, based on the spherical approximation (Eq. 2 using the d_{50} diameter determined by laser scattering and density of the LNO calcinates from Fig. 1). Label B shows the Kr-BET SSA values of the pristine LNO powders, while label C depicts the Kr-BET SSA values of the LNO powders after washing (CAM:H_2O in a weight ratio of 1:5, washed for 20 min at room temperature). Label D marks the estimated primary particle SSAs obtained from the segmentation of the top-view SEM images, using Eq. 3.

indicates that the specific LNO capacitance increases to values proportional with the primary particle SSA, which means that at least a large fraction of the secondary particle structure is penetrated by the electrolyte due to crack formation between the primary particles. Therefore, it is expected that the primary particle size will have a significant impact on key electrochemical performance properties, which will be discussed in the following.

1st cycle capacity loss.—In part I of this study, the comparison between the exact LNO stoichiometry ($Li_{1-z}Ni_{1+z}O_2$) and the 1st cycle capacity loss was discussed, but no correlation was found for this set of samples.[1] In contrast, a weak correlation with the average crystallite size determined by Rietveld refinement was found. With an increase of interface area between the LNO active material and the electrolyte, the effective areal current density at a given C-rate is reduced. Thus, if the 1st cycle capacity loss were to be governed by a kinetic hindrance of the LNO active material at a high degree of lithiation, as suggested in the literature,[19,45,46] an increase in interface area would be expected to lead to a decrease of the 1st cycle capacity loss. In contrast, if the 1st cycle capacity loss would be caused by irreversible side reactions at the CAM surface (e.g. electrolyte oxidation or oxygen release[47,48]), an increase in SSA would be expected to lead to in increase in the 1st cycle capacity loss.

The interface area between the LNO surface and the electrolyte can be monitored during cycling by the capacitance method, and the respective correlation to the 1st cycle capacity loss is shown in Fig. 9. Here, a clear correlation is found for the whole set of samples, with a decrease in the 1st cycle capacity loss with increasing specific LNO capacitance, i.e., with increasing interface area. Therefore, for LNO samples with small values of z (ranging between 0.016–0.037), the CAM-to-electrolyte interface area is the decisive factor determining the 1st cycle coulombic efficiency.

This has profound implications for commercially relevant NCM and NCA materials. Here, particle fracturing is delayed over a large number of cycles due to the lower degree of delithiation when charged to an identical cut-off voltage. So far, particle fracture is often discussed as a detrimental effect on CAM performance, as it deteriorates the mechanical integrity of the cathode and increases the contact area for possible side reactions with the electrolyte.[41] However, as already concluded by Ruess et al.,[26] the intrusion of the electrolyte into the secondary particle structure and the related increase of interface area results in a decrease of the areal current density and therefore improves the Li intercalation kinetics during discharge. This means that even when material degradation already sets in at the very beginning of cycle-life, a concomitant continuous increase of CAM-to-electrolyte interface area can potentially counterbalance the capacity loss by side reactions to some extent. Indeed, several authors observed an increase of discharge capacity during the beginning of cycle-life, often after the materials were modified by doping, coating, or storage experiments, all influencing morphological or surface features of the CAM.[49–55] For LNO, this is rarely reported due to the rapid increase in interface area and the comparably large primary particles in comparison to Co and Mn containing materials with less Ni content.[56] In case of samples with very small primary particles, as observed by Mesnier et al., when calcining LNO at elevated oxygen pressure, such behavior is indeed implied.[57] This also indicates that comparing different materials concerning their discharge capacity without profound knowledge of the particle morphology can result in misleading conclusions.

Charge/discharge cycling of LNO/graphite full-cells.—To analyze the long-term cycling stability, full-cells were investigated for all LNO materials prepared in this study, with the results depicted in Fig. 10. The discharge capacity and the direct current internal resistance (DCIR) vs. cycle number for three exemplary LNO samples with a large variation in primary particle size distribution are shown in Figs. 10a and 10b, respectively. Although all materials are nominally "$LiNiO_2$," distinct differences are observed, with the C/10 discharge capacity after 122 cycles ranging from 150 mAh g^{-1} to 170 mAh g^{-1} (for LNOs based on the nominal 12 μm precursor,

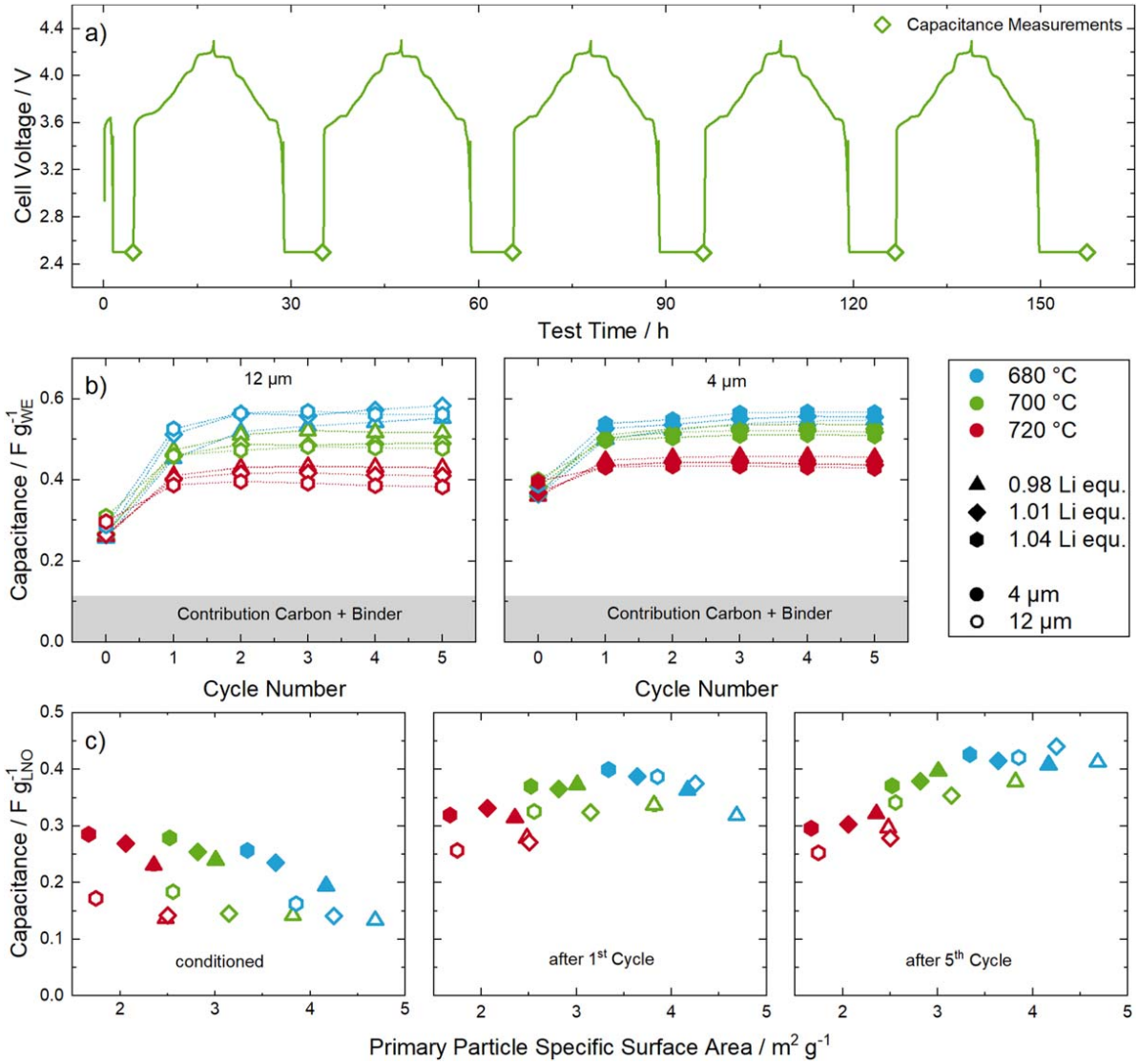

Figure 8. Capacitance measurements of all 18 LNO samples. (a) Voltage profile of an exemplary half-cell measurement. The points at which the capacitance measurements are performed are highlighted by green diamonds. (b) Electrode capacitance evolution over 5 cycles for the LNO samples based on the nominal 12 μm precursor (left panel) and on the nominal 4 μm precursor (right panel). The electrode capacitance is normalized on the total weight of the working electrode (WE). The gray box indicates the estimated contribution of carbon black and binder to the elecrode capacitance. (c) Correlation of the specific LNO capacitance (after substraction of carbon and binder contribution and normalized on the LNO active material weight) after conditioning (left), after the 1st cycle (middle), and after the 5th cycle (right), plotted versus the primary particle specific surface area (SSA) determined by top-view SEM image segmentation. All measurements were performed in a coin half-cell setup with a lithium metal anode, an LNO working electrode, and a glass fiber separator soaked with LP57 electrolyte. The measurement temperature was set at 25 °C and cycling was conducted at C/10 ($\equiv$ 20 mA g^{-1}). The capacitance was determined by discharging the cells to 2.5 V and holding the potential until the current drops below C/250; subsequently, a sine-wave modulated current with a frequency of 100 mHz and an amplitude corresponding to C/50 was superimposed to determine the electrode capacitance (see Experimental section).

prepared with 1.04 Li equivalents and 720 °C calcination temperature and with 0.98 Li equivalents and 680 °C calcination temperature, respectively). Despite the clear difference in the 1st cycle capacity at C/10 for all three materials, the capacity loss between the 1st and the 122nd cycle (both at C/10) is rather similar (50-65 mAh g^{-1}). Interestingly, when comparing the capacity loss between beginning and end of cycling at 1 C (6th and 121th cycle), it has a similar magnitude, ranging between 40 mAh g^{-1} for the best performing material (blue symbols in Fig. 10a) and 60 mAh g^{-1} for the lowest performing material (red symbols).

Generally, the degradation of the discharge capacity during repeated cycling is discussed in connection with an increase of the internal resistance of the cell, as both are related to the different degradation modes of the CAM.[37,39,58–60] When the structural degradation of the CAM leads to an impedance build-up, its overpotential at a given current increases, leading to a decrease of the capacity for a given set of upper and lower cut-off potentials. This, however, does not seem to be the case here, as an impedance build-up would more strongly affect the capacity loss at high C-rates, contrary to what is observed. Furthermore, the highest DCIR resistance increase is observed for the best performing LNO sample (with 0.98 Li equivalents and 680 °C calcination temperature; blue triangles in Fig. 10b): although all samples start with a DCIR of $\sim$30 Ωcm^2, it increases to 60-80 Ωcm^2 after 123 cycles, with the largest increase for the best performing sample. To investigate whether this behavior is correlated to the LNO particle morphology, the discharge capacity and the DCIR values of all 18 LNO samples after 122 cycles are compared to the primary particle SSA determined from the SEM image analysis, which is shown in Figs. 10d and 10e. This reveals rather obvious and striking correlations between the discharge capacities as well as the DCIR values with the primary particle SSAs, implying that these key electrochemical performance

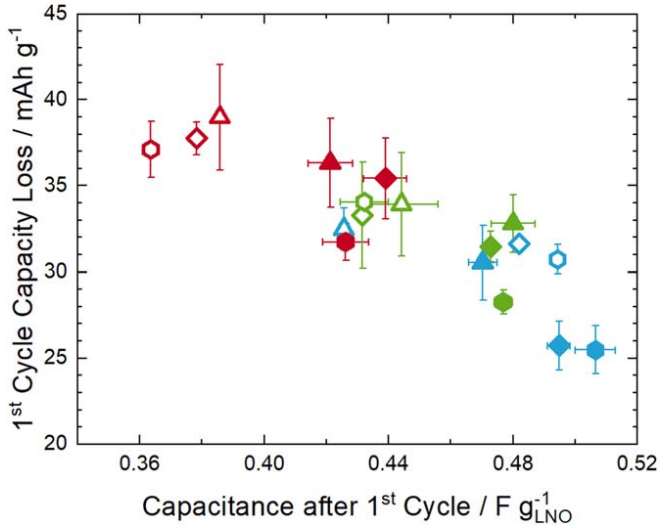

Figure 9. Correlation of the 1st cycle capacity loss with the specific LNO capacitance after the 1st cycle (taken from the middle panel of Fig. 8c). The error bars represent the deviation between two reproductions of the same test. All measurements were performed in a coin half-cell setup with a lithium metal anode, an LNO working electrode, and a glass fiber separator soaked with LP57 electrolyte. The measurement temperature was set at 25 °C and the cycle was conducted at C/10 (≡ 20 mA g^{-1}). The meaning of the different symbols is defined in Fig. 8b.

parameters seem to solely depend on the primary particle morphology. However, the observed trend that LNO materials with a high capacity retention also show a high DCIR increase over cycling seems to be contradictory at first sight, and a deeper understanding of this observation is sought.

For CAMs that exhibit no structural deterioration ($LiFePO_4$, $LiCoO_2$, NCM523 at low upper cut-off potentials), the main degradation mode of full-cells with these CAMs is the continuous growth of the solid electrolyte interphase (SEI) at the anode, which is connected to the consumption of cyclable lithium.[15,61,62] In such a case, the Li content of the cathode active material at the end-of-charge stays constant, while the amount of Li that is reintercalated at the end-of-discharge continuously decreases (i.e., even though the CAM could still accommodate more Li, no more lithium can be provided by the graphite anode). For Ni-rich CAMs, the amount of extractable Li during charge also decreases during cycle life.[37,59,63–65] This phenomenon has been related to the formation of a rock-salt like surface layer, which some authors suggested to increases the charge transfer resistance (and thus lower the charge capacity),[59] while other authors suggested that it would suppress the H2 to H3 phase transition (and thus the related capacity) due to the crystal lattice mismatch with the delithiated layered phase.[63] Thus, the x in Li_xNiO_2 at the end-of-charge would decrease during cycle life. Assuming that the formation of the rock salt-like surface layer is limited to a certain thickness (due to a diffusion limitation of the lattice oxygen from the bulk to the surface),[66] the mass fraction of the rock salt-like surface layer would increase with an increase of the accessible specific surface area of the CAM, as

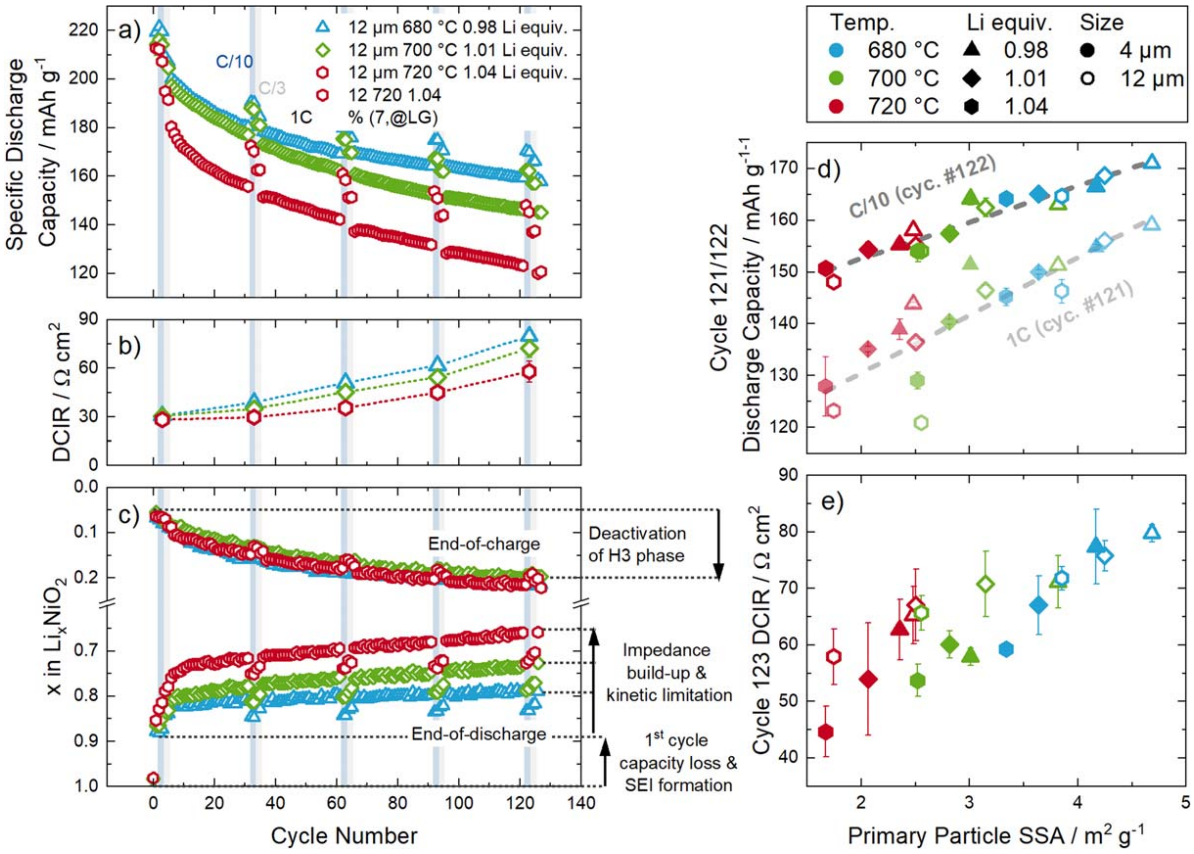

Figure 10. LNO/graphite coin cell data of the LNO samples. (a) Discharge capacity vs. cycle number at 1 C discharge, with intermittent check-up cycles at C/10 and C/3 discharge rate for three selected LNO materials with the largest difference in primary particle size based on the nominal 12 μm precursor. (b) DCIR vs. cycle number for these three LNO samples. (c) Estimated lithium content at end-of-charge and at end-of-discharge calculated from a dQ/dV analysis by determining the minimum corresponding to the single-phase region $Li_{0.5}NiO_2$. (d) Correlation of the 1 C and C/10 discharge capacity in cycle 121 and 122, respectively, with the primary particle SSA (from SEM analysis) and of (e) the DCIR values in cycle 123 for all 18 LNO samples. The cells consisted of a cell stack of an LNO cathode, a polypropylene separator soaked with LP57 electrolyte, and a graphite anode, with a nominal areal capacity of 1.6 ± 0.1 mAh cm^{-2} (based on 200 mAh g_{LNO}^{-1}). The cells were cycled between 3.0 and 4.2 V at a temperature of 25 °C. The CCCV charge rate was fixed to C/2 and until the current drops below C/100. The discharge rate was varied between C/10, C/3 and 1 C.

the surface phase grows from the surface inwards. However, if the crystal lattice mismatch is the origin of the capacity loss, the surface degradation would lead to a complete deactivation of the H3 phase formation in the bulk of the CAM particle, hence the capacity loss during charge would be independent from the primary particle size. Although larger primary particles form less of the degraded phase, the same capacity related to the H3 phase would be lost when compared to CAMs with smaller primary particles. This phenomenon would therefore not be able to explain the observed performance increase with primary particle SSA. Likewise to the loss of capacity during charge, the decreasing amount of lithium that can be reintercalated during discharge must be considered over the whole cycle life, as large differences were observed in the 1st cycle (Fig. 9).

The phase transitions of LNO can be used as a diagnostic measure to determine the absolute SOC, as has already been demonstrated in part I of this study.[1] Minima in the *dQ/dV* correspond to single phase regions that form due to Li ordering states.[67] In the monoclinic domain, a stable phase is reliably observed in the *dQ/dV* plots, corresponding to $Li_{0.5}NiO_2$. Following the minimum in the d*Q*/d*V* related to this phase over cycle-life, one can calculate the lithium content of LNO both at the end-of-charge and end-of-discharge, which then allows to distinguish the loss of capacity occurring at high and low state-of-charge (i.e., at low and high Li content, respectively). The thus determined Li contents of the LNO samples at the end-of-charge and end-of-discharge are shown in Fig. 10c. Indeed, for the three samples with large differences in primary particle size, the amount of extracted Li at the end-of-charge decreases absolutely identically, which in turn indicates that the observed large differences in discharge capacity arise from the amount of Li that can be reintercalated at the end-of-discharge. The decrease of discharge capacity cannot solely be explained by a loss of Li in the SEI, as a decrease of the discharge rate (1 C to C/3 to C/10) leads to an increase of measured discharge capacity (i.e., there is still sufficient active Li present in the anode). The similar fading behavior at C/10 and 1 C (Fig. 10d) also excludes an impact of the deterioration of the electrical conductivity caused by fracturing of the secondary particles (and thus contact loss between primary particles), as a difference for LNO materials with different secondary particle sizes would be expected due to shorter electronic conduction pathways into smaller cracked secondary particles. These considerations point to a kinetic limitation at a high degree of lithiation at the end-of-discharge as the decisive factor instead. The observed correlation of the reintercalatable Li with the interface area between CAM and electrolyte in the 1st cycle (see Fig. 9) thus seems to apply to the overall cycling behavior. Indeed, even after extended cycling, the amount of Li which can be reintercalated during discharge at a set C-rate still depends on the interface area between CAM and electrolyte. As the LNO secondary particle structure appears to completely fracture during the initial cycles (see Fig. 8), a very good correlation of the key electrochemical properties (i.e., 1st cycle capacity loss, capacity retention, impedance build-up) with the estimated primary particle SSA is thus found.

As already discussed above, DCIR measurements were performed at 50% SOC (referenced to the discharge capacity of the preceding C/10 cycle) to quantify the impedance build-up. At this degree of lithiation, kinetics do not have a severe impact, as the charge transfer resistance at intermediate SOCs is rather low for layered transition metal oxide CAMs.[37] Therefore, the resistance build-up will mirror other ohmic contributions, e.g., electrolyte salt depletion, formation of resistive degradation products on the CAM, SEI growth at the anode, etc. Zou et al. showed that the surface rearrangement of the layered cathode structure mostly happens at the CAM-to-electrolyte interface.[68] For LNO, where it was shown that particles thoroughly fracture during the initial cycles, samples with a larger primary particle size have a smaller interface area in contact with the electrolyte and therefore the mass fraction of the formed

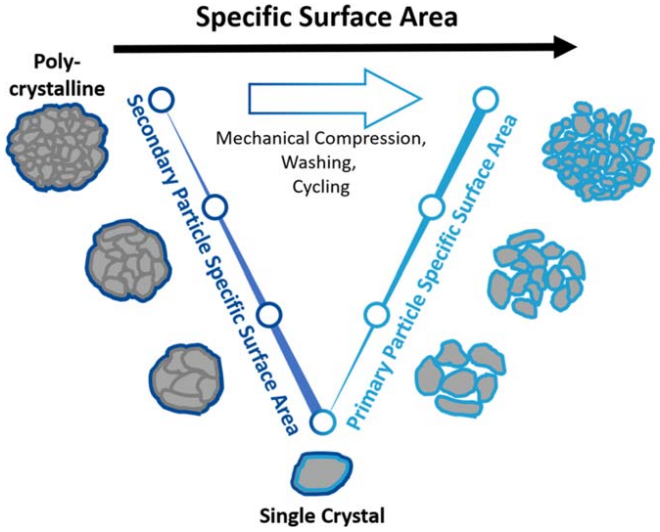

Figure 11. Schematic representation of the specific surface areas (SSAs) for different CAM morphologies. The left side represents the secondary, the right side the primary particle SSA that act as boundaries to the minimal/maximal accessible surface area of the CAM. By processes such as mechanical compression, washing and electrochemical cycling, the SSA increases by better accessibilty of the inner pore structure. For single crystal materials, both boundaries converge to a single value.

rock salt-like surface layer is less. The formation of this surface phase is accompanied by the evolution of gaseous species and further side reactions with the electrolyte would lead to a larger resistance increase.[47,48,69] However, by the deactivation of the H3 phase formation, the same amount of Li is lost independent of particle size. Thus, it can be explained why capacity retention and impedance build-up show inverse trends: samples with smaller primary particle sizes quickly develop larger surface areas, therefore showing a larger impedance increase, but at the same time reducing significantly the kinetic hindrance issue at low SOC. The latter effect thus dominates the performance of the here examined LNO/graphite full-cells, so that LNO samples with a large primary particle SSA (i.e., with small primary particles) have the best capacity retention despite a larger impedance build-up.

Implications for future materials design.—The observations from this study can be used to make predictions and recommendations for future cathode active material research. It was shown that the CAM-to-electrolyte interface area is the governing factor for the electrochemical performance of LNO and that this property changes during cycle-life. However, the CAM-to-electrolyte interface area was shown to also change due to LNO washing (see Table III), similar to what was shown for NCAs and NCMs upon washing and calendering.[23,59,70] In this study it has been found that for LNO CAMs after just a few cycles the interface area between LNO and electrolyte increases drastically towards the primary particle SSA, which seems to be more pronounced compared to mid-Ni materials if cycled under comparable cycling conditions (e.g. when cycled up to 4.3 V against Li^+/Li).

However, the extent of the interface area is always within the secondary particle and primary particle SSA limits, which represent the upper and lower boundary. These limits and the variations within these limits are schematically shown in Fig. 11. Secondary particle and primary particle size are material properties that are set by the precursor precipitation and the subsequent calcination processes. Current CAM research focusses on both polycrystalline and single crystalline morphology. Polycrystalline materials are characterized by large secondary particle agglomerates and by primary particles in the range of a few hundred nm. In contrast, single crystalline materials consist of monolithic primary particles that can have sizes

of a few μm and respresent single crystal domains. Moving from a polycrystalline material to its single crystalline counterpart, the secondary particle SSA increases, while the primary particle SSA decreases until they converge to a single value.

This leads to the conclusion that, depending on the cracking behavior, this transition to single crystalline morphology can increase or decrease the accessible surface area between CAM and electrolyte. For a mid-Ni material, e.g. NCM523, where cracking is assumed to be a minor issue, a single crystalline material can outperform the polycrystalline counterpart. However, for a Ni-rich material, where key electrochemical parameters correlate with the primary particle size due to particle cracking, a transition to single crystal materials induces a reduction in accessible surface area, which in turn leads to a reduction in achievable capacity due to the discussed kinetic limitations towards the end-of-discharge. In fact, it has been reported that cracking of cathode active materials is essential for their full utilization in a battery with a liquid electrolyte.[26,71] In contrast, for cells with a solid electrolyte, the interface between CAM and electrolyte cannot increase upon CAM fracturing, making the single crystal morphology interesting for that type of LIB, if a good contact between CAM and electrolyte can be maintained.[72,73]

Conclusions

LNO regained the attention of the battery community as a model system for Ni-rich cathode active materials. In part I of this study, the frequently suggested correlation between 1st cycle capacity loss and the amount of excess Ni in the Li layer could not be confirmed for small values of z in $Li_{1-z}Ni_{1+z}O_2$ (z ranging between 0.016–0.037). It was thus hypothesized that there might be a correlation with the particle morphology, which lead to the here presented in-depth study of the primary particle size distribution of differently synthesized LNOs by a top-view SEM image segmentation method that was validated against a manually conducted analysis. By means of krypton physisorption and laser scattering measurements of pristine and washed LNO powders, it could be shown that the SSAs of the LNO materials in their pristine state closely represented these of the secondary particles, while the SSAs of the washed LNO powders shifts towards (but does not reach) the specific surface area estimated for the fully separated primary particles.

Using in situ electrode capacitance measurements to characterize the CAM-to-electrolyte interface area during cycling, it was found that the primary particle specific surface area indeed determines the electrochemical performance of the synthesized LNO materials (i.e., the 1st cycle capacity loss, the cycling stability, and the impedance build-up). Particle fracturing and intrusion of the electrolyte into the pore structure lead to the convergence of this interface area towards the primary particle SSA. Although not shown in this publication, further influence of particle morphology on properties like gassing and transition metal dissolution is expected.

The main implication of this study is that the targeted design of cathode active materials cannot be performed without paying attention to particle morphology. The optimum morphology hereby depends on numerous factors, e.g., the chemical composition of the CAM, the cycling conditions, the electrode processing, the safety requirements, and the applied electrolyte. Furthermore, it must be emphasized that other material modifications in the form of doping and coating are likely to also have an impact on particle morphology, so that the latter must be considered when evaluating the intrinsic effects of dopings and coatings.

Acknowledgments

Cheuck Hin Ching and Louis Hartmann from the Chair of Technical Electrochemistry from the Technical University of Munich are gratefully acknowledged for the washing experiments and the krypton physisorption measurements. Phil Jack Holzmeister and Sebastian Michael Fritsch from the group Data Science for Chemicals from BASF SE are gratefully acknowledged for developing the image segmentation algorithm and their help with data processing.

ORCID

Felix Riewald https://orcid.org/0000-0001-9002-3633
Philipp Kurzhals https://orcid.org/0000-0002-7013-080X
Matteo Bianchini https://orcid.org/0000-0003-4034-7706
Jürgen Janek https://orcid.org/0000-0002-9221-4756
Hubert A. Gasteiger https://orcid.org/0000-0001-8199-8703

References

1. P. Kurzhals, F. Riewald, M. Bianchini, H. Sommer, H. A. Gasteiger, and J. Janek, *J. Electrochem. Soc.*, **168**, 110518 (2021).
2. A. Quinn, H. Moutinho, F. Usseglio-Viretta, A. Verma, K. Smith, M. Keyser, and D. P. Finegan, *Cell Reports Physical Science*, **1**, 100137 (2020).
3. S.-Y. Lee, G.-S. Park, C. Jung, D.-S. Ko, S.-Y. Park, H. G. Kim, S.-H. Hong, Y. Zhu, and M. Kim, *Adv. Sci.*, **6**, 1800843 (2019).
4. A. van Bommel and J. R. Dahn, *Chem. Mater.*, **21**, 1500 (2009).
5. P. Barai, Z. Feng, H. Kondo, and V. Srinivasan, *J. Phys. Chem. B*, **123**, 3291 (2019).
6. H. Dong and G. M. Koenig, *CrystEngComm*, **22**, 1514 (2020).
7. J. Zheng, P. Yan, L. Estevez, C. Wang, and J.-G. Zhang, *Nano Energy*, **49**, 538 (2018).
8. L. Zhang, X. Wang, T. Muta, D. Li, H. Noguchi, M. Yoshio, R. Ma, K. Takada, and T. Sasaki, *J. Power Sources*, **162**, 629 (2006).
9. Z. Xu, L. Xiao, F. Wang, K. Wu, L. Zhao, M.-R. Li, H.-L. Zhang, Q. Wu, and J. Wang, *J. Power Sources*, **248**, 180 (2014).
10. D. Li, Y. Sasaki, M. Kageyama, K. Kobayakawa, and Y. Sato, *J. Power Sources*, **148**, 85 (2005).
11. Y. Kim, *ACS Appl. Mater. Interfaces*, **4**, 2329 (2012).
12. G. Qian et al., *Energy Storage Mater.*, **27**, 140 (2020).
13. H.-H. Ryu, B. Namkoong, J.-H. Kim, I. Belharouak, C. S. Yoon, and Y.-K. Sun, *ACS Energy Lett.*, **6**, 2726 (2021).
14. J. Duan, C. Wu, Y. Cao, D. Huang, K. Du, Z. Peng, and G. Hu, *J. Alloys Compd.*, **695**, 91 (2017).
15. J. E. Harlow et al., *J. Electrochem. Soc.*, **166**, A3031 (2019).
16. H. H. Sun, H.-H. Ryu, U.-H. Kim, J. A. Weeks, A. Heller, Y.-K. Sun, and C. B. Mullins, *ACS Energy Lett.*, **5**, 1136 (2020).
17. G.-T. Park, N.-Y. Park, T.-C. Noh, B. Namkoong, H.-H. Ryu, J.-Y. Shin, T. Beierling, C. S. Yoon, and Y.-K. Sun, *Energy Environ. Sci.*, **14**, 5084 (2021).
18. U.-H. Kim, G.-T. Park, B.-K. Son, G. W. Nam, J. Liu, L.-Y. Kuo, P. Kaghazchi, C. S. Yoon, and Y.-K. Sun, *Nat. Energy*, **5**, 860 (2020).
19. A. Liu, N. Phattharasupakun, M. M. E. Cormier, E. Zsoldos, N. Zhang, E. Lyle, P. Arab, M. Sawangphruk, and J. R. Dahn, *J. Electrochem. Soc.*, **168**, 070503 (2021).
20. D. Pritzl, T. Teufl, A. T. S. Freiberg, B. Strehle, J. Sicklinger, H. Sommer, P. Hartmann, and H. A. Gasteiger, *J. Electrochem. Soc.*, **166**, A4056 (2019).
21. I. Hamam, N. Zhang, A. Liu, M. B. Johnson, and J. R. Dahn, *J. Electrochem. Soc.*, **167**, 130521 (2020).
22. W. M. Seong, Y. Kim, and A. Manthiram, *Chem. Mater.*, **32**, 9479 (2020).
23. S. Oswald, D. Pritzl, M. Wetjen, and H. A. Gasteiger, *J. Electrochem. Soc.*, **167**, 100511 (2020).
24. C. S. Yoon, D.-W. Jun, S.-T. Myung, and Y.-K. Sun, *ACS Energy Lett.*, **2**, 1150 (2017).
25. K. Dokko, M. Nishizawa, S. Horikoshi, T. Itoh, M. Mohamedi, and I. Uchida, *Electrochem. Solid-State Lett.*, **3**, 125 (2000).
26. R. Ruess, S. Schweidler, H. Hemmelmann, G. Conforto, A. Bielefeld, D. A. Weber, J. Sann, M. T. Elm, and J. Janek, *J. Electrochem. Soc.*, **167**, 100532 (2020).
27. O. Ronneberger, P. Fischer, and T. Brox, *Medical Image Computing and Computer-Assisted Intervention—MICCAI 2015*, ed. N. Navab, J. Hornegger, W. M. Wells, and A. F. Frangi (Springer, Cham) 234 (2015).
28. M. D. Abràmoff, P. J. Magalhães, and S. J. Ram, *Biophotonics international*, **11**, 36 (2004).
29. C. A. Schneider, W. S. Rasband, and K. W. Eliceiri, *Nat. Methods*, **9**, 671 (2012).
30. S. Oswald, F. Riewald, and H. A. Gasteiger, In Press.
31. Z. Chen, X. Liu, J. Yang, E. Little, and Y. Zhou, *Comput. Geosci.*, **138**, 104450 (2020).
32. B. Rühle, J. F. Krumrey, and V.-D. Hodoroaba, *Sci. Rep.*, **11**, 4942 (2021).
33. D. D. Eberl, J. Środoń, M. Kralik, B. E. Taylor, and Z. E. Peterman, *Science*, **248**, 474 (1990).
34. S. R. Challa, A. T. Delariva, T. W. Hansen, S. Helveg, J. Sehested, P. L. Hansen, F. Garzon, and A. K. Datye, *J. Am. Chem. Soc.*, **133**, 20672 (2011).
35. P. J. Ferreira, G. J. La O', Y. Shao-Horn, D. Morgan, R. Makharia, S. Kocha, and H. A. Gasteiger, *J. Electrochem. Soc.*, **152**, A2256 (2005).
36. M. Thommes, K. Kaneko, A. V. Neimark, J. P. Olivier, F. Rodriguez-Reinoso, J. Rouquerol, and K. S. W. Sing, *Pure Appl. Chem.*, **87**, 1051 (2015).
37. F. Friedrich, B. Strehle, A. T. S. Freiberg, K. Kleiner, S. J. Day, C. Erk, M. Piana, and H. A. Gasteiger, *J. Electrochem. Soc.*, **166**, A3760 (2019).
38. J.-H. Kim, H.-H. Ryu, S. J. Kim, C. S. Yoon, and Y.-K. Sun, *ACS Appl. Mater. Interfaces*, **11**, 30936 (2019).
39. S. Schweidler, L. de Biasi, G. Garcia, A. Mazilkin, P. Hartmann, T. Brezesinski, and J. Janek, *ACS Appl. Energy Mater.*, **2**, 7375 (2019).
40. H.-H. Ryu, K.-J. Park, C. S. Yoon, and Y.-K. Sun, *Chem. Mater.*, **30**, 1155 (2018).
41. K.-J. Park, J.-Y. Hwang, H.-H. Ryu, F. Maglia, S.-J. Kim, P. Lamp, C. S. Yoon, and Y.-K. Sun, *ACS Energy Lett.*, **4**, 1394 (2019).

42. L. de Biasi, A. Schiele, M. Roca-Ayats, G. Garcia, T. Brezesinski, P. Hartmann, and J. Janek, *ChemSusChem*, **12**, 2240 (2019).
43. J.-H. Kim, K.-J. Park, S. J. Kim, C. S. Yoon, and Y.-K. Sun, *J. Mater. Chem. A*, **7**, 2694 (2019).
44. L. de Biasi, A. O. Kondrakov, H. Geßwein, T. Brezesinski, P. Hartmann, and J. Janek, *The Journal of Physical Chemistry C*, **121**, 26163 (2017).
45. J. Kasnatscheew et al., *Phys. Chem. Chem. Phys.*, **18**, 3956 (2016).
46. A. Grenier, P. J. Reeves, H. Liu, I. D. Seymour, K. Märker, K. M. Wiaderek, P. J. Chupas, C. P. Grey, and K. W. Chapman, *J. Am. Chem. Soc.*, **142**, 7001 (2020).
47. R. Jung, M. Metzger, F. Maglia, C. Stinner, and H. A. Gasteiger, *The Journal of Physical Chemistry Letters*, **8**, 4820 (2017).
48. R. Jung, M. Metzger, F. Maglia, C. Stinner, and H. A. Gasteiger, *J. Electrochem. Soc.*, **164**, A1361 (2017).
49. F. Schipper, H. Bouzaglo, M. Dixit, E. Erickson M., T. Weigel, M. Talianker, J. Grinblat, L. Burstein, M. Schmidt, J. Lampert, C. Erk, B. Markovsky, D. Major T., and D. Aurbach, *Adv. Energy Mater.*, **8**, 1701682 (2017).
50. B. Song, W. Li, S.-M. Oh, and A. Manthiram, *ACS Appl. Mater. Interfaces*, **9**, 9718 (2017).
51. R. Jung, R. Morasch, P. Karayaylali, K. Phillips, F. Maglia, C. Stinner, Y. Shao-Horn, and H. A. Gasteiger, *J. Electrochem. Soc.*, **165**, A132 (2018).
52. J. Li and A. Manthiram, *Adv. Energy Mater.*, **0**, 1902731 (2019).
53. H.-H. Ryu, G.-T. Park, C. S. Yoon, and Y.-K. Sun, *J. Mater. Chem. A*, **7**, 18580 (2019).
54. F. Wu et al., *Nano Energy*, **59**, 50 (2019).
55. S. Xu, X. Wang, W. Zhang, K. Xu, X. Zhou, Y. Zhang, H. Wang, and J. Zhao, *Solid State Ionics*, **334**, 105 (2019).
56. H. Ronduda, M. Zybert, A. Szczęsna-Chrzan, T. Trzeciak, A. Ostrowski, D. Szymański, W. Wieczorek, W. Raróg-Pilecka, and M. Marcinek, *Nanomaterials*, **10**, 1 (2020).
57. A. Mesnier and A. Manthiram, *ACS Appl. Mater. Interfaces*, **12**, 52826 (2020).
58. J. Kasnatscheew, M. Evertz, B. Streipert, R. Wagner, S. Nowak, I. Cekic Laskovic, and M. Winter, *The Journal of Physical Chemistry C*, **121**, 1521 (2017).
59. B. Strehle, F. Friedrich, and H. A. Gasteiger, *J. Electrochem. Soc.*, **168**, 050512 (2021).
60. R. Weber, A. J. Louli, K. P. Plucknett, and J. R. Dahn, *J. Electrochem. Soc.*, **166**, A1779 (2019).
61. R. Fathi, J. C. Burns, D. A. Stevens, H. Ye, C. Hu, G. Jain, E. Scott, C. Schmidt, and J. R. Dahn, *J. Electrochem. Soc.*, **161**, A1572 (2014).
62. M. Safari and C. Delacourt, *J. Electrochem. Soc.*, **158**, A1123 (2011).
63. C. Xu et al., *Nat. Mater.*, **20**, 84 (2021).
64. S. Schweidler, L. de Biasi, P. Hartmann, T. Brezesinski, and J. Janek, *ACS Appl. Energy Mater.*, **3**, 2821 (2020).
65. J. Xu, E. Hu, D. Nordlund, A. Mehta, S. N. Ehrlich, X.-Q. Yang, and W. Tong, *ACS Appl. Mater. Interfaces*, **8**, 31677 (2016).
66. B. Strehle, K. Kleiner, R. Jung, F. Chesneau, M. Mendez, H. A. Gasteiger, and M. Piana, *J. Electrochem. Soc.*, **164**, A400 (2017).
67. M. Mock, M. Bianchini, F. Fauth, K. Albe, and S. Sicolo, *J. Mater. Chem. A*, **9**, 14928 (2021).
68. L. Zou, W. Zhao, H. Jia, J. Zheng, L. Li, D. P. Abraham, G. Chen, J. R. Croy, J.-G. Zhang, and C. Wang, *Chem. Mater.*, **32**, 2884 (2020).
69. D. Leanza, M. Mirolo, C. A. F. Vaz, P. Novák, and M. EL Kazzi, *Batteries & Supercaps*, **2**, 482 (2019).
70. R. Sim, S. Lee, W. Li, and A. Manthiram, *ACS Appl. Mater. Interfaces*, **13**, 42898 (2021).
71. E. Trevisanello, R. Ruess, G. Conforto, F. H. Richter, and J. Janek, *Adv. Energy Mater.*, **11**, 2003400 (2021).
72. G. Conforto, R. Ruess, D. Schröder, E. Trevisanello, R. Fantin, F. H. Richter, and J. Janek, *J. Electrochem. Soc.*, **168**, 070546 (2021).
73. C. Wang et al., *Energy Storage Mater.*, **30**, 98 (2020).

3.3 Publication 3:

Deeper Understanding of the Lithiation Reaction during the Synthesis of $LiNiO_2$ Towards an Increased Production Throughput

The third publication of this thesis investigated an alternative two-stage calcination concept, which separates the process into a „partial-lithiation“ step at moderate temperature, where all chemical reactions are taken together, and a sintering step at high temperature to form the final crystal structure and to grow the crystallites.
The pathway of the lithiation reaction between $Ni(OH)_2$ and LiOH monohydrate during LNO synthesis was recapitulated with the aid of thermogravimetry and differential thermal analysis. Two furnace designs were investigated for the partial-lithiation step and a variation of temperature and dwell time was performed for the best suited option. The partially-lithiated samples were analyzed in great detail by a variety of methods in order to get a better understanding of the lithiation reaction. Afterwards, the partially-lithiated materials were subjected to a second treatment at high temperature to obtain electrochemically active LNO samples. The comparison with a reference sample prepared by a conventional calcination showed that the two-stage process resulted in materials having similar physicochemical and electrochemical properties. However, the process including the partial-lithiation step would result in a significant increase of production throughput and it is thus considered worthwhile to implement it in future CAM manufacturing plants.

The publication was written by the author and edited by the co-authors. The experiments were planned by the author and H. Sommer. The rotary kiln experiments were done by the author and D. Sander from BASF SE group Calcination and Combustion with a setup developed by A.M. Kern. The calcination trials with the box-type furnaces were performed by the author. The powder XRD experiments were performed by F. Fauth and the BL04-MSPD beamline team at the ALBA synchrotron and the Rietveld refinement was done by the author and M. Bianchini. The SEM imaging and electrochemical testing were performed by the author. The thermogravimetry and differential thermal analysis, the inductively coupled plasma optical emission spectrometry, acid titration and iodometric titration measurements were done by the Analytics Competence Centre at BASF SE and were evaluated by the author. The X-ray photoelectron spectroscopy experiments were performed and evaluated by F. Walther. The transmission electron microscopy measurements were done and analyzed by S. Ahmed.

P. Kurzhals, F. Riewald, M. Bianchini, S. Ahmed, A.M. Kern, F. Walther, H. Sommer,

K. Volz, J. Janek, *Deeper Understanding of the Lithiation Reaction during the Synthesis of* $LiNiO_2$ *Towards an Increased Production Throughput*, Journal of the Electrochemical Society **169**, 50526 (2022)

Journal of The Electrochemical Society, 2022 **169** 050526

Deeper Understanding of the Lithiation Reaction during the Synthesis of $LiNiO_2$ Towards an Increased Production Throughput

Philipp Kurzhals,[1,2,z] Felix Riewald,[1,3] Matteo Bianchini,[1,4,5,*] Shamail Ahmed,[6] Andreas Michael Kern,[1] Felix Walther,[2] Heino Sommer,[7] Kerstin Volz,[6] and Jürgen Janek[2,5,*,z]

[1]*BASF SE, New Battery Materials and Systems, D-67056 Ludwigshafen, Germany*
[2]*Institute of Physical Chemistry & Center for Materials Research, Justus Liebig University, D-35392 Giessen, Germany*
[3]*Technical Electrochemistry, Department of Chemistry and Catalysis Research Center, Technical University of Munich, D-85748 Garching, Germany*
[4]*Inorganic active materials for electrochemical energy storage systems, Faculty of Biology, Chemistry and Geosciences, Bavarian Center for Battery Technology (Baybatt), University of Bayreuth, Universitätsstraße 30, D-95447 Bayreuth, Germany*
[5]*Battery and Electrochemistry Laboratory (BELLA), Institute of Nanotechnology, Karlsruhe Institute of Technology (KIT), 76344 Eggenstein-Leopoldshafen, Germany*
[6]*Materials Science Centre and Faculty of Physics, Philipps University Marburg, D-35043 Marburg, Germany*
[7]*Cell Force Group, D-72072 Tübingen, Germany*

Efficient manufacturing of cathode active materials (CAMs) for Li-ion batteries is one key target on the roadmap towards cost reduction and improved sustainability. This work deals with a two-stage calcination process for the synthesis of $LiNiO_2$ (LNO) consisting of a (partial) lithiation step at moderate temperatures and short dwell times and a subsequent high temperature crystallization to decouple the chemical reactions and crystal growth. The use of an agitated-bed lithiation using the rotational movement of a rotary kiln setup shows beneficial effects compared to its fixed-bed counterpart in a crucible as the lithiation reaction is faster under otherwise comparable conditions. The temperature profile for the agitated-bed process was further optimized to avoid the presence of needle-like LiOH residuals in the intermediate product indicative of an incomplete reaction. The partially-lithiated samples were subjected to a second calcination step at a maximum calcination temperature of 700 °C and afterwards revealed comparable physico-chemical properties and electrochemical behavior compared to a reference sample made by a standard one-stage calcination. In a simplified model calculation, the proposed calcination concept leads to an increase in throughput by a factor of $\sim$ 3 and thus could embody an important lever for the efficiency of future CAM production.
 [DOI: 10.1149/1945-7111/ac6c0b]

Manuscript submitted March 21, 2022; revised manuscript received April 25, 2022. Published May 19, 2022.

Supplementary material for this article is available online

The increasing demand for Li-ion batteries (LIBs), especially for the battery electric vehicle (BEV) market, calls for solutions with higher energy densities, improved safety and reduced costs. In recent years, layered transition metal oxides with the composition $Li(Ni_{1-x-y}Co_xMn_y)O_2$ (NCM) or $Li(Ni_{1-x-y}Co_xAl_y)O_2$ (NCA) were established as the predominant choice as cathode active material (CAM) for BEVs, as they fullfill most requirements, especially when the Ni content is increased concomitant with a reduction of the Co content.[1,2] However, BEVs still have not reached full cost competitiveness with cars powered by combustion engines. This can be attributed to a large extent to the CAM, which accounts for a substantial share of the overall cell costs.[3,4] As raw material prices have shown a significant increase and the transition towards renewable energy generation has not yet been accomplished,[5–7] increasing production throughput and the search for cheap and sustainable processes are both essential for economically feasible CAM manufacturing.

In a conventional production process for NCM and NCA materials, a mixture of a transition metal hydroxide precursor and a Li source is filled into ceramic vessels, referred to as "saggers," which are then passed through a roller hearth kiln (RHK).[8–11] The mixture passes the hot zones of the furnace, which either leads to a continuous heating or includes holding steps at fixed intermediate temperatures. Finally, the mixture is heated to a maximum calcination temperature T_{max} for a certain dwell time for proper crystallization and crystallite growth.

$LiOH{\cdot}H_2O$ is preferred as Li source compared to other alternatives, e.g. Li_2CO_3, due to its lower melting point at $T_{melt} \sim 460$ °C and less formation of lithium-containing residual salts after calcination, which is an issue especially for CAMs with an increased Ni content.[12–14] However, heating of $LiOH{\cdot}H_2O$ and the transition metal hydroxide precursor leads to the evolution of H_2O vapor and therefore limits calcination throughput because $\sim$ 30 wt% of the initial mixture is lost. Furthermore, the volatile H_2O can cause demixing of the precursor and the Li source, potentially leading to inhomogeneities in the chemical composition of the final product.[15] As with many heterogeneous reactions, limitations by heat and mass transfer are likely to occur, leading to different temperatures and gas concentrations in different parts of the powder bed, varying lithiation progress in the course of the calcination and finally varying physical properties in the CAM powder. High sagger loadings and short reaction times, which are preferred to reduce manufacturing costs, are expected to increase these detrimental effects.

To overcome these problems, an alternative production concept with a two-stage process was proposed, which includes a "pre-calcination" step of the Li source and the precursor in a rotary calciner (a metal or ceramic tube) at an intermediate temperature of up to 750 °C and a second "high temperature calcination" step performed with a rotary calciner or a box furnace.[16] The inventors claim that the final product of this process starting from $Ni_{0.333}Co_{0.333}Mn_{0.333}O_x(OH)_y$ and Li_2CO_3 has an identical crystal structure compared to materials prepared with the standard one-stage route and that it may display an improved product homogeneity, but without providing further analytical results or data on the electrochemical performance. Other authors claim a split firing method, where in a first step at a moderate temperature (650 °C–850 °C) a Li-deficient intermediate product (0.65–0.94 Li equivalents per mol of

*Electrochemical Society Member.
[z]E-mail: philipp.kurzhals@basf.com; juergen.janek@pc.jlug.de

transition metal) is formed, mixed with additional Li source to obtain the target Li equivalents and sintered in a second step.[15] For the first step, a metallic rotary kiln was applied to improve the product homogeneity as well as the temperature distribution during the reaction.

Moreover, in a recent in situ study on the synthesis of LNO it was found that significant lithium uptake into rock-salt type NiO occurred even at moderate temperatures (350 °C and a dwell time of 12 h), which was suggested to be beneficial for the crystallization of the material.[17]

Several research groups have started to use a holding step close to 500 °C for several hours, sometimes accompanied by an intermediate grinding step, before heating up to the maximum temperature for the calcination of their LNO samples.[18–20]

So far, mostly patents have dealt with the potential benefits of separating the chemical reactions during a "partial-lithiation" step at moderate temperatures and the formation of the final crystal structure concomitant with crystallite growth during a sintering step at high temperatures, which also means that the used temperatures and dwell times are described rather unspecifically and that the amount and the completeness of the provided data are quite limited.

Thus, in this study we intend to generate a deeper understanding of the lithiation mechanism itself and whether a two-stage calcination process including a partial-lithiation step can be used to synthesize CAM with comparable properties when benchmarked against a conventional one-stage calcination protocol.

The study is run exemplarily with $LiNiO_2$ as the 100% Ni end member of the NCM and NCA cathode solid solutions. At first, we revisit the occurring chemical reactions via thermogravimetric and differential thermal analysis, starting from the precursors $Ni(OH)_2$ and $LiOH{\cdot}H_2O$. Afterwards, partial-lithiation experiments are performed under agitated-bed conditions using a rotary kiln and compared to the fixed-bed reaction in a box furnace, by use of two different Li stoichiometries, a temperature of 500 °C and a dwell time of one hour. Furthermore, the influence of the partial-lithiation temperature and dwell time on the lithiation progress are pointed out for the agitated-bed furnace concept. Then, CAMs are prepared in a second "main calcination" step and the physico-chemical properties as well as electrochemical behavior are compared to a reference material calcined via a standard one-stage process. Finally, benefits and remaining challenges of the two-stage calcination concept are discussed.

Experimental

Calcination of $LiNiO_2$ using a partial-lithiation step.—LNO samples were calcined through a solid-state synthesis route starting from the base materials $Ni(OH)_2$ and $LiOH{\cdot}H_2O$. A commercial monodisperse $Ni(OH)_2$ precursor (Hunan Zoomwe Zhengyuan Advanced Material Trade Co., Ltd.) with a narrow secondary particle size distribution (d_{50} = 10 μm with a span of 0.8 μm) was utilized. $LiOH{\cdot}H_2O$ was used as Li source (Albemarle Corporation), which was ground prior to the synthesis with an air classifying mill to obtain particles with a size of ~10–20 μm. 50 g of $Ni(OH)_2$ were mixed with either 80% or 100% of the amount of Li source that is required to obtain 1.01 Li equivalents per mol of Ni using a laboratory blender (Kinematica AG). For the fixed-bed partial-lithiation, 60 g of the mixture were filled into an alumina crucible and put into a box furnace (Linn High Therm GmbH). For the agitated-bed partial-lithiation, the same sample amount was put into a metal bulb, which was then attached to a rotary evaporator (Büchi Labortechnik AG) and heated inside an electrical dome-shaped furnace (Horst GmbH).

A schematic of the used calcination profiles is depicted in Fig. 1a. A "one-step reference" sample was prepared by heating the mixture of $Ni(OH)_2$ and $LiOH{\cdot}H_2O$ (1.01 Li equivalents per mol of Ni) using a crucible and a box furnace with a ramp of R_1 = 3 °C min^{-1} to T_1 = 400 °C and a dwell time t_1 = 4 h, followed by heating with the same ramp to T_2 = 700 °C and a dwell time of t_2 = 6 h. The experiment was run in pure oxygen atmosphere (flow rate of 100 liters per hour, corresponding to about ten furnace-volume exchanges per hour).

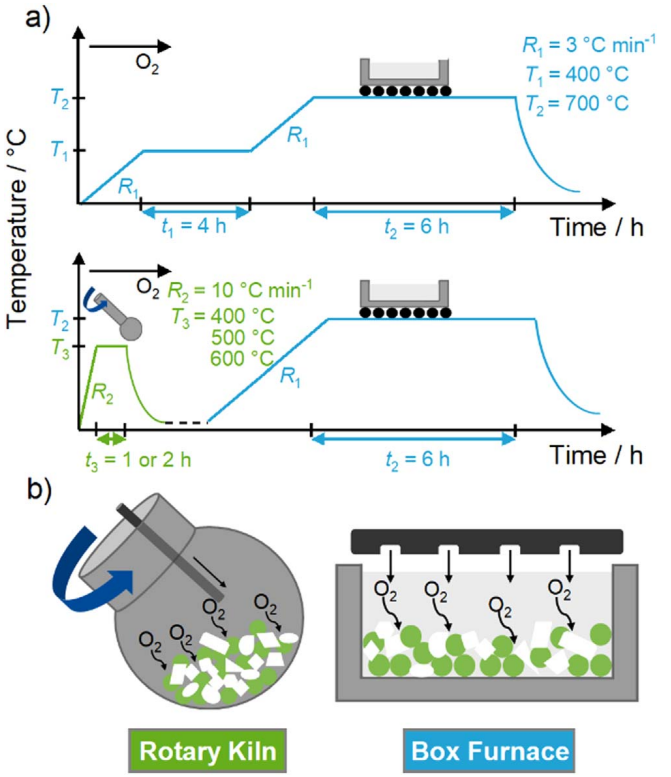

Figure 1. Overview of the experimental conditions and the setup of this study. (a) Top: Typical calcination profile used in industry with one temperature hold at T_1 for a time t_1 and a second temperature hold at $T_2 > T_1$ for a time t_2 and with a heating ramp R_1. Bottom: Calcination profile including a partial-lithiation step using a heating ramp $R_2 > R_1$ and a temperature hold at $T_3 \approx T_1$ for a time $t_3 < t_1$. After cooling, the partially-lithiated powders were heated with a heating ramp R_1 to a temperature $T_2 > T_3$ and a hold for a time t_2 is applied. (b) The two furnace designs, which were used for the partial-lithiation step: a rotary kiln with a metal bulb (left) and a crucible within a box furnace (right).

For sample preparation including the partial-lithiation step, the mixture of $Ni(OH)_2$ and $LiOH{\cdot}H_2O$ was heated with R_2 = 10 °C min^{-1} to a temperature T_3 = 400 °C, 500 °C or 600 °C and a dwell time t_3 = 1 h or 2 h. Figure 1b shows schematics of the furnace designs used for the partial-lithiation step. All experiments were run in pure oxygen atmosphere with a flow rate of 100 liters per hour for the box furnace (~ ten furnace-volume exchanges per hour) and 60 liters per hour for the rotary kiln (~ thirty furnace-volume exchanges per hour). The rotary kiln was operated with a rotational speed of 20 revolutions per minute.

The partially-lithiated samples were removed from either the metal bulb or the crucible and analyzed by inductively coupled plasma optical emission spectrometry (ICP-OES) to determine the amounts of Li and Ni. Afterwards, the samples were mixed with the required amount of $LiOH{\cdot}H_2O$ to obtain 1.01 Li equivalents per mol of Ni in the final product and subjected to a main calcination step using a crucible and the box furnace. For this purpose, the mixtures were heated with R_1 = 3 °C min^{-1} to T_2 = 700 °C and a dwell time t_2 = 6 h. After the holding step at T_2, all samples were cooled down to 120 °C and brought to a dry room (21 °C, dew point < −40 °C) inside a gas-tight box to prevent reactions with ambient moisture and CO_2. If not specified otherwise, all further powder processing was performed under dry room conditions. Prior to characterization of the materials and electrode preparation, the powders were sieved using sieves with a mesh size of 32 μm (Retsch GmbH).

Thermogravimetric—differential thermal analysis (TG-DTA).— $Ni(OH)_2$, $LiOH{\cdot}H_2O$ and the mixture of both with 1.01 Li equivalents per mol of Ni were investigated using a TG-DTA device (STA 449 F1 Jupiter, Netzsch-Gerätebau GmbH). Measurements were performed under oxygen enriched atmosphere with an O_2 flow rate of 95 ml min^{-1} and 5 ml min^{-1} of synthetic air (furnace volume $\sim$ 100 ml). For each experiment, $\sim$ 60 mg of the sample were filled into a ceramic crucible (Al_2O_3, 0.9 ml volume) and heated with 10 °C min^{-1} to 500 °C, where the temperature was held for one hour. One additional measurement was made with the mixture of $Ni(OH)_2$ and $LiOH{\cdot}H_2O$ heated with the same ramp to 600 °C and a dwell time of one hour.

Inductively coupled plasma optical emission spectrometry (ICP-OES).—Li and Ni contents of the samples after each calcination step were determined by ICP-OES. For this purpose, a small amount of sample ($\sim$ 0.3 g) was dispersed in 5 M aqueous HCl solution. The mixture was stirred and slightly heated until the solid powder was completely dissolved. Afterwards, the mixture was cooled down and diluted with deionized H_2O, until a concentration of 0.5 M HCl was reached. Finally, the concentrations of the elements Li and Ni were measured with the ICP-OES device (5100, Agilent Technologies, Inc.).

Acid titration.—To evaluate the amount of lithium-containing residual salts in form of LiOH and Li_2CO_3 after the partial-lithiation step as well as after the main calcination, the samples were investigated using acid titration. For this purpose, 2 g of intermediate sample or CAM were mixed with 10 g of deionized H_2O and stirred for 20 min in a glovebox under N_2 atmosphere. Then, the sample/H_2O dispersion was filtered using a syringe filter and the filtrate was titrated using an automatic titrator (Titrando 808, Deutsche Metrohm GmbH & Co. KG) and 0.1 M HCl as a standard solution (analytical grade, Bernd Kraft GmbH). The change of the pH value was monitored using a glass electrode (Metrohm). LiOH and Li_2CO_3 were distinguished by the two distinct equivalent points in the titration curve. The first equivalent point thereby corresponds to the protonation of the hydroxide and carbonate ions, whereas the second equivalent point equals the protonation of the hydrogen carbonate ions, thus making the differentiation of the two salt concentrations possible. The weight fractions of "soluble Li" species were calculated by multiplying the weight fractions of LiOH and Li_2CO_3 with the respective Li stoichiometries and the molar mass of Li, dividing by the respective molar masses and finally adding both contributions.

Iodometric titration.—The average Ni oxidation states of the samples after the partial-lithiation step and after the main calcination were determined by iodometric titration. For this purpose, a small amount of sample ($\sim$ 0.3 g) was dispersed in a 20 wt% HCl solution and the mixture was heated to evaporate into a receiver containing a 10 wt% KI solution. Subsequently, the Ni^{3+} ions were reduced to Ni^{2+} concomitant with the oxidation of I^- to I_2. The resulting iodine was titrated using a 0.1 M $Na_2S_2O_3$ solution. From the consumption of the thiosulfate solution, the amount of substance of Ni^{3+} was calculated and compared to the total amount of substance of Ni measured by ICP-OES to determine the average oxidation state of Ni.

Scanning electron microscopy (SEM) imaging.—For top view images, a small amount of cathode powder was fixed on a SEM pin holder (Agar Scientific, Ltd.) covered with conducting carbon cement (Plano GmbH). A 6 nm thick platinum layer was added by sputter deposition (SCD 500 Sputter Coater, Bal-Tec AG). Measurements were performed using a SEM with a thermal field emission cathode and an Everhart-Thornley secondary electron detector at an operating voltage of 5 kV (Ultra 55, Carl Zeiss AG). Samples for cross section measurements were prepared by initially mixing 2 g of epoxy resin and 0.5 g of epoxy hardener (Buehler, ITW Test & Measurement GmbH) and adding a few drops of the mixture to a small amount of cathode powder in a gelatine capsule, followed by 2 min of mixing with a spatula. Afterwards, the slurries were cast onto an Al-foil using a manual coater with a gap size of 0.5 mm and dried in an oven (Heraeus Holding GmbH) at 40 °C over night. Smaller sections were prepared with a scalpel, mounted on a customized mask and aligned with an optical microscope. Then, the samples were transferred to an ion milling system (ArBlade 5000, Hitachi, Ltd.) and cross sections were prepared by milling with an Ar ion beam at an operating voltage of 6 kV for two hours. Images were taken as described above for the top view measurements.

Image segmentation.—An automated SEM image segmentation method was used to quantify the primary particle size distribution of the CAMs. Details on the algorithm and the criteria, that were used for primary particle segmentation, were published in a recent report.[21] The size of a primary particle was quantified by taking the area of the particle after segmentation and calculating the diameter of a circle with the same area ("equivalent diameter"). Ten top view SEM images in 20 k magnification were measured for each CAM after the main calcination to have a sufficient amount of particles for proper statistical evaluation. More than 1000 primary particles per sample were analyzed.

Powder X-ray diffraction.—Synchrotron powder X-ray diffraction (PXRD) measurements were performed at the ALBA synchrotron. The measurements at ALBA were carried out at the BL04-MSPD beamline at a wavelength of $\lambda = 0.62001$ Å (calibrated using a Si NIST standard) using a Si 111 monochromator and the MYTHEN II position sensitive detector in 2θ angular range of 2° −82°. The LNO samples were filled in borosilicate capillaries of 0.7 mm diameter, sealed by flame, and mounted on a spinning sample holder. Data were collected in Debye–Scherrer geometry for 27 different positions of the detector, and a long data acquisition time of 30 s was chosen for each position in order to obtain high intensity patterns. For the partially-lithiated samples, the angular positions of impurity phases were compared to the calculated diffraction patterns of LiOH and Li_2CO_3 and the relative peak intensities will be discussed qualitatively.

Rietveld refinement was done using the Fullprof software package. For each sample a new background for the measured diffraction pattern was determined with the WinPLOTR software and corrected by visual inspection. The refinements were based on a hexagonal α-$NaFeO_2$ structure with the $R-3m$ space group. The instrumental broadening was determined by measuring a NAC ($Na_2Ca_3Al_2F_{14}$) standard in the same sample configuration. The model used for the fitting is based on Thompson-Cox-Hastings pseudo-Voigt convoluted with axial divergence asymmetry functions. Refinement of the parameters of the structural model was done for consecutive iteration cycles until convergence was reached and the quality of the fit was checked by inspection of R_{wp} (weighted profile factor with all non-excluded points) and R_{Bragg} (Bragg R-factor) as well as χ^2 (reduced chi-square). Two different structural models were used for the refinement.

For the first model in the final iteration step 12 parameters were refined: scale factor, zero shift, a and c unit cell parameters, U, X, Y as parameters of the Gaussian (U) and Lorentzian (X, Y) contribution to the pseudo-Voigt function, fractional atomic coordinate of oxygen z_{ox}, occupancy of Ni on Li site (assuming site remains fully occupied), B_{iso} (isotropic displacement parameter) of O, Ni and of Li. According to the recent report of Yin et al., Li and O were treated using the ionic form factors while the atomic form factor was applied for Ni, which was shown to be reasonable in our recent report on a large set of $LiNiO_2$ samples.[22]

The second model takes anisotropic size effects into account by using additional parameters. In this case, the Lorentzian part of the peak broadening is modeled with linear combinations of spherical

harmonics (Y_{00}, Y_{20}, Y_{40}, Y_{43-}, Y_{60}, Y_{63+} and Y_{66+}) as discussed in the report of Casas-Cabanas et al. on the microstructure of $Ni(OH)_2$.[23]

X-ray photoelectron spectroscopy (XPS).—XPS analyses were performed for the $Ni(OH)_2$ precursor, for the partially-lithiated sample with 1.01 Li equivalents per mol of Ni, that was subjected to 500 °C and a dwell time of one hour in the rotary kiln, and the respective partially-lithiated sample with an increased temperature of 600 °C. All samples were prepared in an Ar-filled glovebox. The powders were compacted in Teflon cups, which were then attached to the sample holder with non-conductive adhesive tape. The samples were transferred under an Ar atmosphere from the glovebox into the XPS instrument (PHI5000 Versa Probe II, Physical Electronics Inc.) using a transfer vessel for PTS holders by PREVAC. For the analysis, monochromatic Al Kα radiation was used (1486.6 eV). The power of the X-ray source was 50 W and the beam voltage was 17 kV. The diameter of the beam was 200 μm. The pass energy of the analyzer was set to 46.95 eV for all detail spectra. A dual-beam charge neutralization was applied during the measurements. For data evaluation, all spectra were calibrated in relation to the signal of adventitious carbon at 284.8 eV.

Transmission electron microscopy (TEM).—TEM samples were prepared using a focused ion beam—scanning electron microscopy (FIB-SEM) system (JIB-4601F, JEOL GmbH). The samples were first coated with a thin layer of Pt ($\sim$ 100 nm) using a sputter coater prior to loading them to the FIB-SEM to avoid any damage from the electron and the Ga-ion beam. The selected particles were then further protected by first depositing the carbon layer and then tungsten layers using a Ga-ion beam. The sample was first thinned with a 30 kV Ga-ion beam to around 500 nm thickness and then further thinned with a 5 kV Ga-ion beam.

Images and scanning-precession electron diffraction data (SPED) were taken with a TEM (JEM 3010, JEOL GmbH) equipped with the ASTAR system (NanoMEGAS SPRL). The microscope was operated at 300 kV. The SPED 4D datasets were taken under low-dose conditions, i.e., by selecting the smallest condenser lens aperture and the lowest current possible at this microscope. The dataset was taken with a step size of 15 nm, with the beam having a probe size of around 11 nm. A precession angle of 0.25 degrees was used and the PED patterns were analyzed using ASTAR's indexing software.[24,25] For this purpose, first, a library of simulated diffraction patterns from the candidate phases LiOH, Li_2O, and Li_2CO_3 were produced in different orientations. The best matches from the simulated data were found using template matching, which are illustrated in Fig. S6 (available online at stacks.iop.org/JES/169/050526/mmedia) (supplementary information).

Electrochemical characterization.—Electrodes for electrochemical characterization were prepared by mixing the CAM powders with conductive carbon (C65, Imerys Graphite & Carbon) and PVDF binder (Solef 5130, Solvay GmbH) in a 94:3:3 mass ratio. For this, a 7.5 wt% binder solution in N-methyl-2-pyrrolidone (NMP,

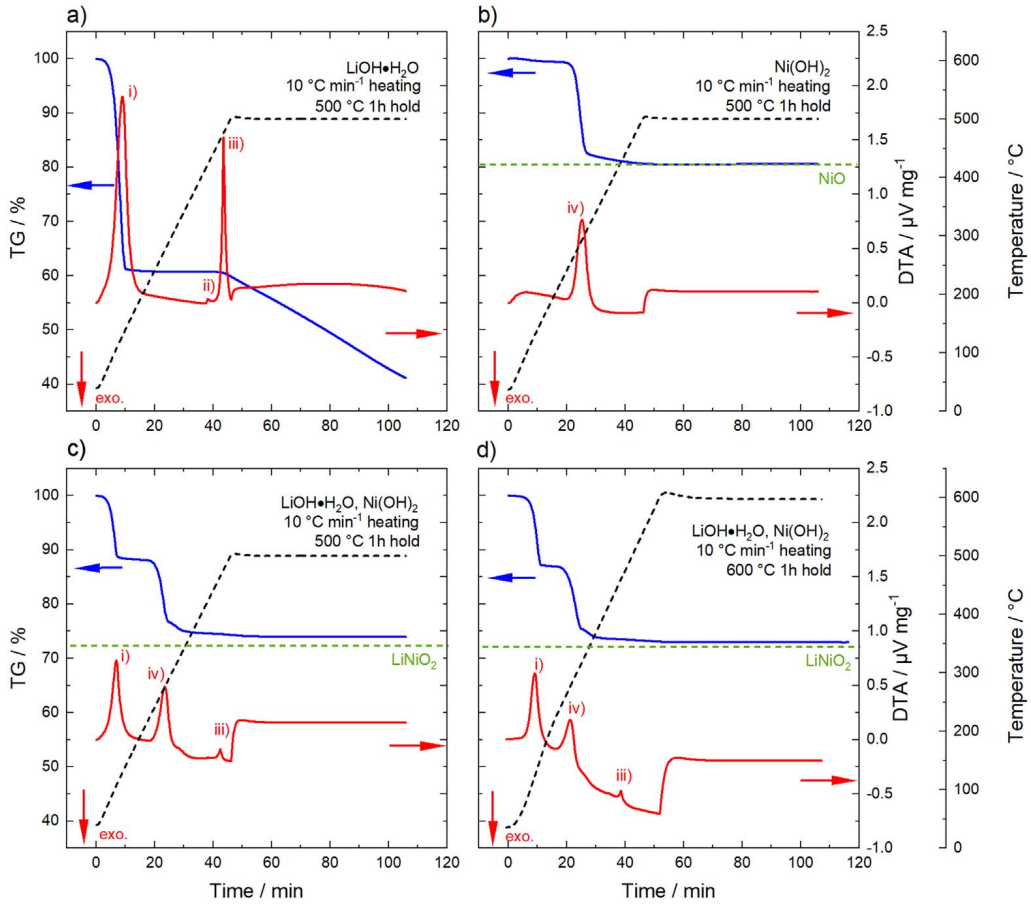

Figure 2. TG-DTA measurements illustrating the chemical reactions that occur during lithiation. (a) $LiOH{\cdot}H_2O$ heated with 10 °C min^{-1} to 500 °C with a dwell time of one hour, (b) $Ni(OH)_2$ heated with 10 °C min^{-1} to 500 °C with a dwell time of one hour, (c) mixture of $LiOH{\cdot}H_2O$ and $Ni(OH)_2$ (1.01 Li equivalents per mol of Ni) heated with 10 °C min^{-1} to 500 °C with a dwell time of one hour and (d) mixture of $LiOH{\cdot}H_2O$ and $Ni(OH)_2$ (1.01 Li equivalents per mol of Ni) heated with 10 °C min^{-1} to 600 °C with a dwell time of one hour. Thermogravimetric analysis (TG, blue line) on the left *y*-axis, differential thermal analysis (DTA, red line) and temperature (black dashed line) on the right *y*-axis. The chemical reactions are marked in the DTA data: (i) formation of anhydrous LiOH, (ii) melting of eutectic mixture of LiOH and Li_2CO_3, (iii) melting and decomposition of LiOH to Li_2O and (iv) conversion of $Ni(OH)_2$ to NiO. For the formation of NiO and $LiNiO_2$, the theoretical mass loss after complete conversion is indicated by the green dashed lines. The measurements were performed under O_2 atmosphere. The direction of an exothermic process is indicated by a red arrow.

BASF SE) was mixed with additional NMP and the conductive carbon, and mixed for at least 24 min at 2000 rpm in a planetary mixer (ARE 250, Thinky Corporation). The CAM powders were added to the obtained slurry and were mixed for additional 10 min. The solid fraction of the final slurries was 61 wt%. The slurries were cast onto an Al-foil (thickness 20 μm, Nippon Light Metal Co., Ltd.) using a box-type coater (wet-film thickness 100 μm, width 6 cm, Erichsen GmbH & Co. KG) and an automated coating table (5 mm s^{-1}, Coatmaster 510, Erichsen GmbH & Co. KG). The coated tapes were placed in a vacuum oven (VDL 23, Binder GmbH) and dried at 120 °C under dynamic vacuum for 12 h. The dried cathode tapes were compressed using a calender (CA5, Sumet Systems GmbH) at a set line-force of 30 N mm^{-1} and a roller speed of 0.5 m min^{-1}. Circular electrodes with a diameter of 14 mm were punched out using a high-precision handheld punch (Nogamigiken Co., Ltd.). After weighing, the electrodes were transferred to an Ar filled glovebox for cell assembly. An average loading of (8.0 ± 0.5) mg cm^{-2} and an electrode density of (3.0 ± 0.2) g cm^{-3} were obtained. Coin half-cells were built using a 2032 coin cell geometry. The cell stack consisted of the cathode, a glass fiber separator (ø 17 mm, 300 μm thickness, GF/D, VWR International, LLC.) soaked with 95 μl electrolyte (LP57, BASF SE) and a pre-punched Li anode (ø 15.8 mm, thickness 0.58 mm, purity 99.9%, Shandong Gelon LIB Co., Ltd.). After assembly the cells were closed in an automated crimper (Hohsen Corp.). The cells were then transferred to a climate chamber (Binder GmbH) and connected to a battery cycler (Series4000, MACCOR, Inc.). All tests were performed at 25 °C and the C rates were defined according to 1C = 200 mAg^{-1}.

Results and Discussion

Pathway of the lithiation reaction.—Many reports have dealt with the synthesis of $LiNiO_2$ made via a solid-state route starting from a Li source ($LiOH{\cdot}H_2O$, Li_2CO_3, Li_2O_2, $LiNO_3$) and various Ni salts ($Ni(OH)_2$, NiO, $Ni(NO_3)_2{\cdot}6\ H_2O$).[20,26–30] Several studies used thermogravimetric analysis to resolve the different processes occuring during the calcination reaction and to monitor onset temperature and speed of the reactions.[17,31–33] Prior to the partial-lithiation experiments with its modified temperature profile compared to the one-stage calcination, thermogravimetry and differential thermal analysis (TG-DTA) was performed. Figure 2a shows the results for $LiOH{\cdot}H_2O$ heated at a rate of 10 °C min^{-1} to 500 °C and a dwell time of one hour. Already around 100 °C, a first significant mass loss is observed concomitant with an endothermic peak in the DTA curve, which is related to the loss of water of crystallization and the formation of anhydrous LiOH. On further heating, a small endothermic peak occurs around 420 °C, associated with the melting of the eutectic mixture of LiOH and Li_2CO_3 (small fraction of Li_2CO_3 impurities is likely to be present in the Li source).[34] No further mass loss is observed until the temperature reaches ∼ 450 °C, where a third endothermic peak in the DTA signal arises, which is related to the melting and decomposition of LiOH. During the following one hour dwell time at 500 °C, a continuous mass loss is observed, which is due to the continuous decomposition of LiOH into Li_2O accompanied by the release of H_2O.[35] Note that the temperature, where the transformation to Li_2O starts, strongly depends on the partial pressure of water p_{H2O} in the surrounding atmosphere. It has been reported that for low p_{H2O} the transition to Li_2O occurs before the melting point of LiOH, whereas at increased p_{H2O} the transition to Li_2O starts from liquid LiOH.[36] The TG-DTA measurements were performed with a fast heating rate of 10 °C min^{-1} and thus the start of the transition to Li_2O coincides with the endothermic DTA peak related to the melting of LiOH.

Figure 2b shows the results for the $Ni(OH)_2$ precursor using the same temperature profile. After a small mass change < 1% up to 200 °C, which is most likely related to the loss of enclosed residual H_2O in the layers of the $Ni(OH)_2$ crystal structure, a rapid mass loss is observed between 230 °C and 310 °C. This mass loss slows down on further heating and no additional changes in the TG curve can be seen during the 500 °C hold. The change in mass is related to the conversion of $Ni(OH)_2$ to NiO with a theoretical mass loss of 19.4%.[37,38] This coincides well with the observed mass loss of 19.5% before the holding step at 500 °C and indicates a completed conversion reaction. Thus, pure NiO is present at this point.

Figure 2c depicts the respective measurement of a mixture of $Ni(OH)_2$ and $LiOH{\cdot}H_2O$ with 1.01 Li equivalents per mol of Ni. The same features in the TG-DTA data (formation of anhydrous LiOH, conversion of $Ni(OH)_2$ to NiO, melting of LiOH) are observed as for the separated educts, although the resulting plot is not only a superposition of the previous reactions. The formation of LNO, starting from the used base materials, is given by the reaction in Eq. 1.

$$LiOH{\cdot}H_2O + Ni(OH)_2 + \frac{1}{4}O_2 \rightarrow LiNiO_2 + \frac{5}{2}H_2O \qquad [1]$$

For a complete reaction to $LiNiO_2$, a total mass loss of 27.5% is expected. The total mass loss observed after the one hour dwell at 500 °C was determined to be 25.9%, which means that the lithiation reaction is not completed under these conditions. Repeating the experiment with a dwell time of one hour at 600 °C (Fig. 2d) yields a total mass loss of 27.0% due to a faster reaction at higher temperature, but still the lithiation is not completed.

It must be underlined that the experimental conditions of the TG-DTA measurements do not fully resemble the ones used in the laboratory calcination. Thermal analysis experiments were performed with 60 mg samples in contrast to the laboratory calcination with 60 g sample amount. Moreover, TG-DTA measurements were performed in a furnace with a volume of 100 ml and a gas flow rate of 100 ml min^{-1}, which corresponds to a higher volume exchange rate compared to a calcination in a conventional box furnace (∼ 10 furnace-volume exchanges per hour). It has been reported that the O_2 flow rate has a significant impact on the structural chemistry of LNO, although different reagents and different temperature profiles were used compared to this study.[39] Depite these deviations, the thermal analysis measurements demonstrate the chemical reactions which are expected during a partial-lithiation step on the laboratory-scale and the results will be used in the following discussion.

Comparison between fixed-bed and agitated-bed partial-lithiation.—Partially-lithiated samples were prepared by either mixing $Ni(OH)_2$ with either 80% or with 100% of the amount of $LiOH{\cdot}H_2O$ to obtain 1.01 Li equivalents per mol of Ni. Furthermore, this step was performed under fixed-bed conditions in a box furnace and compared to an agitated-bed process in the metal bulb of a rotary kiln. For the initial experiments, a partial-lithiation temperature of 500 °C, which is well above the melting point of LiOH (T_{melt} ∼ 460 °C), and a dwell time of one hour were chosen.

Figure 3 shows top view SEM images in 1 k magnification of the samples synthesized according to the described procedure. The precursor appears as roughly spherical secondary particle agglomerates, which consist of smaller primary particles with sizes of a few hundred nm. The samples prepared under fixed-bed conditions (Figs. 3c and 3d) show large needle-like lithium-containing residuals, which are attached to the surface of the precursor secondary particles and can grow to several tens of μm in size (it will be rationalized below that the needles are pure LiOH). Obviously, in this case the lithiation reaction is not fully completed and it can be assumed that during cooling of the partially-lithiated materials to room temperature, the formerly molten LiOH recrystallizes in the observed manner.

The sample partially-lithiated with 100% (stoichiometric) Li amount using the rotary kiln setup also shows residuals of the Li source on top of the secondary particles. However, these lithium-containing residuals do not occur as large needles but rather a small spikes. This can be attributed to the rotational movement of the rotary kiln, which can cause the needles to break during the cool-down period. Nevertheless, also in this case the lithiation reaction is

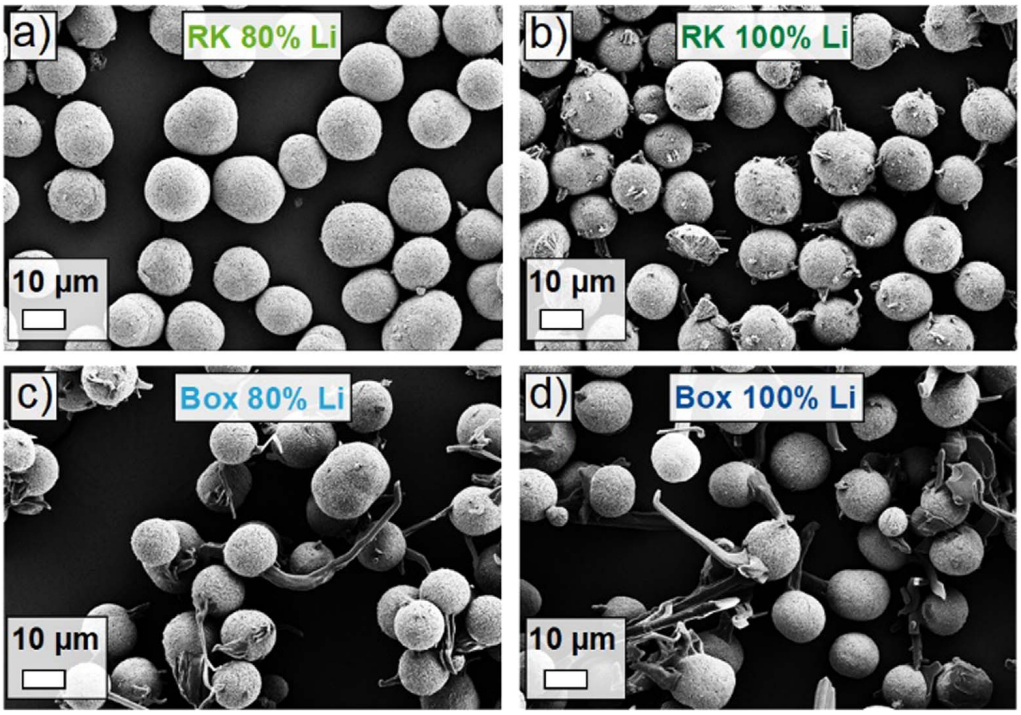

Figure 3. Top view SEM images in 1 k magnification of the samples after a partial-lithiation step at 500 °C and a dwell time of one hour using either the rotary kiln setup (RK) or the box furnace (Box). (a) RK partially-lithiated sample using 80% of the Li amount required to obtain 1.01 Li equivalents per mol of Ni, (b) RK partially-lithiated sample using 100% of the Li amount, (c) box partially-lithiated sample using 80% of the Li amount and (d) box partially-lithiated sample using 100% of the Li amount. The length of the white bar equals 10 μm.

not finished. In contrast to the previous observations, for the sample partially-lithiated with 80% (stoichiometric) Li amount using the rotary kiln setup, no large lithium-containing residuals are observed. This suggests that under these conditions (not all lithium added yet, 500 °C with one hour dwell time *and* rotational movement), the lithiation of the precursor secondary particles has progressed to a large extent. Figure S1 (Supplementary Information) shows the respective top view SEM images in 20 k magnification. The thread-like surface structure of the $Ni(OH)_2$ precursor is maintained to a large extent and no noteworthy crystallite growth is observed yet.

Analytical data of the samples after the partial-lithiation step are summarized in Table I. The results of the ICP-OES measurements reveal that the targeted numbers of Li equivalents are obtained and that no loss of lithium occurs independent of the used furnace concept. The acid titration measurements show that the weight fractions of LiOH and Li_2CO_3 after this first heat treatment are significantly larger compared to CAMs after the main calcination step (see results in Table III). After the cool-down period and during storage, the residual LiOH will take up tiny amounts of H_2O to form $LiOH{\cdot}H_2O$, at least in the near-surface region. The Li_2CO_3 is formed by the reaction between $LiOH{\cdot}H_2O$ and CO_2 from the surrounding atmosphere and the content is higher for the samples with the larger target number of Li equivalents.[40]

Moreover, the amounts of soluble lithium-containing salts in form of LiOH and Li_2CO_3 are generally smaller for the samples partially-lithiated with the rotary kiln setup, when comparing the same target number of Li equivalents. By calculating the weight fractions of "soluble Li" (as described in the experimental section) and comparing the results to the total weight fractions of Li measured with ICP-OES, it is clearly observed that a larger fraction of Li is not incorporated under the fixed-bed compared to the agitated-bed conditions.

Note that for the sample with 80% Li added in the partial-lithiation step using the rotary kiln, a significant amount of residual salts is measured by acid titration, although no large fractions of impurities are observed on the surface of the secondary particles in Fig. 3a. This implies that also in this case the lithiation reaction is not fully completed. However, the results of the acid titration method have to be treated with caution, as will be pointed out below.

The average Ni oxidation states of the partially-lithiated samples were measured via iodometric titration. Starting from $Ni(OH)_2$ (and later on NiO), during lithiation the oxidation state of Ni is gradually increased and for every Li^+ ion incorporated in the structure, one Ni^{2+} has to be oxidized to Ni^{3+} to maintain charge neutrality. This means that for the partially-lithiated samples a Ni oxidation state between +2 and +3 is expected, with a higher oxidation state

Table I. Comparison of analytical data of samples after a partial-lithiation step at 500 °C and a dwell time of one hour for the rotary kiln (RK) and box furnace (Box) design and two different target numbers of Li equivalents per mol of Ni (0.8 and 1.01). Weight fractions of Li and Ni determined by ICP-OES, resulting number of Li equivalents, LiOH and Li_2CO_3 weight fractions measured by acid titration, resulting "soluble Li" weight fraction and average Ni oxidation state determined by iodometric titration.

Sample	Li [wt%]	Ni [wt%]	Li equiv.	LiOH [wt%]	Li_2CO_3 [wt%]	"Soluble Li" [wt%]	Average Ni oxid. state
RK 80% Li	5.9	62.6	0.80	3.07	0.94	1.07	2.74
RK 100% Li	7.0	59.7	0.99	5.29	1.37	1.79	2.89
Box 80% Li	5.9	62.9	0.79	5.37	0.99	1.75	2.63
Box 100% Li	7.0	59.6	0.99	8.91	1.43	2.85	2.63

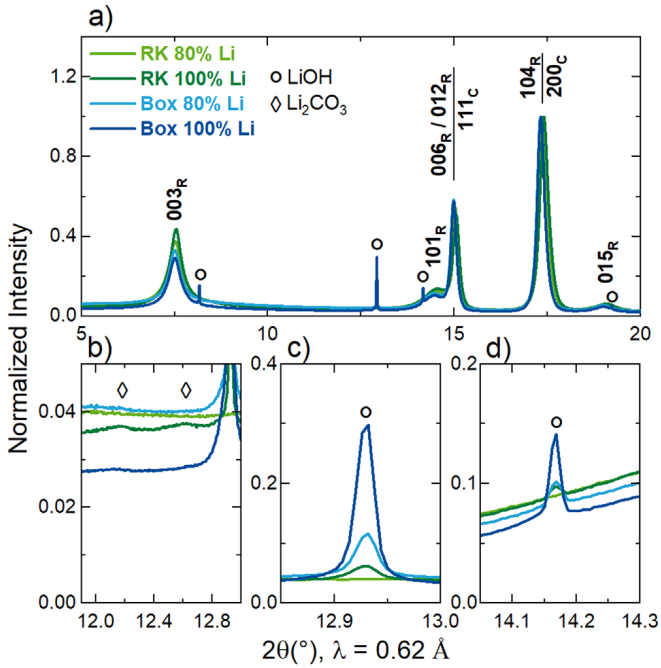

Figure 4. Synchrotron powder X-ray diffraction (PXRD) patterns of the samples after a partial-lithiation step at 500 °C and a dwell time of one hour using either the rotary kiln setup (RK) or the box furnace (Box). Patterns are shown for the RK partially-lithiated sample using 80% of the Li amount required to obtain 1.01 Li equivalents per mol of Ni (light green), for the RK partially-lithiated sample using 100% of the Li amount (dark green), for the box partially-lithiated sample using 80% of the Li amount (light blue) and for the box partially-lithiated sample using 100% of the Li amount (dark blue). (a) PXRD patterns in the range of $2\theta = 5° - 20°$ with the Bragg peaks of the rhombohedral $LiNiO_2$ structure marked by the subscript "R" and the Bragg peaks of the cubic (lithiated) NiO structure marked by the subscript "C". (b)–(d) Magnifications of selected 2θ regions with the symbols marking peaks assigned to the lithium-containing impurities LiOH (circles) and Li_2CO_3 (diamonds). The data were collected at the BL04-MSPD beamline of the ALBA synchrotron at a set wavelength of $\lambda = 0.62$ Å and were normalized to the maximum intensity.

indicating a more advanced lithiation. The results in Table I demonstrate that the partial-lithiation step using the rotary kiln leads to higher Ni oxidation states compared to the reaction in the box furnace under otherwise similar conditions. Notably, the Ni oxidation state under fixed-bed conditions is the same regardless of the used target number of Li equivalents. This shows that, although a larger amount of Li source is provided, the lithiation reaction did not proceed further in this case.

To further characterize the samples after the partial-lithiation step, synchrotron powder X-ray diffraction (PXRD) measurements were performed and the results are depicted in Fig. 4. As can be seen in the overview image (Fig. 4a), none of the partially-lithiated samples exhibits the complete rhombohedral crystal structure of $LiNiO_2$. The dominant Bragg peaks in the PXRD patterns are the 111_C and the 200_C related to the cubic crystal structure of lithiated NiO, whereas the Bragg peaks of the rhombohedral $LiNiO_2$ structure are only indicated by broad humps. Lithiated NiO can be prepared with compositions up to $Li_{0.3}Ni_{0.7}O$, where the Li ions homogeneously distribute within the Ni sublattice.[17,41] Further lithiation leads to the segregation of Li ions and Ni ions into alternating layers, which was shown to be associated with the appearance of the 003_R reflection; a large integrated intensity ratio of $I(003_R)/I(104_R)$ well above 1.0 indicates nearly complete layering,[26] which is not observed for the investigated samples.

Moreover, clear signs of impurity phases are present in the PXRD patterns, which are analyzed in more detail in Figs. 4b–4d. The dominant impurity phase found for the partially-lithiated samples is LiOH, with the magnitude showing a good correlation with the qualitative information from the SEM images and the trends observed via acid titration. The samples heat-treated in the box furnace exhibit larger contributions of the LiOH phase to the diffraction patterns compared to the agitated-bed counterparts with the sample with the larger target number of Li equivalents showing the largest LiOH peak intensities of all investigated materials. Interestingly, the partially-lithiated sample from the rotary kiln setup with 80% of the Li amount does not show any peak intensity originating from crystalline LiOH, which is well in line with the absence of lithium-containing impurities in the SEM image in Fig. 3a. Regarding Li_2CO_3 as second expected impurity phase, only small indications are visible for the two samples prepared with 100% Li amount.

Overall, we can state that the partial-lithiation under agitated-bed conditions using the rotary kiln setup shows a clear advantage over the fixed-bed equivalent regarding the progress of the lithiation reaction under otherwise comparable experimental conditions. However, for an industrially feasible process a second addition of Li source and an additional mixing step prior to the main calcination should be avoided. Thus, in the following section the agitated-bed process will be further investigated using 100% of the required Li amount while optimizing other parameters.

Impact of temperature and dwell time on partial-lithiation.— After the benefits regarding lithiation progress under agitated-bed conditions were pointed out, the influence of partial-lithiation temperature and dwell time on the lithiation reaction were investigated. For this purpose, mixtures of $Ni(OH)_2$ and $LiOH{\cdot}H_2O$ with 1.01 Li equivalents per mol of Ni were prepared and partially-lithiated using the rotary kiln setup and a variation of temperature profiles. Top view SEM images of the mixture before heat treatment and of the partially-lithiated samples in 1 k magnification are depicted in Fig. 5. Before the heating step, $Ni(OH)_2$ secondary particles and $LiOH{\cdot}H_2O$ chunks loosely lie next to each other. In contrast, after a treatment at 400 °C and a dwell time of one hour, it is observed that the precursor particles and the LiOH are in parts "fused together" and that splinters of LiOH are attached to the surface of the $Ni(OH)_2$ secondary particles. This indicates that the lithiation reaction already sets in between the involved solids while the temperature is still well below the melting point of LiOH. This is in good agreement with an *in situ* PXRD report on the synthesis of $LiNiO_2$, where a respective mixture was preannealed at 350 °C for 12 h and significant lithiation of NiO was observed (composition determined to be $Li_{0.22}Ni_{0.78}O$).[17] For the sample partially-lithiated at 500 °C for one hour, formation of needle-like lithium-containing residuals is again observed, with some of them breaking due to the rotational movement. Increasing the dwell time to 2 h at the same temperature reduces the amount of lithium-containing residuals visible in the images significantly, although small spots of impurities still remain on top of the secondary particles. Further increasing the partial-lithiation temperature to 600 °C finally leads to a complete disappearance of visible impurities in the top view SEM images.

The analytical properties of the samples partially-lithiated using different temperatures and dwell times are summarized in Table II. Slightly lower numbers of Li equivalents per mol of Ni were measured compared to the target value of 1.01. The trends of the fractions of soluble lithium-containing residuals that can be titrated are in very good agreement with the discussed top view SEM images in Fig. 5. The reduction of visible impurities in the images coincides with less LiOH and Li_2CO_3 measured via acid titration. Increasing the partial-lithiation temperature from 400 °C to 500 °C leads to a significant reduction of the "soluble Li" weight fraction. This effect is enhanced by doubling the dwell time at 500 °C. Using 600 °C during this step leads to a further reduction of measured LiOH and Li_2CO_3 by further progression of the lithiation reaction. A doubling of the dwell time at 600 °C shows a beneficial effect, although it is smaller as for the lower temperature case due to the already more advanced state of the reaction.

These observations are corroborated by the measured average Ni oxidation states. A one hour partial-lithiation step at 400 °C results

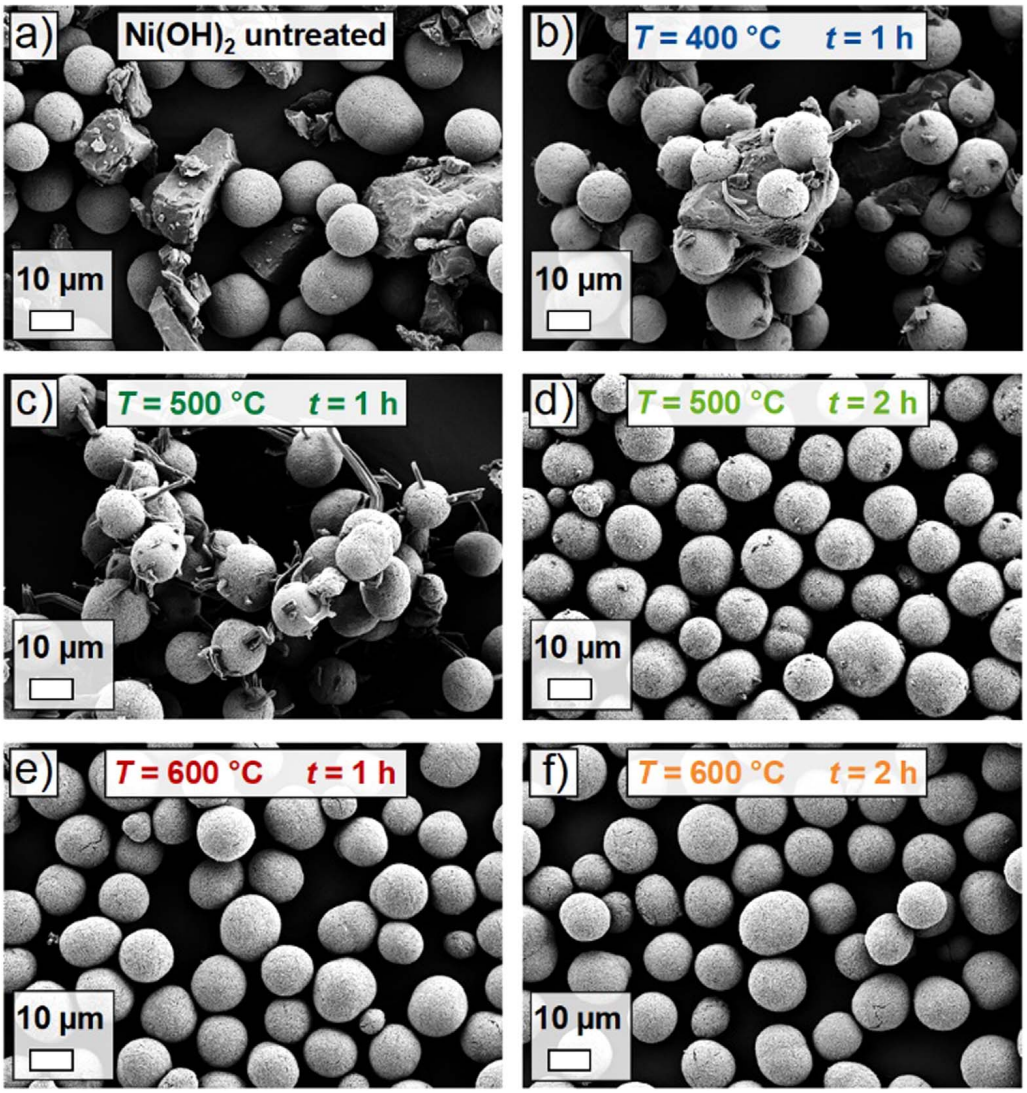

Figure 5. Top view SEM images of the samples in 1 k magnification after a partial-lithiation step using the rotary kiln setup and applying different temperatures and dwell times. (a) Mixture of $LiOH{\cdot}H_2O$ and $Ni(OH)_2$ (1.01 Li equivalents per mol of Ni) before heat treatment. (b) Partially-lithiated sample using 400 °C and a dwell time of one hour, (c) 500 °C and a dwell time of one hour, (d) 500 °C and a dwell time of two hours, (e) 600 °C and a dwell time of one hour and (f) 600 °C and a dwell time of two hours. The length of the white bar equals 10 μm.

Table II. Comparison of analytical data of samples after a partial-lithiation step using the rotary kiln setup and a mixture of $LiOH{\cdot}H_2O$ and $Ni(OH)_2$ (1.01 Li equivalents per mol of Ni). Different temperatures and dwell times were applied for the partial-lithiation step. Weight fractions of Li and Ni determined by ICP-OES, resulting number of Li equivalents per mol of Ni, LiOH and Li_2CO_3 weight fractions measured by acid titration, resulting "soluble Li" weight fraction and average Ni oxidation state determined by iodometric titration.

Sample	Li [wt%]	Ni [wt%]	Li equiv.	LiOH [wt%]	Li_2CO_3 [wt%]	"Soluble Li" [wt%]	Average Ni oxid. state
400 °C 1 h	6.6	57.4	0.97	13.93	0.80	4.19	2.46
500 °C 1 h	6.8	58.2	0.99	6.13	1.62	2.08	2.82
500 °C 2 h	6.7	58.0	0.98	4.00	1.58	1.46	2.94
600 °C 1 h	6.8	58.8	0.98	1.53	1.32	0.69	2.94
600 °C 2 h	6.9	58.8	0.99	1.45	1.17	0.64	2.98

in an average Ni oxidation state of 2.46, which means that barely half of the intended stoichiometric amount of Li is indeed incorporated. The heat treatment at 500 °C and a dwell time of one hour leads to a Ni oxidation state of 2.82, with a further increase to 2.94 when either doubling the dwell time at 500 °C or increasing the temperature to 600 °C. The highest Ni oxidation state of 2.98 is found for the sample partially-lithiated at 600 °C with a dwell time of two hours.

Interestingly, two samples with an identical average Ni oxidation state ("500 °C 2 h" and "600 °C 1 h") show a large difference in the weight fraction of "soluble Li" (1.46 wt% and 0.69 wt%, respectively). We suggest that this can be explained by the disordered crystal structure and small crystallites prone to surface reactions at this early stage of material synthesis. Figure S2 (Supplementary Information) shows representative top view SEM images of the samples after the partial-lithiation step in 20 k magnification and the

impact of partial-lithiation temperature and dwell time can clearly be seen. After the heat treatment at 400 °C for one hour, the thread-like structure of the precursor is still maintained to a large extent. Cavities occur, which are related to the densification from $Ni(OH)_2$ to NiO. Increasing the partial-lithiation temperature to 500 °C leads to the emergence of small crystallites, which are growing in size when 600 °C is applied during this step, although still in the range of only a few tens of nm. Cross section SEM images in Fig. S3 (Supplementary Information) confirm that the discussed observations are not confined to the surface but rather extend into the bulk of the secondary particles.

As discussed in the literature, exposing CAM to H_2O can lead to leaching of Li from the near-surface lattice via the proton exchange reaction depicted in Eq. 2.[42,43]

$$Li^+|_{LNO} + H_2O \rightarrow H^+|_{LNO} + Li^+ + OH^- \quad [2]$$

This contributes to the overall LiOH content, which is measured by the used titration method. The experimental conditions for the dispersion in deionized H_2O were kept constant, but a larger contribution from the leached Li is expected for the "500 °C 2 h" sample compared to the "600 °C 1 h" sample due to the smaller crystallite size (higher surface-to-volume ratio).

To further corroborate the discussed results, PXRD measurements were performed and the outcome is shown in Fig. 6. Significant differences between the samples are observed in the overview image in Fig. 6a. The transition from a lithiated rocksalt-type NiO to the rhombohedral phase of $LiNiO_2$ is clearly measurable when the partial-lithiation temperature profile is adjusted. For the sample partially-lithiated at 400 °C and a dwell time of one hour, large peaks from LiOH impurities can be seen. Instead of a well-defined 003_R Bragg peak, a blurred low-intensity signal is observed. Other than that, the 111_C and 200_C peaks of the cubic phase dominate the PXRD pattern. Increasing the temperature during this step to 500 °C leads to an increase in intensity of the 003_R peak and indications of additional Bragg peaks related to the rhombohedral phase, e.g. 101_R and 015_R. Furthermore, the Bragg peaks formerly corresponding to the solely cubic phase shift to higher diffraction angles as the formation of the rhombohedral $LiNiO_2$ structure proceeds. For the samples partially-lithiated at 600 °C, the transition to the rhombohedral phase has further progressed and the peaks become more defined as the crystallite size increases. However, it must be underlined that the formation of a perfectly layered $LiNiO_2$ crystal structure is not yet reached, which can be concluded, e.g., from the integrated intensity ratio $I(003_R)/I(104_R)$ not being well above 1.0 and from the absence of characteristic peak splittings, e.g. of the 006_R and 012_R peaks. Furthermore the overall background in the PXRD patterns of the 600 °C partially-lithiated samples is still high, which we attribute to amorphous lithium-containing impurity phases on top of the secondary particles and indicate an incomplete crystallization. Minor contributions of Li_2CO_3 to the PXRD pattern can be seen for the samples heat-treated at 500 °C in the magnified image in Fig. 6b, whereas no signs of crystalline Li_2CO_3 are present for the samples partially-lithiated at 600 °C. Figures 6c and 6d show that crystalline LiOH is only present for the samples partially-lithiated at 400 °C and 500 °C and a dwell time of one hour.

To confirm the composition of the needle-like lithium-containing residuals from the incomplete lithiation reaction, they were further investigated by X-ray photoelectron spectroscopy (XPS) with the results depicted in Fig. S4 (Supplementary Information). Three samples were investigated: the untreated $Ni(OH)_2$ precursor (black), the partially-lithiated sample using the rotary kiln setup, 500 °C and a dwell time of one hour (green) and the RK partially-lithiated sample using 600 °C and a dwell time of one hour (red). The $Ni(OH)_2$ serves as a reference without Li, the 500 °C partially-lithiated sample was chosen as it exhibits lithium-containing residual needles and the 600 °C counterpart as in this case there are no residual impurities visible in the SEM image (Fig. 5). The C 1 s spectra of all three samples show one signal at 284.8 eV from

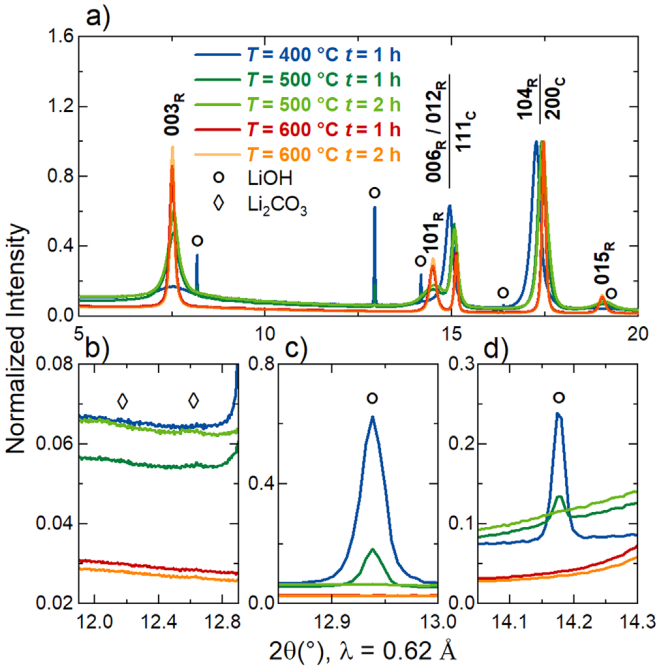

Figure 6. Synchrotron powder X-ray diffraction (PXRD) patterns of the samples after a partial-lithiation step using the rotary kiln setup (RK) and applying different temperatures and dwell times. Patterns are shown for the RK partially-lithiated samples using 100% of the Li amount required to obtain 1.01 Li equivalents per mol of Ni with 400 °C and a dwell time of one hour (blue), 500 °C and a dwell time of one hour (dark green), 500 °C and a dwell time of two hours (light green), 600 °C and a dwell time of one hour (red) and 600 °C and a dwell time of two hours (orange). (a) PXRD patterns in the range of $2\theta = 5°-20°$ with the Bragg peaks of the rhombohedral $LiNiO_2$ structure marked by the subscript "R" and the Bragg peaks of the cubic (lithiated) NiO structure marked by the subscript "C". (b)–(d) Magnifications of selected 2θ regions with the symbols marking peaks assigned to the lithium-containing impurities LiOH (circles) and Li_2CO_3 (diamonds). The data were collected at the BL04-MSPD beamline of the ALBA synchrotron at a set wavelength of $\lambda = 0.62$ Å and were normalized to the maximum intensity.

adventitious carbon contamination. A second signal is visible in the binding energy range of carbonates at around ∼ 289 eV. For the lithiated samples, this signal can mainly be attributed to Li_2CO_3,[44,45] while the carbonate fraction is observed to be very similar for both samples. Since the sample partially-lithiated at 500 °C displays the lithium-containing residual needles and the 600 °C sample does not, Li_2CO_3 can be excluded as the origin of this surface impurity phase. In the case of the $Ni(OH)_2$ reference, the second C 1 s signal most likely stems from carbonate impurities from the precipitation process (the carbon content of the precursor was determined to be 0.13 wt% by elemental analysis).[46,47]

The Ni 2p spectra reveal significant differences between $Ni(OH)_2$ and the heat-treated samples, which can be attributed to the progressive oxidation of Ni^{2+} to Ni^{3+} during the lithiation reaction. However, since there is almost no difference in the Ni 2p spectra between the two partially-lithiated samples (consider the detection limit of the XPS), no absolute values/fractions for the Ni oxidation states can be obtained with this setup.

The Li 1 s spectra of the partially-lithiated samples are mainly composed of two contributions: one signal at a binding energy of 55.0 eV and one at a binding energy of 53.8 eV. Otto et al. investigated the Li 1 s region for a set of lithium-containing compounds and according to this study the signal at 55.0 eV can be attributed to LiOH and/or Li_2CO_3.[48] Moreover, the signal at 53.8 eV binding energy can be related to the lattice Li in $LiNiO_2$.[49] It is observed in Fig. S4 that the relative contribution of LiOH/Li_2CO_3 to the Li 1 s spectrum decreases and the contribution of $LiNiO_2$ increases, when the partial-lithiation temperature is raised from

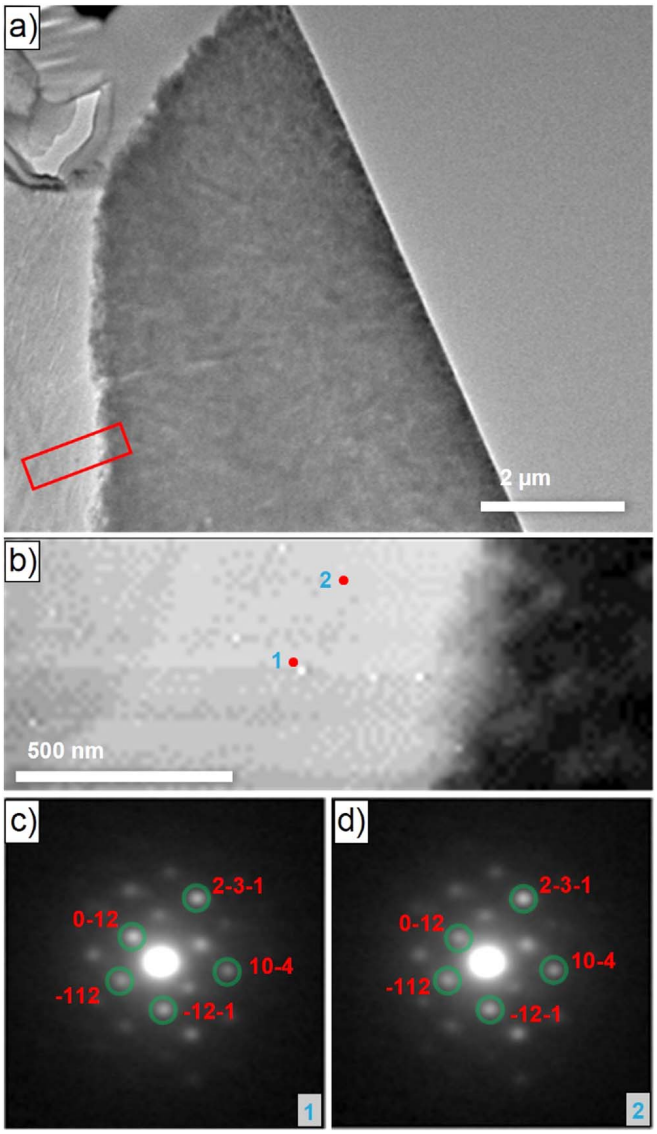

Figure 7. Transmission electron microscopy (TEM) was used for the phase identification of the lithium-containing residual needles. (a) Image of the interface between the precursor secondary particle (right) and one of the needles (left). (b) Scanning-precession electron diffraction virtual bright-field (SPED-VBF) image from the area marked with the red rectangle in (a). The SPED-VBF image was constructed from 4D datasets, which means that at each pixel in (b), there is a 2D-precession electron diffraction (PED) pattern that can be matched with the candidate phases for phase identification. The bright contrast on the left of this image is the residual needle and the dark contrast on the right are primary particles from the precursor secondary particle. (c) and (d) PED patterns from positions 1 and 2 in (b), respectively. The diffraction patterns were matched with the LiOH phase (marked by green circles). The miller indices of some of the exemplary spots/reflections are also marked. The length of the white bar equals 2 μm and 500 nm in (a) and (b), respectively.

500 °C to 600 °C. The same behaviour is found for the O 1 s spectra, where the contribution of $LiOH/Li_2CO_3$ at ~531.5 eV decreases with a concomitant increase of the contribution of LNO at ~528.7 eV. In principle, Li_2O could also be involved as its Li 1 s and O 1 s binding energies overlap with the ones of $LiNiO_2$ and the TGA results revealed that decomposition of LiOH to Li_2O is indeed happening. We did not find any indication of a crystalline Li_2O phase in the PXRD patterns, but small amounts of Li_2O would be difficult to detect by XRD and the reaction with trace amounts of H_2O to form LiOH is expected to be fast.

Transmission electron microscopy (TEM) measurements were performed to conclusively clarify the structure of the lithium-containing residual needles. The sample preparation is depicted in Fig. S5 (Supplementary Information). Figure 7a shows a TEM image of the interface between a lithium-containing residual needle and the precursor secondary particle. Figure 7b is a scanning-precession electron diffraction virtual bright-field (SPED-VBF) image from a 4D dataset taken from the position marked by the red rectangle in Fig. 7a. Figures 7c and 7d depict the PED patterns from two positions marked in Fig. 7b. They are successfully matched with simulated PED patterns from LiOH phase (the matching procedure is described in Fig. S6). It is important to note that the two PED patterns are exemplarily shown in Figs. 7c and 7d to illustrate the phase identification and corresponding matching procedure. The PED patterns from all the pixels from the bright contrast area in the SPED-VBF image in Fig. 7b are successfully matched with the LiOH phase, showing that the lithium-containing residual needles solely consist of LiOH. We also acquired SPED 4D datasets at other positions and found the same result.

To the best of our knowledge, this is the first report on the composition of the lithium-containing residual needles. By combination of PXRD, XPS and SPED-VBF, Li_2CO_3 and Li_2O were excluded and the presence of LiOH was confirmed.

Comparison of LNO samples after main calcination step.—The materials prepared for the comparison between fixed-bed and agitated-bed partial-lithiation were afterwards subjected to a main calcination step. For this purpose, $LiOH{\cdot}H_2O$ was added to the intermediate samples to compensate for the Li deficiency, such that 1.01 Li equivalents per mol of Ni were achieved. The mixtures were then calcined at 700 °C for six hours in a box furnace. Additionally, a "one-step reference" sample was prepared by using a standard temperature profile with a hold at 400 °C for four hours and a second hold at 700 °C for six hours without an intermediate cool-down or a second mixing step (see Fig. 1).

Recently, we introduced an automated SEM image analysis approach to quantify the primary particle size distribution of LNO after calcination.[21] This method was applied to the samples prepared in this study and the results are shown in Fig. 8. Figures 8a and 8b show an exemplary SEM image in 20 k magnification before and after the automated segmentation, respectively. The primary particle size distributions are depicted in Fig. 8c by means of the equivalent diameter defined in the experimental section. No large differences are observed concerning the median primary particle size $Q_{0.5}$ and the width of the size distribution between the two samples calcined following the box furnace partial-lithiation and the one-step reference. In contrast, the two CAMs prepared from the samples partially-lithiated using the rotary kiln show slightly smaller median primary particle sizes and also a narrower size distribution. As discussed, the agitated-bed partial-lithiation with the rotary kiln setup leads to a faster lithiation of the secondary particles and thus less residual LiOH remains compared to the samples heat-treated in the box furnace as observed in Fig. 3. Molten LiOH can support the crystal growth and the fact that a smaller fraction of it is involved in the rotary kiln partially-lithiated samples during the main calcination can be one possible explanation for the slightly smaller primary particle sizes.

Analytical data of the samples after the main calcination step are summarized in Table III. The number of Li equivalents per mol of Ni determined by ICP-OES is very similar for all samples and close to the intended value of 1.01. Moreover, the weight fractions of soluble lithium-containing residuals (as determined by titration) of the CAMs prepared using the partial-lithiation step are comparable to the results of the one-step reference ("soluble Li" weight fraction of ~0.4 wt% for all investigated samples). The average Ni oxidation states of the partially-lithiated samples after the main calcination are very close to +3, although a slightly higher value was obtained for the one-step reference. The reference sample was investigated by

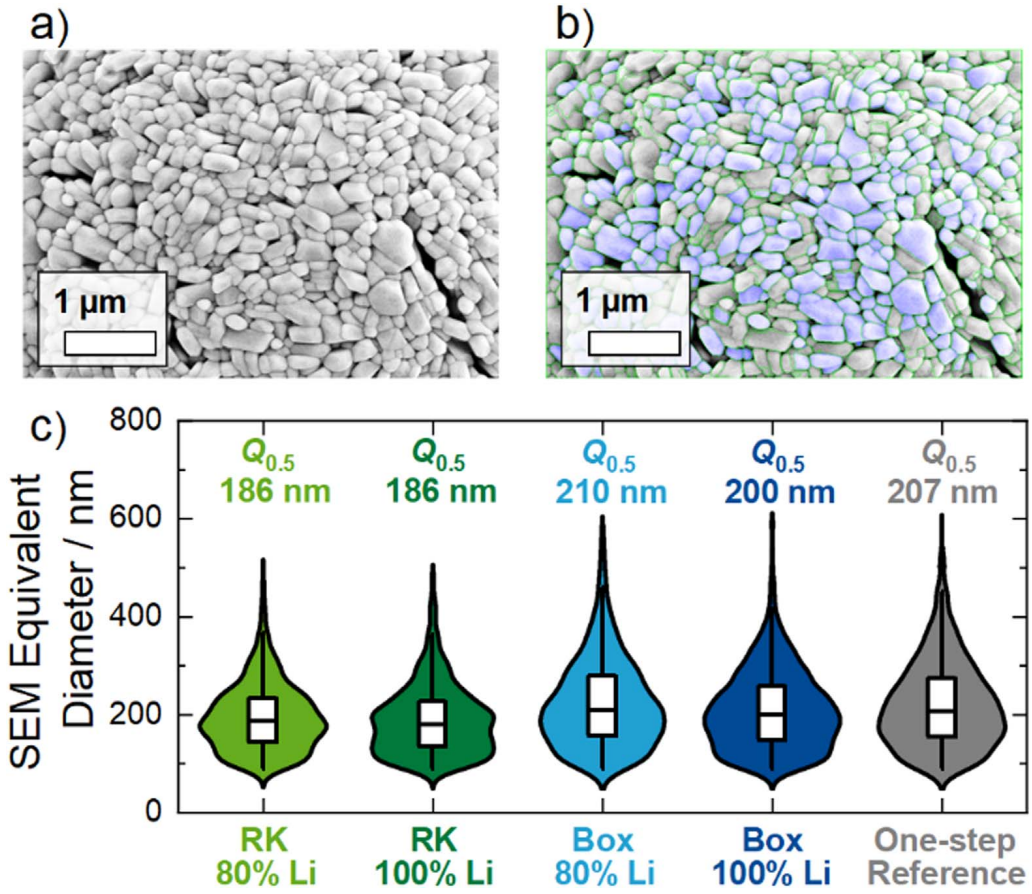

Figure 8. SEM image analysis of the calcined CAM. Top view SEM image of one exemplary sample (a) before primary particle segmentation and (b) after the segmentation. The length of the white bar equals 1 μm. (c) Primary particle size distributions obtained by automated SEM image analysis. Ten images in 20 k magnification of individual secondary particles were analyzed per sample. Results are shown for the calcined samples made from the RK partially-lithiated sample using 80% of the Li amount required to obtain 1.01 Li equivalents per mol of Ni (light green), from the RK partially-lithiated sample using 100% of the Li amount (dark green), from the box partially-lithiated sample using 80% of the Li amount (light blue), from the box partially-lithiated sample using 100% of the Li amount (dark blue) and for the one-step reference sample (gray). The particle size distributions are depicted as violin plots with the *y*-axis showing the equivalent diameter and the width in *x*-axis direction indicating the probability density distribution as a kernel smoothed histogram. The boxes indicate the median as well as the 25% and 75% percentiles, with the whiskers extending to the 10% and 90% percentiles. The median values $Q_{0.5}$ are shown as numbers as well.

Table III. Comparison of analytical results after the main calcination of samples beforehand partially-lithiated at 500 °C and a dwell time of one hour for the rotary kiln (RK) and box furnace (Box) design and two different numbers of Li equivalents (0.8 and 1.01). The results for a material synthesized with a one-step calcination are shown as well. Weight fractions of Li and Ni determined by ICP-OES, resulting number of Li equivalents per mol of Ni, weight fractions of LiOH and Li_2CO_3 measured by acid titration, resulting "soluble Li" weight fraction and average Ni oxidation state determined by iodometric titration.

Sample	Li [wt%]	Ni [wt%]	Li equiv.	LiOH [wt%]	Li_2CO_3 [wt%]	"Soluble Li" [wt%]	Ni oxid. state
RK 80% Li	7.1	60.0	1.00	0.92	0.63	0.39	2.93
RK 100% Li	7.1	60.0	1.00	0.86	0.81	0.40	2.95
Box 80% Li	7.0	60.0	0.99	0.82	0.80	0.39	2.95
Box 100% Li	7.0	60.0	0.99	0.92	0.49	0.36	2.95
One-step ref.	7.0	58.9	1.01	0.81	0.72	0.37	2.99

iodometric titration immediately upon preparation, whereas the partially-lithiated samples were stored for some time prior to the measurement. Although the samples were stored in an air-tight box inside a dry room, $LiNiO_2$ already reacts with trace amounts of moisture (occuring e.g. during sample bottling) and decomposes to a lithiated rock salt-type phase over time, which leads to a decrease of the Ni oxidation state.

Finally, the prepared CAMs were characterized regarding their electrochemical behavior in coin half-cells. The 1st cycle voltage profiles of all samples shown in Fig. 9a are very similar and no significant differences compared to the one-step reference are observed. The results depicted in Table IV do not show large deviations regarding the 1st cycle charge capacities and only slightly lower 1st cycle discharge capacities for the samples prepared with a partial-lithiation step in the box furnace. The small differences are also reflected in the 1st cycle capacity loss, which deviates by ± 3 mAh g^{-1}. We have reported in a recent publication that the primary particle morphology is the decisive factor for the electrochemical performance of LNO, determines the 1st cycle capacity loss and that samples with a smaller primary particle size show a higher Coulombic efficiency.[21] In the present work, this is also observed for the comparison between the samples partially-lithiated with the

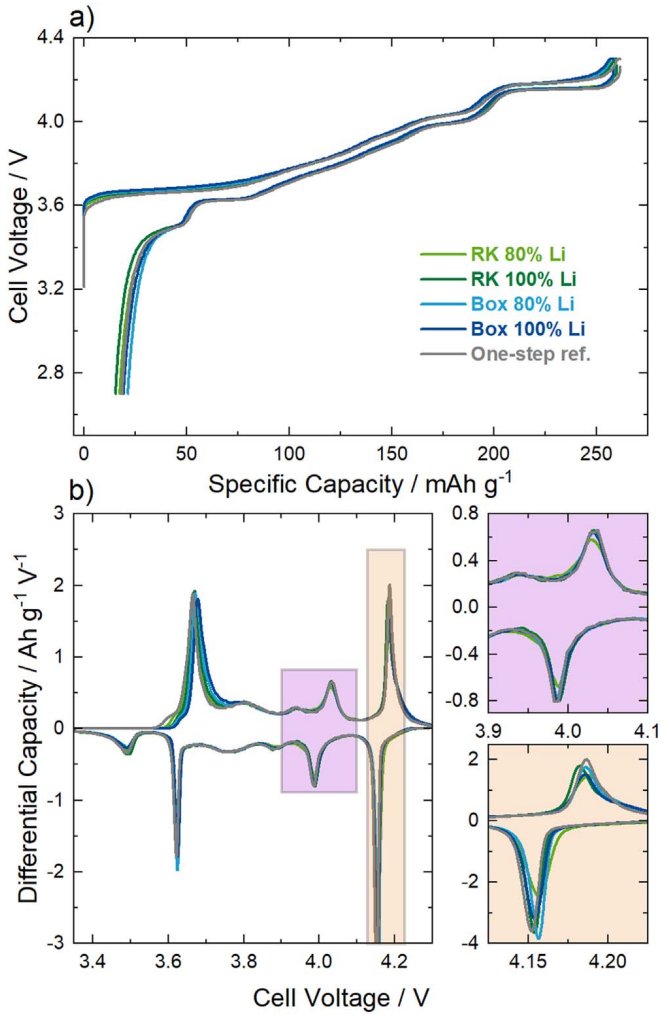

Figure 9. Electrochemical analysis of the calcined CAM made from the RK partially-lithiated sample using 80% of the Li amount required to obtain 1.01 Li equivalents per mol of Ni (light green), from the RK partially-lithiated sample using 100% of the Li amount (dark green), from the box partially-lithiated sample using 80% of the Li amount (light blue), from the box partially-lithiated sample using 100% of the Li amount (dark blue) and for the one-step reference sample (gray). (a) Cell voltage vs specific capacity of the 1st cycle and (b) differential capacity vs cell voltage. Two magnifications of the data in the range of 3.9–4.1 V (purple) and 4.125–4.225 V (orange) are shown. All measurements were performed in a coin half-cell setup with Li metal anodes and a glass fiber separator soaked with LP57 as electrolyte. The measurement temperature was set at 25 °C with a current rate of 10 mA g^{-1}.

rotary kiln setup (comparatively smaller primary particles) and the samples partially-lithiated with the box furnace (comparatively larger primary particles, see Fig. 8), as the RK samples show a smaller 1st cycle capacity loss. However, the one-step reference sample exhibits a primary particle size distribution similar to the samples partially-lithiated with the box furnace, but a smaller 1st cycle capacity loss. Note that the differences in primary particle sizes are much smaller ($Q_{0.5}$ values deviating by $\sim$ 20 nm) compared to the previous work and therefore marginal variance in sample properties can attribute for the different 1st cycle results.

Several reports have shown that LNO tends to an excess of z Ni^{2+} ions in the Li layer ("off-stoichiometry") and is thus better described by $Li_{1-z}Ni_{1+z}O_2$. We have shown in a recent report that *dQ/dV* analysis is a valuable tool to characterize the structural chemistry of LNO and the value of z in particular.[22] Figure 9b shows the *dQ/dV* curves of the 1st cycle for all calcined materials with the magnified views depicting two distinct voltage ranges. All materials exhibit the common structural phase transitions of LNO during (de-) lithiation, which occur as peaks in the *dQ/dV* curves.

The purple inset shows the voltage range between 3.9–4.1 V, where a local minimum in the *dQ/dV* corresponding to $Li_{0.4}NiO_2$ is expected.[50] We have shown that materials with a small Ni excess (z = 0.016–0.022, determined as Ni occupancy on the Li site by Rietveld refinement) exhibit two peaks with a clear local minimum, whereas for samples with Ni excess values exceeding a certain threshold ($z \sim 0.03$), this minimum is no longer observed in the *dQ/dV* curve. All samples from the present study display the local minimum, and thus, only moderate off-stoichiometry is expected.

The orange inset shows the peaks related to the H2 to H3 phase transition. Our recent publication revealed that there is a linear correlation between the mean potential of this phase transition and the Ni occupancy on the Li site. This relation was found to be valid for samples made from two individual $Ni(OH)_2$ precursors from the same supplier as the one used in this study. The results for the mean potential of the H2 to H3 phase transition are depicted in Table IV and, as already expected from Fig. 9b, the mean potentials are very similar and deviate by not more than 4 mV. This again underlines that the off-stoichiometry of the samples is very similar regardless of whether a partial-lithiation step was used or not.

We also performed PXRD measurements and Rietveld refinement for all calcined samples of this study using the same structural model as in our previous report.[22] This was done to compare the amount of Ni excess and the average crystallite size obtained from the refinement to the results of the *dQ/dV* analysis and the SEM image segmentation.

As can be seen for one exemplary sample (partially-lithiated using 1.01 Li equivalents and the rotary kiln setup before main calcination) in Figs. S7a and S7b (Supplementary Information), this structural model leads to a good fit but with some remaining differences between the measured and the calculated patterns, which is further on expressed in the reliability factors depicted in Table SI. One possible explanation could be anisotropic size effects, where line broadening in the PXRD patterns is caused by the deviation of the crystallite shape from the ideal spherical symmetry. This effect was shown to determine the line broadening in the PXRD patterns of plate-like $Ni(OH)_2$ particles using a structural model based on linear combinations of spherical harmonics.[23] This approach was used in the present study to investigate whether including anisotropy in the structural model improves the goodness of fit after refinement. It is evident from the results in Figs. S7c and S7d, that indeed this

Table IV. Electrochemical properties of the calcined samples measured during the 1st cycle in a coin half-cell setup. All measurements were performed with Li metal anodes and a glass fiber separator soaked with LP57 as electrolyte. The measurement temperature was set at 25 °C with a current rate of 10 mA g^{-1}. Three cells per sample were evaluated.

Sample	Charge Capacity [mAh g^{-1}]	Discharge Capacity [mAh g^{-1}]	Capacity loss [mAh g^{-1}]	H2-H3 Mean Potential [V]
RK 80% Li	260.4(5)	242.5(1)	17.9	4.176
RK 100% Li	259.9(2)	244.3(1)	15.6	4.172
Box 80% Li	258.5(1)	237.2(2)	21.3	4.174
Box 100% Li	258.5(4)	239.1(2)	19.4	4.174
One-step ref.	260.7(7)	242.6(2)	18.1	4.172

structural model leads to an improved fitting. Moreover, this is also observed for the other CAMs prepared in this study as can be seen by comparing the reliability factors in Table SI.

We believe that the anisotropy might be caused by the specific morphology of the $Ni(OH)_2$ precursor ($d_{50} = 10\ \mu m$) employed in this study, which features more anisotropic primary grains and hence differs slightly from the previously used ones (same commercial precursor supplier, $d_{50} = 4\ \mu m$ and $12\ \mu m$, respectively[22]), leading to anisotropic growth of the crystallites. On the other hand, the anisotropy model includes five additional free parameters and thus an improved fitting could be of artificial nature and not fully related to the model itself. Besides, the anisotropy model prevents the evaluation of one single average crystallite size (it results in an apparent size value for all crystallographic directions, e.g., 180 nm along 003 and 230 nm along 110 for the sample depicted in Fig. S7) in contrast to the conventional model for approximately spherical crystallites. Finally, both the anisotropy model and the "conventional model" used in the previous work lead to comparably large off-stoichiometry values of $0.025 < z < 0.036$ (the z values are ~0.002–0.004 larger when the anisotropy model is used). This result is contrary to the *dQ/dV* analysis, which indicates that a rather moderate off-stoichiometry is present in all samples ($z \approx 0.02$). All in all, we believe that it is more convenient for the present samples to rely on the electrochemical data and the SEM image analysis for evaluation of the off-stoichiometry and primary particle size distribution, respectively.

Implications for future CAM production design.—In summary, the investigations in the last section confirm that materials prepared by a synthesis including a partial-lithiation step indeed show similar physico-chemical properties and electrochemical behavior when compared to conventionally calcined samples. The open point remains whether this two-stage calcination concept can have a beneficial impact on large-scale CAM production.

As explained in the introduction, an increased CAM calcination throughput directly translates into a production cost decrease. This throughput increase is currently addressed by using roller hearth kilns with a larger number of saggers in a row and additional sagger layers on top.[51,52] However, to exploit the full potential of this synthesis concept, still higher sagger loadings and shorter calcination times are required. This in turn can potentially cause a demixing of precursor and Li source due to H_2O evolution and melting processes together with an inhomogeneous temperature distribution inside the saggers, leading to a variation of chemical composition and crystallite size in the final product.

Although a laboratory process with restricted sample size cannot probe all these issues to the full extent, a simple calculation can illustrate the tremendous advantage of the partial-lithiation concept regarding economically feasible production. An exemplary sagger used in industrial production has a size of 33 cm × 33 cm × 10 cm (wall thickness ~1 cm) and the bulk density of the mixture of $Ni(OH)_2$ and $LiOH{\cdot}H_2O$ is ~1 g cm^{-3}, corresponding to a maximum loading of 8.65 kg. Filling the sagger up to 80% of the total volume corresponds to a loading of 6.92 kg. As discussed in the context of the TG-DTA data, full conversion of the used precursors to $LiNiO_2$ will lead to a mass loss of 27.5% in the form of H_2O vapor, meaning that only 5.02 kg per sagger and production run are obtained as final product. In contrast, the bulk density of the "500 °C 2 h" partially-lithiated sample was determined to be 2.3 g cm^{-3} and the two samples heat-treated at 600 °C showed bulk densities of 2.4 g cm^{-3}. Filling the same sagger volume as before, loadings of 15.91–-16.60 kg can be achieved without additional mass losses in the main calcination as the removal of H_2O is completed during the partial-lithiation step. In the present case, the amount of CAM per sagger and production run can thus be increased by a factor of ~3.

Certainly, this is a rather rough estimation and a higher bulk density will also lead to a time delay during heating and cooling, which requires an adjustment of the temperature profiles. Furthermore, a two-stage calcination concept including a partial-lithiation step in a rotary kiln requires additional capital expenditures for the kiln and its infrastructure (filling and emptying equipment, O_2 atmosphere, etc.). However, the metal bulb of the rotary kiln is more robust against fast heating compared to the ceramic saggers and therefore heating ramps up to 30 °C min^{-1} can be used instead of the standard 3 °C min^{-1} applied for a roller hearth kiln. Moreover, the rotational movement and the continuous supply of fresh O_2 gas to the mixture of precursor and Li source leads to a fast lithiation, and dwell times of not more than two hours are needed. The calcination in a roller hearth kiln is an energy-intensive process step and thus the dwell time in this furnace should be as short as possible. With the use of the two-stage calcination, the overall time in the roller hearth kiln can be reduced as no plateau in the medium temperature region (400 °C–500 °C) is used and higher sagger loadings can be realized, both leading to an increased production throughput.

Unfortunately, performing the entire calcination only with the rotary kiln would not be cost-effective as temperatures of 700 °C and more are needed for complete formation of the rhombohedral structure and proper growth of the crystallites. The herein used metal bulb of the rotary kiln is composed of a Ni-Fe-Cr alloy (Inconel 600), which is specified to be corrosion-resistant against high temperatures and oxidizing conditions. However, the molten Li source is believed to be very corrosive and to aggressively react with the alloy, especially at elevated temperatures, which will lead to corrosion of the bulb over time and impurities in the final product. Thus, a compromise has to be found regarding the partial-lithiation temperature profile, such that the lithiation reaction is (almost) finished, but the metal bulb is not severely affected. We believe that in the present study a partial-lithiation temperature of 500 °C and a dwell time of two hours is the favorable profile as the lithiation has progressed to a large extent (only small lithium-containing impurities visible in the SEM images, Ni oxidation state is 2.94) and the bulk density is similar to the values obtained for the samples prepared at 600 °C. Note that this is only valid for the educts used in this study and that precursors with different morphology (crystallite size and aspect ratio, porosity) and chemical composition might require an adjusted temperature profile. In particular, the impact of the other transition metals Co, Mn and Al on the kinetics of the lithiation of $Ni_{1-x-y}Co_xMn_y(OH)_2$ and $Ni_{1-x-y}Co_xAl_y(OH)_2$ precursors needs to be investigated.

Conclusions

We have shown in this report for the synthesis of $LiNiO_2$, as model system for Ni-rich NCM and NCA cathode materials, that a two-stage calcination process including a partial-lithiation step has the potential to increase the calcination throughput while still resulting in a final product with similar physico-chemical properties and electrochemical behavior compared to a one-step calcination. It is pointed out that the agitated-bed partial-lithiation using the rotational movement of a rotary kiln setup leads to a faster lithiation reaction compared to the fixed-bed counterpart in a crucible. Moreover, the impact of the temperature and the dwell time on the progress of the agitated-bed partial-lithiation was investigated. Taking the corrosion issue of the metal rotary bulb into account, the optimum conditions for the present starting materials $LiOH{\cdot}H_2O$ and $Ni(OH)_2$ were determined to be 500 °C and a dwell time of two hours within the chosen parameter space of the heat treatment. The use of such partially-lithiated samples would lead to a potential increase in sagger loadings by a factor of ~3 and therefore to an immensely increased throughput in large-scale production. The temperature profile needs to be optimized for precursors with different morphology and chemical composition, although the benefits of the two-stage calcination are expected to remain. Further advantages of the partial-lithiation process regarding homogeneity of the composition and crystallite size of the CAM are believed to come into view as soon as large-scale sample amounts are investigated, which will be part of future work.

Acknowledgments

François Fauth and the BL04-MSPD beamline team at the ALBA synchrotron are gratefully acknowledged for their support to the PXRD measurements. Daniel Sander from BASF SE's group Calcination and Combustion is gratefully acknowledged for the help and advise with the rotary kiln setup.

Funding

Shamail Ahmed and Kerstin Volz gratefully acknowledge the funding from Bundesministerium für Bildung und Forschung (BMBF) within the FESTBATT cluster of competence (project 03XP0433C).

ORCID

Philipp Kurzhals https://orcid.org/0000-0002-7013-080X
Felix Riewald https://orcid.org/0000-0001-9002-3633
Matteo Bianchini https://orcid.org/0000-0003-4034-7706
Felix Walther https://orcid.org/0000-0002-5843-4237
Jürgen Janek https://orcid.org/0000-0002-9221-4756

References

1. W. Li, E. M. Erickson, and A. Manthiram, *Nat. Energy*, **5**, 26 (2020).
2. S.-T. Myung, F. Maglia, K.-J. Park, C. S. Yoon, P. Lamp, S.-J. Kim, and Y.-K. Sun, *ACS Energy Lett.*, **2**, 196 (2017).
3. W. Bernhart, *Lithium-Ion Batteries*, ed. G. Pistoia (Elsevier, Amsterdam) p. 553 (2014).
4. K. Turcheniuk, D. Bondarev, G. G. Amatucci, and G. Yushin, *Mater. Today*, **42**, 57 (2021).
5. W. Bernhart, *ATZelectronics worldwide*, **14**, 38 (2019).
6. A. Saavedra, N. A. Galvis, F. Mesa, E. Banguero, M. Castaneda, S. Zapata, and A. J. Aristizabal, *International Journal on Engineering Applications*, **9**, 115 (2021).
7. Global Energy Review, (2021), (https://iea.org/reports/global-energy-review-2021) (accessed: 06.03.2022) *International Energy Agency* (IAE, Paris).
8. S. Taniguchi, (2009), JP2009/103331 A Roller Hearth Kiln.
9. Y. Kawakami and T. Nihei, (2018), JP2018/193296A Production Method of Lithium Nickel Composite Oxide.
10. Y.-M. Park, S.-C. Hwang, C.-M. Yang, and W.-T. Kim, (2017), WO2017/217625 A1 Sagger for firing active material of lithium secondary battery, and method for manufacturing active material using same.
11. D. Ham et al., (2019), US2019/0074513 A1 Cathode active material precursor, cathode active material formed therefrom, method of preparing the cathode active material, and cathode, and lithium battery each including the cathode active material.
12. Y. Kim, H. Park, J. H. Warner, and A. Manthiram, *ACS Energy Lett.*, **6**, 941 (2021).
13. A. Manthiram, B. Song, and W. Li, *Energy Storage Mater.*, **6**, 125 (2017).
14. J. Kim, H. Lee, H. Cha, M. Yoon, M. Park, and J. Cho, *Adv. Energy Mater.*, **8**, 1702028 (2018).
15. A. Park, J. Kim, S.-Y. Han, J. Paulsen, K.-T. Lee, and R. De Palma, (2018), WO2018/158078 A1 Precursor and method for preparing Ni based cathode material for rechargeable lithium ion batteries.
16. I. Petrovic, A. Thurston, and S. Sheargold, (2012), WO/1778332012 Process for synthesis of a layered oxide cathode composition .
17. M. Bianchini, F. Fauth, P. Hartmann, T. Brezesinski, and J. Janek, *J. Mater. Chem. A*, **8**, 1808 (2020).
18. H. Arai, M. Tsuda, and Y. Sakurai, *J. Power Sources*, **90**, 76 (2000).
19. H. Li, N. Zhang, J. Li, and J. R. Dahn, *J. Electrochem. Soc.*, **165**, A2985 (2018).
20. A. Mesnier and A. Manthiram, *ACS Appl. Mater. Interfaces*, **12**, 52826 (2020).
21. F. Riewald, P. Kurzhals, M. Bianchini, H. Sommer, J. Janek, and H. Gasteiger, *J. Electrochem. Soc.*, **169**, 020529 (2022).
22. P. Kurzhals, F. Riewald, M. Bianchini, H. Sommer, H. A. Gasteiger, and J. Janek, *J. Electrochem. Soc.*, **168**, 110518 (2021).
23. M. Casas-Cabanas, M. R. Palacín, and J. Rodríguez-Carvajal, *Powder Diffr.*, **20**, 334 (2005).
24. E. F. Rauch, J. Portillo, S. Nicolopoulos, D. Bultreys, S. Rouvimov, and P. Moeck, *Z. Kristallogr.*, **225**, 103 (2010).
25. E. F. Rauch, P. Harrison, X. Zhou, M. Herbig, W. Ludwig, and M. Véron, *Symmetry*, **13**, 1675 (2021).
26. T. Ohzuku, A. Ueda, and M. Nagayama, *J. Electrochem. Soc.*, **140**, 1862 (1993).
27. A. Rougier, P. Gravereau, and C. Delmas, *J. Electrochem. Soc.*, **143**, 1168 (1996).
28. M. Song, I. Kwon, H. Kim, S. Shim, and D. R. Mumm, *J. Appl. Electrochem.*, **36**, 801 (2006).
29. V. Bianchi, D. Caurant, N. Baffier, C. Belhomme, E. Chappel, G. Chouteau, S. Bach, J. P. Pereira-Ramos, A. Sulpice, and P. Wilmann, *Solid State Ionics*, **140**, 1 (2001).
30. A. Hirano, R. Kanno, Y. Kawamoto, Y. Takeda, K. Yamaura, M. Takano, K. Ohyama, M. Ohashi, and Y. Yamaguchi, *Solid State Ionics*, **78**, 123 (1995).
31. H. X. Yang, Q. F. Dong, X. H. Hu, X. P. Ai, and S. X. Li, *J. Power Sources*, **79**, 256 (1999).
32. S. Li, Q. Wu, C. Zhang, H. Zhu, C. Zhang, X. Wang, and C. Kong, *Materials Science-Poland*, **36**, 107 (2018).
33. R. Weber, H. Li, W. Chen, C.-Y. Kim, K. Plucknett, and J. Dahn, *J. Electrochem. Soc.*, **167**, 100501 (2020).
34. C. W. Bale and A. D. Pelton, *Calphad*, **6**, 255 (1982).
35. H. Kudo, *J. Nucl. Mater.*, **87**, 185 (1979).
36. J. M. Kiat, G. Boemare, B. Rieu, and D. Aymes, *Solid State Commun.*, **108**, 241 (1998).
37. M. Aghazadeh, A. N. Golikand, and M. Ghaemi, *Int. J. Hydrogen Energy*, **36**, 8674 (2011).
38. A. Al-Hajry, A. Umar, M. Vaseem, M. Al-Assiri, F. El-Tantawy, M. Bououdina, S. Al-Heniti, and Y.-B. Hahn, *Superlattices Microstruct.*, **44**, 216 (2008).
39. C.-H. Lu and L. Wei-Cheng, *J. Mater. Chem.*, **10**, 1403 (2000).
40. D. Williams and R. Miller, *Industrial & Engineering Chemistry Fundamentals*, **9**, 454 (1970).
41. J. Goodenough, D. Wickham, and W. Croft, *J. Phys. Chem. Solids*, **5**, 107 (1958).
42. I. A. Shkrob, J. A. Gilbert, P. J. Phillips, R. Klie, R. T. Haasch, J. Bareño, and D. P. Abraham, *J. Electrochem. Soc.*, **164**, A1489 (2017).
43. D. Pritzl, T. Teufl, A. T. S. Freiberg, B. Strehle, J. Sicklinger, H. Sommer, P. Hartmann, and H. A. Gasteiger, *J. Electrochem. Soc.*, **166**, A4056 (2019).
44. F. Walther, F. Strauss, X. Wu, B. Mogwitz, J. Hertle, J. Sann, M. Rohnke, T. Brezesinski, and J. Janek, *Chem. Mater.*, **33**, 2110 (2021).
45. K. Kanamura, H. Tamura, S. Shiraishi, and Z. i Takehara, *J. Electrochem. Soc.*, **142**, 340 (1995).
46. A. Delahaye-Vidal, B. Beaudoin, N. Sac-Epée, K. Tekaia-Elhsissen, A. Audemer, and M. Figlarz, *Solid State Ionics*, **84**, 239 (1996).
47. D. S. Hall, D. J. Lockwood, C. Bock, and B. R. MacDougall, *Proc Math Phys Eng Sci*, **471**, 20140792 (2015).
48. S.-K. Otto, Y. Moryson, T. Krauskopf, K. Peppler, J. Sann, J. Janek, and A. Henss, *Chem. Mater.*, **33**, 859 (2021).
49. L. Mu, Z. Yang, L. Tao, C. K. Waters, Z. Xu, L. Li, S. Sainio, Y. Du, H. L. Xin, D. Nordlund, and F. Lin, *J. Mater. Chem. A*, **8**, 17487 (2020).
50. M. Mock, M. Bianchini, F. Fauth, K. Albe, and S. Sicolo, *J. Mater. Chem. A*, **9**, 14928 (2021).
51. NGK Insulators, (accessed: 24.11.2021) https://ngk-insulators.com/en/product/hd-roller-kiln.html.
52. Onejoon Co. Ltd, (accessed: 24.11.2021) https://onejoon.de/site/assets/files/17007/onejoon_whitepaper_why_the_battery_ pusher_kiln.pdf.

SUPPLEMENTARY INFORMATION

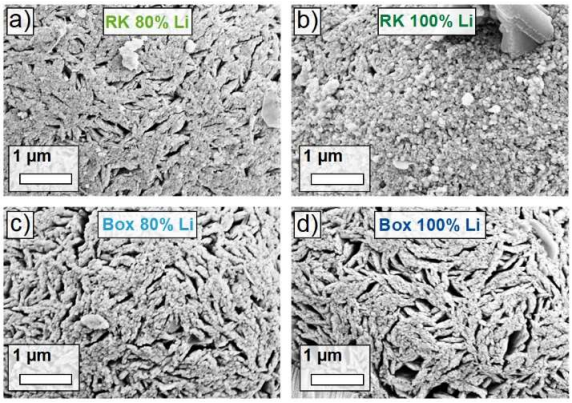

Figure S1: Top view SEM images in 20 k magnification of the samples after a partial-lithiation step at 500 °C and a dwell time of one hour using either the rotary kiln setup (RK) or the box furnace (Box). **a)** RK partially-lithiated sample using 80% of the Li amount required to obtain 1.01 Li equivalents per mol of Ni, **b)** RK partially-lithiated sample using 100% of the Li amount, **c)** box partially-lithiated sample using 80% of the Li amount and **d)** box partially-lithiated sample using 100% of the Li amount. The length of the white bar equals 1 µm.

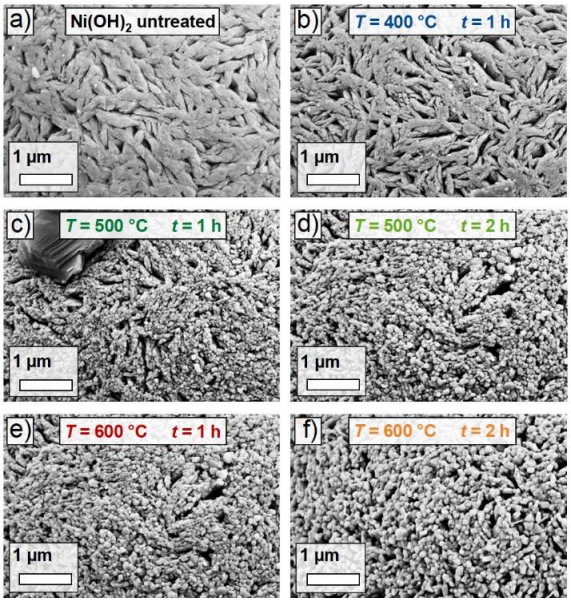

Figure S2: Top view SEM images of the samples in 20 k magnification after a partial-lithiation step using the rotary kiln setup and applying different temperatures and dwell times. **a)** $Ni(OH)_2$ before the heat treatment. **b)** Partially-lithiated sample using 400 °C and a dwell time of one hour, **c)** 500 °C and a dwell time of one hour, **d)** 500 °C and a dwell time of two hours, **e)**

600 °C and a dwell time of one hour and **f)** 600 °C and a dwell time of two hours. The length of the white bar equals 1 µm.

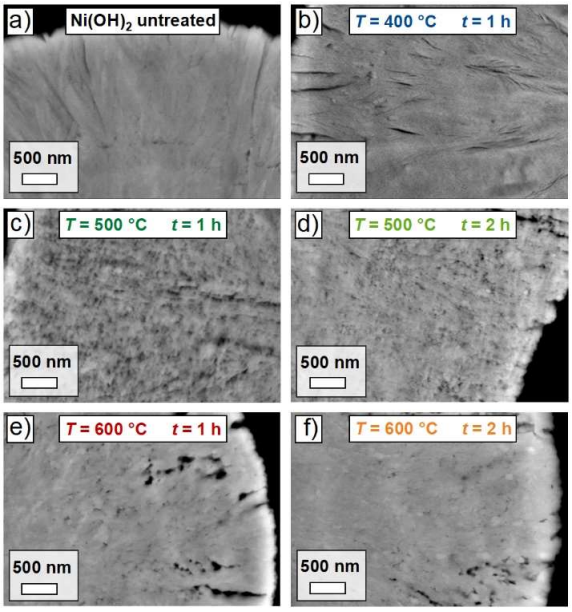

Figure S3: Cross section SEM images of the samples in 30 k magnification after a partial-lithiation step using the rotary kiln setup and applying different temperatures and dwell times. **a)** $Ni(OH)_2$ before the heat treatment. **b)** Partially-lithiated sample using 400 °C and a dwell time of one hour, **c)** 500 °C and a dwell time of one hour, **d)** 500 °C and a dwell time of two hours, **e)** 600 °C and a dwell time of one hour and **f)** 600 °C and a dwell time of two hours. The length of the white bar equals 500 nm.

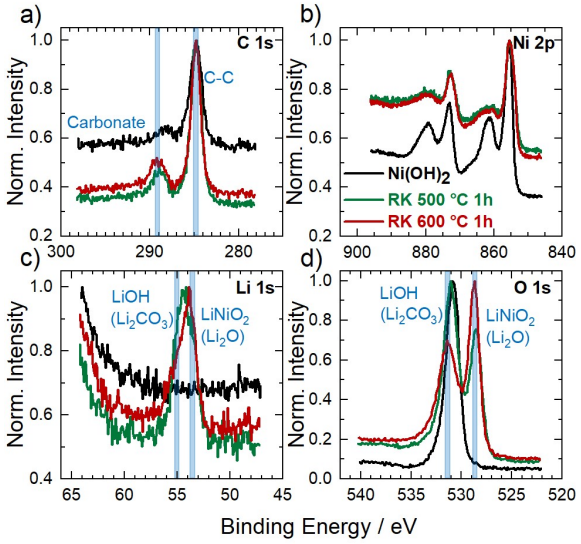

Figure S4: X-ray photoelectron spectroscopy (XPS) analyses of pure $Ni(OH)_2$ (black), the RK partially-lithiated sample using 100% of the Li amount required to obtain 1.01 Li equivalents per mol of Ni using 500 °C and a dwell time of one hour (green), and the RK partially-lithiated sample using the same Li amount and 600 °C and a dwell time of one hour (red). **a)** C 1s spectra, **b)** Ni 2p spectra, **c)** Li 1s spectra and **d)** O 1s spectra. The signal positions related to certain compounds are indicated by blue lines in **a)**, **c)** and **d)**.

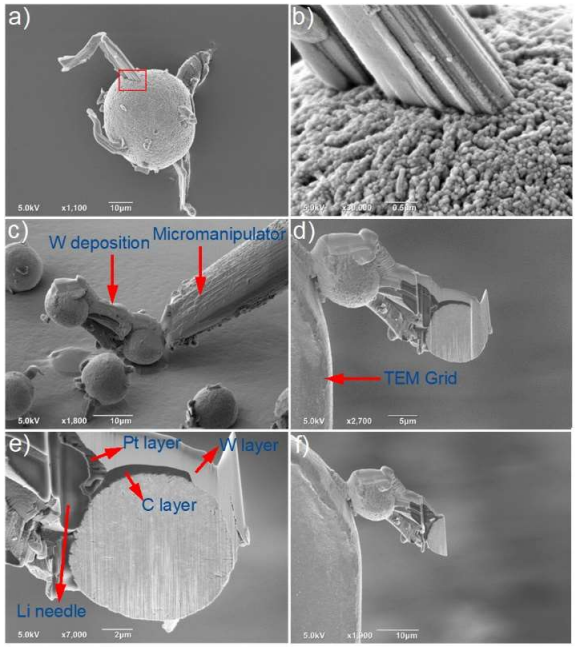

Figure S5: Overview of the TEM sample preparation using the FIB-SEM system. The measurement was done with the RK partially-lithiated sample using 100% of the Li amount required to obtain 1.01 Li equivalents per mol of Ni using 500 °C and a dwell time of one hour.

a) Top view image of one precursor secondary particle showing attached lithium-containing residual needles. **b)** High-magnification image of the area marked with a red rectangle in **a)**. **c)** The selected particles were coated with carbon and tungsten and then attached to a micromanipulator needle. **d)** The particles were attached to a TEM grid. The particle on the right was thinned down to an intermediate thickness of ~ 500 nm. **e)** After further thinning, the Pt, C, and W protective coatings and the interface between precursor secondary particle and the lithium-containing residual needle were still visible. **f)** TEM sample after the final thinning step.

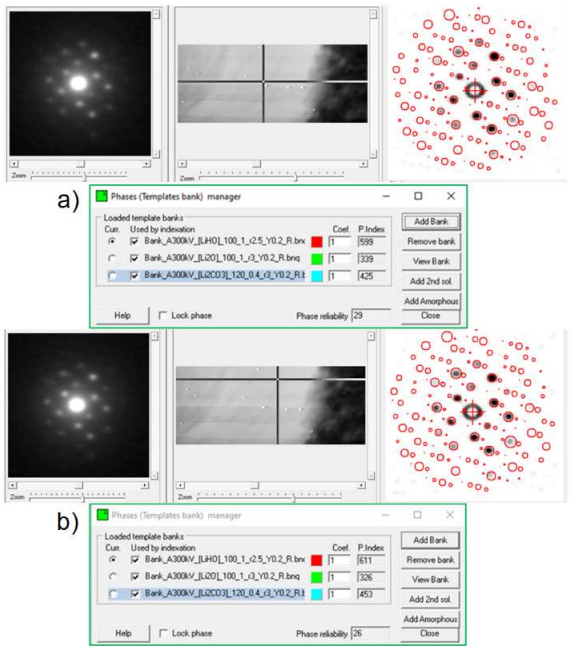

Figure S6: Matching procedure used to evaluate the TEM measurements. Screenshots from the ASTAR indexing software for matching PED patterns from two different exemplary positions **a)** and **b)**. The scanning-precession electron diffraction virtual bright-field (SPED-VBF) image is shown in the middle. The marker in the SPED-VBF image shows the position from which the PED diffraction pattern is displayed on the left. On the right, the best match from the library of simulated PED patterns from three different phases LiOH, Li_2O, and Li_2CO_3 is shown and overlaid on the actual PED pattern. The banks loaded from LiOH, Li_2O, and Li_2CO_3 phases are depicted as well. The Phase Index represents the quality of the match and is highest for the LiOH phase. The phase reliability factor is shown as well, confirming that the phase present here is LiOH (phase reliability factors of 15 or above denote that the solution is certain according to the ASTAR software's manual).

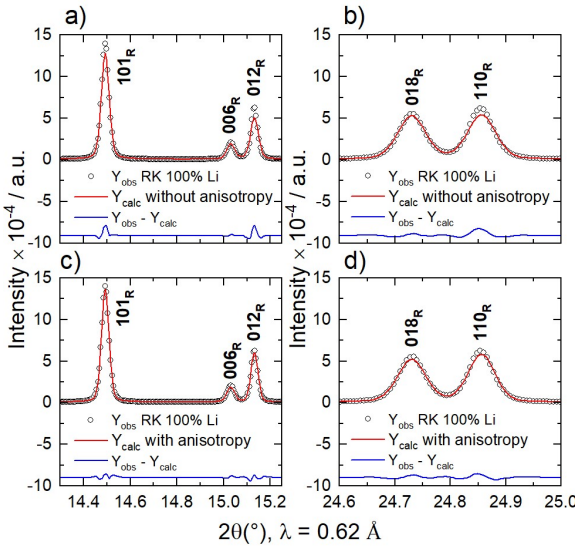

Figure S7: Rietveld refinement for the synchrotron powder X-ray diffraction (PXRD) pattern of one exemplary CAM from this study (sample partially-lithiated using the rotary kiln setup, 1.01 Li equivalents per mol of Ni and a dwell time of one hour, which was afterwards subjected to the main calcination. Two distinct angular regions are shown with characteristic Bragg peaks of the rhombohedral structure of $LiNiO_2$. The data are plotted as black circles, the pattern calculated from the applied refinement model as red lines and the difference between observed and calculated pattern as blue lines. **a)** and **b)** show the refinement without consideration of anisotropic size effects and **c)** and **d)** show the refinement including anisotropic size effects. The data were collected at the BL04-MSPD beamline of the ALBA synchrotron at a set wavelength of $\lambda = 0.62$ Å.

Table S1: Results of Rietveld refinement using the synchrotron PXRD patterns after the main calcination step for the samples partially-lithiated at 500 °C and a dwell time of one hour for the rotary kiln setup (RK) and box furnace (Box) and two different numbers of Li equivalents (0.8 and 1.01). The results for a material synthesized with a one-step calcination are shown as well. The table shows the refinement results for a structural model assuming spherical crystallites (1) and with consideration of anisotropic size effects (2): Ni occupancy on the Li site, average crystallite size (spherical particles), average apparent size using the anisotropy model (considering the deviating results for all possible crystallographic directions) and the reliability factors R_{Bragg}, R_{wp} and χ^2.

Sample	Ni occ. [%]	Size [nm]	Anisotropy [nm]	R_{Bragg}	R_{wp}	χ^2
RK 80% Li (1)	2.8(2)	205(9)	-	2.26	9.15	65.3
RK 80% Li (2)	3.0(2)	-	203(59)	1.89	7.57	50.0
RK 100% Li (1)	3.1(3)	198(3)	-	3.11	10.5	99.7
RK 100% Li (2)	3.4(2)	-	198(61)	2.64	8.65	75.4

Box 80% Li (1)	2.5(3)	253(11)	-	1.97	10.3	89.7
Box 80% Li (2)	2.8(2)	-	273(101)	1.69	8.68	71.4
Box 100% Li (1)	2.9(2)	229(12)	-	2.43	8.40	43.6
Box 100% Li (2)	3.2(2)	-	248(84)	1.99	6.65	30.7
One-step ref. (1)	3.2(3)	382(13)	-	2.91	10.3	84.0
One-step ref. (2)	3.6(2)	-	328(168)	2.71	8.38	55.1

Bibliography

[1] L.D. Dyer, B.S. Borie Jr, G.P. Smith, *Alkali metal-nickel oxides of the type* $MNiO_2$, Journal of the American Chemical Society **76**, 1499 (1954).

[2] M.G.S.R. Thomas, W.I.F. David, J.B. Goodenough, P. Groves, *Synthesis and structural characterization of the normal spinel* $LiNi_2O_4$, Materials Research Bulletin **20**, 1137 (1985).

[3] K.J.P.C. Mizushima, P.C. Jones, P.J. Wiseman, J.B. Goodenough, Li_xCoO_2 ($0 < x < -1$)*: A new cathode material for batteries of high energy density*, Materials Research Bulletin **15**, 783 (1980).

[4] C. Delmas, I. Saadoune, A. Rougier, *The cycling properties of the* $Li_xNi_{1-y}Co_yO_2$ *electrode*, Journal of Power Sources **44**, 595 (1993).

[5] M. Broussely, F. Perton, P. Biensan, J.M. Bodet, J. Labat, A. Lecerf, C. Delmas, A. Rougier, J.P. Peres, Li_xNiO_2*, a promising cathode for rechargeable lithium batteries*, Journal of Power Sources **54**, 109 (1995).

[6] Y. Nishi, H. Azuma, A. Omaru, *Non aqueous electrolyte cell*, U.S. Patent 4 959 281, 1990.

[7] T. Ohzuku, A. Ueda, *Solid-state redox reactions of* $LiCoO_2$ *(R3m) for 4 volt secondary lithium cells*, Journal of The Electrochemical Society **141**, 2972 (1994).

[8] A. Yano, M. Shikano, A. Ueda, H. Sakaebe, Z. Ogumi, $LiCoO_2$ *degradation behavior in the high-voltage phase transition region and improved reversibility with surface coating*, Journal of The Electrochemical Society **164**, A6116 (2016).

[9] M. Duffiet, M. Blangero, P.-E. Cabelguen, C. Delmas, D. Carlier, *Influence of the initial* Li/Co *ratio in* $LiCoO_2$ *on the high-voltage phase-transitions mechanisms*, The Journal of Physical Chemistry Letters **9**, 5334 (2018).

[10] H.-H. Ryu, K.-J. Park, C.S. Yoon, Y.-K. Sun, *Capacity fading of Ni-rich* $LiNi_xCo_yMn_{1-x-y}O_2$ ($0.6 \leq x \leq 0.95$) *cathodes for high-energy-density lithium-ion batteries: bulk or surface degradation?*, Chemistry of Materials **30**, 1155 (2018).

[11] H. Li, A. Liu, N. Zhang, Y. Wang, S. Yin, H. Wu, J.R. Dahn, *An unavoidable challenge for Ni-rich positive electrode materials for lithium-ion batteries*, Chemistry of Materials **31**, 7574 (2019).

[12] J.-H. Kim, H.-H. Ryu, S.J. Kim, C.S. Yoon, Y.-K. Sun, *Degradation Mechanism of Highly Ni-Rich* $LiNi_xCo_yMn_{1-x-y}O_2$ *Cathodes with* $x > 0.9$, ACS Applied Materials & Interfaces **11**, 30936 (2019).

[13] R. Adams, *Global cobalt production needs to be double in just 8 years. Where is it coming from?*, `https://stockhead.com.au/resources/global-cobalt-production-needs-to-double-in-just-8-years-where-is-it-coming-from/`, accessed: 2022-01-28.

[14] J. Chiat, *Nickel prices are at 11-year highs as EV demand heats up. Can we find enough of the battery metal to feed the beast?*, `https://stockhead.com.au/resources/nickel-prices-are-at-11-year-highs-as-ev-demand-heats-up-can-we-find-enough-of-the-battery-metal-to-feed-the-beast/`, accessed: 2022-01-28.

[15] S.W.D. Gourley, T. Or, Z. Chen, *Breaking free from cobalt reliance in lithium-ion batteries*, Iscience **23**, 101505 (2020).

[16] R.M. Salgado, F. Danzi, J.E. Oliveira, A. El-Azab, P.P. Camanho, M.H. Braga, *The latest trends in Electric Vehicles batteries*, Molecules **26**, 3188 (2021).

[17] N. Hume, H. Lockett, *Chinese metals tycoon faces steep losses on nickel price surge*, `https://www.ft.com/content/0269cdda-ef67-43c8-b820-a919c919b5fa/`, accessed: 2022-05-15.

[18] H.-K. Kim, J.M. Nam, *Tesla's shift to LFP cells to shake global battery industry*, `https://www.kedglobal.com/newsView/ked202110220007`, accessed: 2022-02-24.

[19] H. Li, M. Cormier, N. Zhang, J. Inglis, J. Li, J.R. Dahn, *Is cobalt needed in Ni-rich positive electrode materials for lithium ion batteries?*, Journal of The Electrochemical Society **166**, A429 (2019).

[20] W. Li, S. Lee, A. Manthiram, *High-Nickel NMA: A Cobalt-Free Alternative to NMC and NCA Cathodes for Lithium-Ion Batteries*, Advanced Materials **32**, 2002718 (2020).

[21] T. Liu, L. Yu, J. Liu, J. Lu, X. Bi, A. Dai, M. Li, M. Li, Z. Hu, L. Ma, D. Luo, J. Zheng, T. Wu, Y. Ren, J. Wen, F. Pan, K. Amine, *Understanding Co roles towards developing Co-free Ni-rich cathodes for rechargeable batteries*, Nature Energy **6**, 277 (2021).

[22] A. Aishova, G.-T. Park, C.S. Yoon, Y.-K. Sun, *Cobalt-Free High-Capacity Ni-Rich Layered* $LiNi_{0.9}Mn_{0.1}O_2$ *Cathode*, Advanced Energy Materials **10**, 1903179 (2020).

[23] J.B. Goodenough, D.G. Wickham, W.J. Croft, *Some magnetic and crystallographic properties of the system* $Li^{+}{}_{x}Ni^{++}{}_{1-2x}Ni^{+++}{}_{x}O$, Journal of Physics and Chemistry of Solids **5**, 107 (1958).

[24] H.C. Stober, *Analytical profiles of drug substances* (Elsevier Academic Press, Amsterdam, 1986), Vol. 15, 367–391.

[25] R.D. Shannon, *Revised effective ionic radii and systematic studies of interatomic distances in halides and chalcogenides*, Acta Crystallographica Section A: Crystal Physics, Diffraction, Theoretical and General Crystallography **32**, 751 (1976).

[26] T. Sata, *High-temperature vaporization of* Li_2O *component from solid solution* $Li_xNi_{1-x}O$ *in air*, Ceramics International **24**, 53 (1998).

[27] E. McCalla, G.H. Carey, J.R. Dahn, *Lithium loss mechanisms during synthesis of layered* $Li_xNi_{2-x}O_2$ *for lithium ion batteries*, Solid State Ionics **219**, 11 (2012).

[28] J.R. Dahn, U. von Sacken, C.A. Michal, *Structure and electrochemistry of* $Li_{1\pm y}NiO_2$ *and a new* Li_2NiO_2 *phase with the* $Ni(OH)_2$ *structure*, Solid State Ionics **44**, 87 (1990).

[29] W. Li, J.N. Reimers, J.R. Dahn, *In situ x-ray diffraction and electrochemical studies of* $Li_{1-x}NiO_2$, Solid State Ionics **67**, 123 (1993).

[30] H. Li, N. Zhang, J. Li, J.R. Dahn, *Updating the Structure and Electrochemistry of* Li_xNiO_2, Journal of The Electrochemical Society **165**, A2985 (2018).

[31] T. Ohzuku, A. Ueda, M. Nagayama, *Electrochemistry and structural chemistry of* $LiNiO_2$ *(R3m) for 4 volt secondary lithium cells*, Journal of the Electrochemical Society **140**, 1862 (1993).

[32] R. Kanno, H. Kubo, Y. Kawamoto, T. Kamiyama, F. Izumi, Y. Takeda, M. Takano, *Phase Relationship and Lithium Deintercalation in Lithium Nickel Oxides*, Journal of Solid State Chemistry **110**, 216 (1994).

[33] H. Arai, S. Okada, H. Ohtsuka, M. Ichimura, J. Yamaki, *Characterization and cathode performance of* $Li_{1-x}Ni_{1+x}O_2$ *prepared with the excess lithium method*, Solid State Ionics **80**, 261 (1995).

[34] H. Arai, S. Okada, Y. Sakurai, J. Yamaki, *Reversibility of* $LiNiO_2$ *cathode*, Solid State Ionics **95**, 275 (1997).

[35] A. Rougier, P. Gravereau, C. Delmas, *Optimization of the composition of the* $Li_{1-z}Ni_{1+z}O_2$ *electrode materials: structural, magnetic, and electrochemical studies*, Journal of The Electrochemical Society **143**, 1168 (1996).

[36] M. Bianchini, M. Roca-Ayats, P. Hartmann, T. Brezesinski, J. Janek, *There and back again—the journey of* $LiNiO_2$ *as a cathode active material*, Angewandte Chemie International Edition **58**, 10434 (2019).

[37] J.P. Peres, C. Delmas, A. Rougier, M. Broussely, F. Perton, P. Biensan, P. Willmann, *The relationship between the composition of lithium nickel oxide and the loss of reversibility during the first cycle*, Journal of Physics and Chemistry of Solids **57**, 1057 (1996).

[38] C. Pouillerie, E. Suard, C. Delmas, *Structural Characterization of* $Li_{1-z-x}Ni_{1+z}O_2$ *by Neutron Diffraction*, Journal of Solid State Chemistry **158**, 187 (2001).

[39] V. Bianchi, D. Caurant, N. Baffier, C. Belhomme, E. Chappel, G. Chouteau, S. Bach, J.P. Pereira-Ramos, A. Sulpice, P. Wilmann, *Synthesis, structural characterization and magnetic properties of quasistoichiometric* $LiNiO_2$, Solid State Ionics **140**, 1 (2001).

[40] V. Bianchi, S. Bach, C. Belhomme, J. Farcy, J.P. Pereira-Ramos, D. Caurant, N. Baffier, P. Willmann, *Electrochemical investigation of the Li insertion–extraction reaction as a function of lithium deficiency in* $Li_{1-x}Ni_{1+x}O_2$, Electrochimica Acta **46**, 999 (2001).

[41] W. Li, J.C. Currie, J. Wolstenholme, *Influence of morphology on the stability of* $LiNiO_2$, Journal of Power Sources **68**, 565 (1997).

[42] S.P. Sheu, I.C. Shih, C.Y. Yao, J.M. Chen, W.M. Hurng, *Studies of* $LiNiO_2$ *in lithium-ion batteries*, Journal of Power Sources **68**, 558 (1997).

[43] K. Dokko, M. Nishizawa, S. Horikoshi, T. Itoh, M. Mohamedi, I. Uchida, *In Situ Observation of* $LiNiO_2$ *Single-Particle Fracture during Li-Ion Extraction and Insertion*, Electrochemical and Solid State Letters **3**, 125 (2000).

[44] H.-H. Sun, A. Manthiram, *Impact of microcrack generation and surface degradation on a nickel-rich layered* $LiNi_{0.9}Co_{0.05}Mn_{0.05}O_2$ *cathode for lithium-ion batteries*, Chemistry of Materials **29**, 8486 (2017).

[45] C.S. Yoon, D.-W. Jun, S.-T. Myung, Y.-K. Sun, *Structural stability of* $LiNiO_2$ *cycled above* 4.2 V, ACS Energy Letters **2**, 1150 (2017).

[46] G. W. Nam, N.-Y. Park, K.-J. Park, J. Yang, J. Liu, C.S. Yoon, Y.-K. Sun, *Capacity fading of Ni-rich NCA cathodes: effect of microcracking extent*, ACS Energy Letters **4**, 2995 (2019).

[47] S. Schweidler, L. de Biasi, G. Garcia, A. Mazilkin, P. Hartmann, T. Brezesinski, J. Janek, *Investigation into mechanical degradation and fatigue of high-Ni NCM cathode material: A long-term cycling study of full cells*, ACS Applied Energy Materials **2**, 7375 (2019).

[48] C.-C. Chang, J.Y. Kim, P.N. Kumta, *Influence of crystallite size on the electrochemical properties of chemically synthesized stoichiometric* $LiNiO_2$, Journal of the Electrochemical Society **149**, A1114 (2002).

[49] J. Välikangas, P. Laine, M. Hietaniemi, T. Hu, P. Tynjälä, U. Lassi, *Precipitation and Calcination of High-Capacity* $LiNiO_2$ *Cathode Material for Lithium-Ion Batteries*, Applied Sciences **10**, 8988 (2020).

[50] A. Iqbal, D. Li, *Systematic study of the effect of calcination temperature and Li/M molar ratio on high performance Ni-rich layered* $LiNi_{0.9}Co_{0.1}O_2$ *cathode materials*, Chemical Physics Letters **720**, 97 (2019).

[51] T.-J. Park, J.-B. Lim, J.-T. Son, *Effect of calcination temperature of size controlled microstructure of* $LiNi_{0.8}Co_{0.15}Al_{0.05}O_2$ *cathode for rechargeable lithium battery*, Bulletin of the Korean Chemical Society **35**, 357 (2014).

[52] K. Wu, F. Wang, L. Gao, M.-R. Li, L. Xiao, L. Zhao, S. Hu, X. Wang, Z. Xu, Q. Wu, *Effect of precursor and synthesis temperature on the structural and electrochemical properties of* $Li(Ni_{0.5}Co_{0.2}Mn_{0.3})O_2$, Electrochimica Acta **75**, 393 (2012).

[53] J. Zheng, P. Yan, L. Estevez, C. Wang, J.-G. Zhang, *Effect of calcination temperature on the electrochemical properties of nickel-rich* $LiNi_{0.76}Mn_{0.14}Co_{0.10}O_2$ *cathodes for lithium-ion batteries*, Nano Energy **49**, 538 (2018).

[54] H. Ronduda, M. Zybert, A. Szczęsna-Chrzan, T. Trzeciak, A. Ostrowski, D. Szymański, W. Wieczorek, W. Raróg-Pilecka, M. Marcinek, *On the Sensitivity of the Ni-rich Layered Cathode Materials for Li-ion Batteries to the Different Calcination Conditions*, Nanomaterials **10**, 2018 (2020).

[55] G.V. Zhuang, G. Chen, J. Shim, X. Song, P.N. Ross, T.J. Richardson, Li_2CO_3 *in* $LiNi_{0.8}Co_{0.15}Al_{0.05}O_2$ *cathodes and its effects on capacity and power*, Journal of Power Sources **134**, 293 (2004).

[56] S.S. Zhang, *Insight into the gassing problem of Li-ion battery*, Frontiers in Energy Research **2**, 59 (2014).

[57] R. Jung, R. Morasch, P. Karayaylali, K. Phillips, F. Maglia, C. Stinner, Y. Shao-Horn, H.A. Gasteiger, *Effect of ambient storage on the degradation of Ni-rich positive electrode materials (NMC811) for Li-ion batteries*, Journal of The Electrochemical Society **165**, A132 (2018).

[58] A.T.S. Freiberg, J. Sicklinger, S. Solchenbach, H.A. Gasteiger, Li_2CO_3 *decomposition in Li-ion batteries induced by the electrochemical oxidation of the electrolyte and of electrolyte impurities*, Electrochimica Acta **346**, 136271 (2020).

[59] S. Oswald, D. Pritzl, M. Wetjen, H.A. Gasteiger, *Novel Method for Monitoring the Electrochemical Capacitance by In Situ Impedance Spectroscopy as Indicator for Particle Cracking of Nickel-Rich NCMs: Part I. Theory and Validation*, Journal of The Electrochemical Society **167**, 100511 (2020).

[60] S. Oswald, D. Pritzl, M. Wetjen, H.A. Gasteiger, *Novel Method for Monitoring the Electrochemical Capacitance by In Situ Impedance Spectroscopy as Indicator for Particle Cracking of Nickel-Rich NCMs: Part II. Effect of Oxygen Release Dependent on Particle Morphology*, Journal of The Electrochemical Society **168**, 120501 (2021).

[61] A. Liu, N. Phattharasupakun, M.M.E. Cormier, E. Zsoldos, N. Zhang, E. Lyle, P. Arab, M. Sawangphruk, J.R. Dahn, *Factors that affect capacity in the low voltage kinetic hindrance region of Ni-Rich positive electrode materials and diffusion measurements from a reinvented approach*, Journal of The Electrochemical Society **168**, 070503 (2021).

[62] S. Moores, *Benchmark Analysis: Lithium ion battery cell prices close in on* \$100/kWh *& come of EV age, but is this the end for double digit declines?*, `https://www.benchmarkminerals.com/membership/benchmark-analysis-lithium-ion-battery-cell-prices-close-in-on-100-kwh-come-of-ev-age-but-is-this-the-end-for-double-digit-declines-2/`, accessed: 2022-02-08.

[63] P. Desai, M. Nguyen, *Shortages flagged for EV materials lithium and cobalt*, `https://www.reuters.com/business/energy/shortages-flagged-ev-materials-lithium-cobalt-2021-07-01/`, accessed: 2022-02-08.

[64] G. Silberg, E. Shapiro, 22nd *Annual Global Automotive Executive Survey 2021*, `https://assets.kpmg/content/dam/kpmg/xx/pdf/2021/11/global-automotive-executive-summary-2021.pdf`, accessed: 2022-02-09.

[65] S. Moores, *Global battery arms race: 200 Gigafactories, China leads*, `https://www.benchmarkminerals.com/membership/global-battery-arms-race-200-gigafactories-china-leads-2/`, accessed: 2022-02-08.

[66] M. Kamieth, *BASF Battery Materials investor update September 27, 2021*, https://www.basf.com/global/documents/en/investor-relations/calendar-and-publications/presentations/2021/BASF_Investor-Update_Presentation_Battery-Materials.pdf, accessed: 2022-02-08.

[67] F. Zou, Y. Liu, *Method to produce cathode materials for Li-ion batteries*, U.S. Patent 2021/0013507 A1, 2021.

[68] M.N. Obrovac, L. Zheng, M.D.L. Garayt, *Engineered particle synthesis by dry particle microgranulation*, Cell Reports Physical Science **1**, 100063 (2020).

[69] L. Zheng, J.C. Bennett, M.N. Obrovac, *All-Dry Synthesis of Single Crystal NMC Cathode Materials for Li-Ion Batteries*, Journal of The Electrochemical Society **167**, 130536 (2020).

[70] Noritake Co. Ltd., *World's first hydrogen combustion-type continuous combustion furnace for making Li-ion battery electrode materials goes on sale by Noritake, Tokyo Gas and TGES*, https://www.prnewswire.com/news-releases/worlds-first-hydrogen-combustion-type-continuous-combustion-furnace-for-making-lithium-ion-battery-electrode-materials-goes-on-sale-by-noritake-tokyo-gas-and-tges-301416032.html, accessed: 2022-02-11.

[71] M. Lehmann, *Production of cathode active material in Europe*, https://www.onejoon.de/site/assets/files/34611/onejoon_e-mobility_technology_international_09_2021.pdf, accessed: 2022-02-10.

[72] M. Yamamoto, O. Sasaki, N. Kimura, K. Nishimura, W. Koyonagi, T. Kuwahara, *Method for producing lithium hydroxide anhydride and rotary kiln to be used therefor*, WO 2018084134, 2018.

[73] I. Petrovic, A. Thurston, S. Sheargold, *Process for synthesis of a layered oxide cathode composition*, WO 2012/177833, 2012.

[74] A. Park, J. Kim, S.-Y. Han, J. Paulsen, K.-T. Lee, R. De Palma, *Precursor and method for preparing Ni based cathode material for rechargeable lithium ion batteries*, WO 2018/158078 A1, 2018.

[75] M. Bianchini, F. Fauth, P. Hartmann, T. Brezesinski, J. Janek, *An in situ structural study on the synthesis and decomposition of* $LiNiO_2$, Journal of Materials Chemistry A **8**, 1808 (2020).

[76] J.E. Harlow, X. Ma, J. Li, E. Logan, Y. Liu, N. Zhang, L. Ma, S.L. Glazier, M.M.E. Cormier, M. Genovese, S. Buteau, A. Cameron, J.E. Stark, J.R. Dahn, *A wide range of testing results on an excellent lithium-ion cell chemistry to be*

used as benchmarks for new battery technologies, Journal of The Electrochemical Society **166**, A3031 (2019).

[77] F. Zhang, S. Lou, S. Li, Z. Yu, Q. Liu, A. Dai, C. Cao, M.F. Toney, M. Ge, X. Xiao, W.-K. Lee, Y. Yao, J. Deng, T. Liu, Y. Tang, G. Yin, J. Lu, D. Su, J. Wang, *Surface regulation enables high stability of single-crystal lithium-ion cathodes at high voltage*, Nature Communications **11**, 1 (2020).

[78] H.-H. Ryu, B. Namkoong, J.-H. Kim, I. Belharouak, C.S. Yoon, Y.-K. Sun, *Capacity fading mechanisms in Ni-rich single-crystal NCM cathodes*, ACS Energy Letters **6**, 2726 (2021).

[79] Y. Bi, J. Tao, Y. Wu, L. Li, Y. Xu, E. Hu, B. Wu, J. Hu, C. Wang, J.-G. Zhang, Y. Qi, J. Xiao, *Reversible planar gliding and microcracking in a single-crystalline Ni-rich cathode*, Science **370**, 1313 (2020).

[80] J. Langdon, A. Manthiram, *A perspective on single-crystal layered oxide cathodes for lithium-ion batteries*, Energy Storage Materials **37**, 143 (2021).

[81] J. Li, H. Li, W. Stone, R. Weber, S. Hy, J.R. Dahn, *Synthesis of single crystal* $LiNi_{0.5}Mn_{0.3}Co_{0.2}O_2$ *for lithium ion batteries*, Journal of The Electrochemical Society **164**, A3529 (2017).

[82] H. Li, J. Li, X. Ma, J.R. Dahn, *Synthesis of single crystal* $LiNi_{0.6}Mn_{0.2}Co_{0.2}O_2$ *with enhanced electrochemical performance for lithium ion batteries*, Journal of The Electrochemical Society **165**, A1038 (2018).

[83] Y. Kim, *Lithium nickel cobalt manganese oxide synthesized using alkali chloride flux: morphology and performance as a cathode material for lithium ion batteries*, ACS Applied Materials & Interfaces **4**, 2329 (2012).

[84] G. Qian, Y. Zhang, L. Li, R. Zhang, J. Xu, Z. Cheng, S. Xie, H. Wang, Q. Rao, Y. He, Y. Shen, L. Chen, M. Tang, Z.-F. Ma, *Single-crystal nickel-rich layered-oxide battery cathode materials: synthesis, electrochemistry, and intra-granular fracture*, Energy Storage Materials **27**, 140 (2020).

[85] S.-H. Lee, S.-J. Sim, B.-S. Jin, H.-S. Kim, *High performance well-developed single crystal* $LiNi_{0.91}Co_{0.06}Mn_{0.03}O_2$ *cathode via* $LiCl - NaCl$ *flux method*, Materials Letters **270**, 127615 (2020).

[86] L. Li, G. Hu, Y. Cao, Z. Peng, J. Zeng, S. Zhang, K. Du, *Synthesis of micron-sized single-crystalline* $LiNi_{0.65}Co_{0.07}Mn_{0.28}O_2$ *cathode material for Li-ion batteries via various calcination additives with large ion radius*, Ionics 1 (2022).

[87] G. Qian, Z. Li, D. Meng, J.-B. Liu, Y.-S. He, Q. Rao, Y. Liu, Z.-F. Ma, L. Li, *Temperature-swing synthesis of large-size single-crystal* $LiNi_{0.6}Mn_{0.2}Co_{0.2}O_2$ *cathode materials*, Journal of the Electrochemical Society **168**, 010534 (2021).

[88] Y. Ma, J.H. Teo, D. Kitsche, T. Diemant, F. Strauss, Y. Ma, D. Goonetilleke, J. Janek, M. Bianchini, T. Brezesinski, *Cycling Performance and Limitations of* $LiNiO_2$ *in Solid-State Batteries*, ACS Energy Letters **6**, 3020 (2021).

[89] R. Koerver, I. Ayguün, T. Leichtweiß, C. Dietrich, W. Zhang, J.O. Binder, P. Hartmann, W.G. Zeier, J. Janek, *Capacity fade in solid-state batteries: interphase formation and chemomechanical processes in nickel-rich layered oxide cathodes and lithium thiophosphate solid electrolytes*, Chemistry of Materials **29**, 5574 (2017).

[90] T. Shi, Y.-Q. Zhang, Q. Tu, Y. Wang, M.C. Scott, G. Ceder, *Characterization of mechanical degradation in an all-solid-state battery cathode*, Journal of Materials Chemistry A **8**, 17399 (2020).

[91] G. Conforto, R. Ruess, D. Schröder, E. Trevisanello, R. Fantin, F.H. Richter, J. Janek, *Editors' Choice—Quantification of the Impact of Chemo-Mechanical Degradation on the Performance and Cycling Stability of NCM-Based Cathodes in Solid-State Li-Ion Batteries*, Journal of The Electrochemical Society **168**, 070546 (2021).

[92] X. Liu, B. Zheng, J. Zhao, W. Zhao, Z. Liang, Y. Su, C. Xie, K. Zhou, Y. Xiang, J. Zhu, H. Wang, G. Zhong, Z. Gong, J. Huang, Y. Yang, *Electrochemo-Mechanical Effects on Structural Integrity of Ni-Rich Cathodes with Different Microstructures in All Solid-State Batteries*, Advanced Energy Materials **11**, 2003583 (2021).

[93] Y. Han, S.H. Jung, H. Kwak, S. Jun, H.H. Kwak, J.H. Lee, S.-T. Hong, Y.S. Jung, *Single-or Poly-Crystalline Ni-Rich Layered Cathode, Sulfide or Halide Solid Electrolyte: Which Will be the Winners for All-Solid-State Batteries?*, Advanced Energy Materials **11**, 2100126 (2021).

[94] C. Wang, R. Yu, S. Hwang, J. Liang, X. Li, C. Zhao, Y. Sun, J. Wang, N. Holmes, R. Li, H. Huang, S. Zhao, L. Zhang, S. Lu, D. Su, X. Sun, *Single crystal cathodes enabling high-performance all-solid-state lithium-ion batteries*, Energy Storage Materials **30**, 98 (2020).